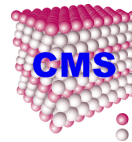
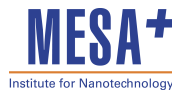


**TOWARDS PERFECT SPIN-FILTERING:  
A FIRST-PRINCIPLES STUDY**

**Volodymyr Mykolajovych Karpan**

Samenstelling promotiecommissie:

Prof. dr. M. J. Peters	Universiteit Twente, voorzitter
Prof. dr. P. J. Kelly	Universiteit Twente, promotor
Prof. dr. P. H. Dederichs	Institut für Festkörperforschung, Jülich
Prof. dr. C. Filippi	Universiteit Twente, Universiteit Leiden
Prof. dr. J. L. Herek	Universiteit Twente
Prof. dr. B. Koopmans	Technische Universiteit Eindhoven
Prof. dr. W. L. Vos	Universiteit Twente, AMOLF
Dr. M. Zwierzycki	Instytut Fizyki Molekularnej, Poznań



The work presented in this thesis was financially supported by “NanoNed”, a nanotechnology programme of the Dutch Ministry of Economic Affairs, and was carried out in the “Computational Materials Science” (CMS) group which belongs to the University of Twente’s Faculty of Science and Technology (TNW) and MESA<sup>+</sup> Institute for Nanotechnology. Part of the calculations were performed with a grant of computer time from the “Stichting Nationale Computerfaciliteiten (NCF)” which is financially supported by the “Nederlandse Organisatie voor Wetenschappelijk Onderzoek” (NWO).

Towards perfect spin-filtering: a first-principles study.

V.M. Karpan,

ISBN: 978-90-365-2687-6

Thesis Universiteit Twente, Enschede.

Copyright © V.M. Karpan, 2008

Printed by Gildeprint Drukkerijen BV, Enschede, the Netherlands

---

**TOWARDS PERFECT SPIN-FILTERING:  
A FIRST-PRINCIPLES STUDY**

**PROEFSCHRIFT**

ter verkrijging van  
de graad van doctor aan de Universiteit Twente,  
op gezag van de rector magnificus,  
prof. dr. W. H. M. Zijm,  
volgens besluit van het College voor promoties  
in het openbaar te verdedigen  
op vrijdag 20 juni 2008 om 13.15 uur

door

**Volodymyr Mykolajovych Karpan**

geboren op 16 September 1977  
te Gorodenka, Oekraïne

Dit proefschrift is goedgekeurd door:

Prof.dr. P. J. Kelly

promotor

to Yulya, my parents  
and teachers



# Contents

<b>1</b>	<b>Introduction</b>	<b>1</b>
1.1	Spintronics . . . . .	1
1.1.1	Magnetoresistance . . . . .	3
1.1.2	Spin injection into semiconductors . . . . .	7
1.2	Computational scheme . . . . .	8
1.2.1	Landauer-Büttiker formalism . . . . .	8
1.2.2	Density Functional Theory . . . . .	10
1.2.3	Tight-Binding Muffin-Tin Orbitals . . . . .	11
1.2.4	Wave function matching . . . . .	15
1.3	Thesis outline . . . . .	18
	Bibliography . . . . .	19
<b>2</b>	<b>Spin injection from Fe into InAs</b>	<b>23</b>
2.1	Introduction . . . . .	23
2.2	Method . . . . .	24
2.3	FeInAs revisited . . . . .	26
2.4	Fe BL InAs system . . . . .	30
2.4.1	Ideal Fe Au InAs junction . . . . .	31
2.4.2	Disordered Fe Au InAs junction . . . . .	34
2.5	Conclusions . . . . .	36
	Bibliography . . . . .	38
<b>3</b>	<b>Influence of Roughness and Disorder on Tunneling Magnetoresistance</b>	<b>41</b>
3.1	Introduction . . . . .	41
3.2	Methods, Models and Technical Details . . . . .	42
3.3	Barrier profile . . . . .	45
3.4	Ideal Fe vacuum Fe MTJ. Transport calculations . . . . .	46
3.4.1	Parallel configuration: Majority channel . . . . .	47
3.4.2	Parallel configuration: Minority channel . . . . .	48

3.5	Effect of interfacial roughness on the TMR . . . . .	53
3.5.1	Majority transmission . . . . .	55
3.5.2	Minority transmission . . . . .	57
3.5.3	Antiparallel spin alignment . . . . .	59
3.6	Substitutional disorder: $Fe_xCo_{1-x}$ electrodes . . . . .	59
3.7	Discussion and Conclusions . . . . .	61
3.8	Appendix 1: The k-point sampling . . . . .	63
3.9	Appendix 2: Configurational averaging and the size of the scattering region . . . . .	64
	Bibliography . . . . .	67
<b>4</b>	<b>Recovering the Jullière model by including interface disorder</b>	<b>71</b>
4.1	Introduction . . . . .	71
4.2	Early models . . . . .	73
4.3	<i>Ab-initio</i> results . . . . .	76
4.3.1	Factorizing the conductance . . . . .	78
4.3.2	Factorization of conductance for finite bias . . . . .	81
4.4	Summary and Conclusions . . . . .	84
	Bibliography . . . . .	84
<b>5</b>	<b>Graphene and Graphite as Perfect Spin Filters</b>	<b>87</b>
5.1	Introduction . . . . .	87
5.2	Computational Method . . . . .	90
5.3	Geometry and electronic structure of TM Gr <sub>n</sub>  TM . . . . .	92
5.3.1	Graphite and graphene . . . . .	92
5.3.2	Graphene on Ni(111) substrate . . . . .	94
5.3.3	Ni Gr <sub>n</sub>  Ni(111) junction . . . . .	95
5.4	Electron transport through a FM Gr <sub>n</sub>  FM junction . . . . .	98
5.4.1	Specular interface . . . . .	98
5.4.2	Ni Cu <sub>m</sub>  Gr <sub>n</sub>  Cu <sub>m</sub>  Ni (111) . . . . .	101
5.4.3	Effect of disorder . . . . .	102
5.5	Discussion and Conclusions . . . . .	104
	Bibliography . . . . .	106
<b>6</b>	<b>A new material system for highly planar electronics</b>	<b>109</b>
	Bibliography . . . . .	114
	<b>Summary</b>	<b>117</b>
	<b>Samenvatting</b>	<b>119</b>
	<b>Acknowledgments</b>	<b>123</b>



**Curriculum vitae**

**125**



# Chapter 1

## Introduction

*In this thesis, the spin-dependent transport of electrons in multilayered structures is studied. In the first part of this chapter a general introduction to the field of spintronics is presented. Problems and progress in the main research areas of spintronics: magnetoresistance and spin injection into nonmagnetic materials are discussed. In the second part of this chapter we introduce the theoretical basis of our numerical scheme, namely density functional theory, the linearized-muffin tin orbitals method, the wave function matching method and finally the Landauer–Büttiker transport formalism. At the end we give a brief outline of the remainder of the thesis.*

### 1.1 Spintronics

The central object of study in this thesis is the spin degree of freedom of an electron in electronic transport. Just as a planet orbiting the sun and spinning about its own axis possesses both orbital and spin angular momenta, so does an electron orbiting a nucleus. Since the electron has no radial extent and cannot be “turning” about its axis, this is purely an analogy. The spin is an intrinsic property of the electron and has a constant value. However, just as the planets can rotate clockwise or anticlockwise, the electron spin can also be considered to be clockwise or anticlockwise: there are two different kinds of spin according to whether the projection of the spin onto a given quantization axis is  $+\frac{\hbar}{2}$  or  $-\frac{\hbar}{2}$ , which we term spin “up” and spin “down”, respectively. The relative number of electrons with spin up and spin down is very important for the magnetic properties of a chosen material. Nonmagnetic materials are characterized by the same number of electrons with the same properties in both spin channels<sup>1</sup>. As for magnetic materials, there is an imbalance in the density of states for spin up and spin down electrons as illustrated in Fig. 1.1. In the following the channel with more (fewer) states below the Fermi level is termed the majority (minority) spin channel. The spin of an electron is an intrinsic angular momentum  $\mathbf{s}$  which is directly coupled to its magnetic moment  $\mathbf{m}$  by the relation  $\mathbf{m} = -g_s\mu_B(\mathbf{s}/\hbar)$

---

<sup>1</sup>the term “channel” is used to emphasize our interest in studying electronic transport

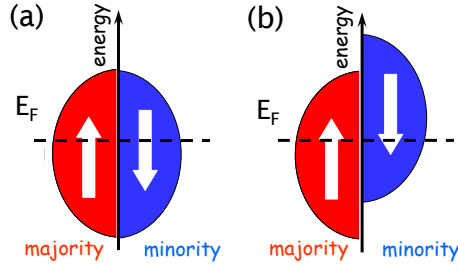


**Figure 1.1:** Spin-dependent densities of states in case of a nonmagnetic metal (a) and of a ferromagnetic metal (b).  $E_F$  is the Fermi energy. Majority (minority) describes the spin-channel with more (fewer) states below the Fermi energy.

where  $\mu_B = e\hbar/(2m_e)$  is the Bohr magneton and  $g_s$  the Landé factor which is roughly equal to two.

The spin of an electron was first measured in 1922 by Stern and Gerlach [1], in an experiment that was proposed by Stern in 1921 [2]. A theoretical explanation was developed by Kronig who, however, decided not to publish his results because the linear speed required on the electron surface was larger than the speed of light. Later, in 1925 a theoretical study of intrinsic electron spin by Uhlenbeck and Goudsmit [3] appeared. In 1927 Pauli introduced spin into quantum mechanics [4]. A breakthrough in the understanding of spin was made by Dirac who, by combining quantum mechanics and special relativity, developed a theoretical framework from which the magnetic moment and “spin” of electrons followed automatically.

Despite the central role played by electron spin in many areas of condensed matter physics, it barely figured in the mainstream of charge-based electronics. The situation changed with the discovery of oscillatory interlayer exchange coupling in Fe|Cr and Co|Cu multilayers by Grünberg *et al.* [5] and later by Parkin *et al.* [6–8]. This led to the near simultaneous discovery of the giant magnetoresistance effect (GMR) by two experimental research groups led by A. Fert [9] in Paris and P. Grünberg [10] in Jülich. The GMR effect is a milestone in condensed matter physics for which both Fert and Grünberg were awarded the Nobel Prize in Physics in 2007. From the study and application of this effect a new branch of solid state physics has emerged, which is called spintronics or spin electronics<sup>2</sup>. This field refers to the study of the role played by electron spin in transport, and to possible devices that specifically exploit spin properties instead of or in addition to charge degrees of freedom. Though, current efforts in this field involve several major directions, we will restrict ourselves to a discussion of spin transport phenomena in metal and semiconductor-based devices. The focus of the former is on perfecting the existing magnetoresistance - based technology by either developing new materials or making improvements or variations in the ex-

<sup>2</sup>I use spintronics to include magnetoelectronics which sometimes used just to describe spin transport in metals

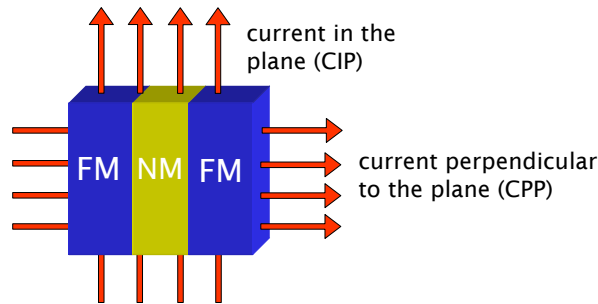


**Figure 1.2:** Example of a magnetic layered junction that consists of two ferromagnetic metallic electrodes and a nonmagnetic metallic spacer layer between them (FM|NM|FM junction). If the current flows perpendicular to the planes of a junction (perpendicular to the growth direction) we speak of a current-perpendicular-to-the-plane (CPP) geometry. If the injected current flows parallel to the planes we speak of a current-in-plane (CIP) geometry.

isting devices that allow for better spin filtering. The second field focuses on finding novel ways of generating and utilizing spin-polarized currents in semiconductor-based systems. Range of interests includes investigation of spin transport in semiconductors (SC) and looking for ways in which semiconductors can function as spin polarizers and spin valves. In the following subsections we discuss in more detail some major issues in these two fields.

### 1.1.1 Magnetoresistance

We consider here metal-based spintronic devices that consist of the leads made of a ferromagnetic metal (FM) with a nonmagnetic spacer layer between them. To be more specific we focus on the electrical resistance of such devices. The electrical resistance of a ferromagnetic metal (FM) can be changed in different ways. One of the simplest ways is to influence the electrical resistance by changing the temperature. Resistance grows as a function of temperature due to the increase of electron scattering by thermally activated ions. A more complicated way of changing the electrical resistance of a FM is associated with the change of a FM magnetization direction relative to the current direction. Since this effect depends on the angle between the current direction and the orientation of the magnetization it is called the anisotropic magnetoresistance (AMR) effect. It was discovered by Thompson<sup>3</sup> in 1857 [11]. This magnetoresistance (MR) effect is small, typically  $\sim 1\%$ .

With the progress of fabrication techniques it became possible to produce thin layered structures that exhibited MRs much larger than the AMR effect. In the

<sup>3</sup>also known as Lord Kelvin

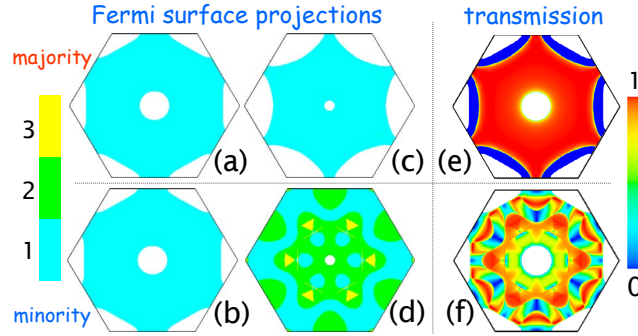


**Figure 1.3:** Fermi surface projection of Cu (a) and (b) and of Co for majority (c) and minority (d) spin channels. The number of propagating states is colour-coded following the colour bar on the left. Spin polarization of current in Cu|Co junction is made clear with majority (e) and minority (f) transmissions.

following we discuss the successors of the AMR effect - giant and tunneling magnetoresistance effects.

The GMR effect is a quantum mechanical effect which is observed in a junction consisting of two ferromagnetic (FM) leads separated by a nonmagnetic metal (NM) spacer layer. In such a FM|NM|FM junction the relative orientation of magnetization directions in the magnetic layers can be changed by applying an external magnetic field. Changing the relative orientation of these magnetizations from parallel to antiparallel gives rise to a change of the electrical resistance of the device. The GMR effect is observed with various combinations of materials. To explain it, we consider a Co|Cu|Co(111) junction in the so-called current-perpendicular-to-the-plane (CPP) geometry shown schematically in Fig. 1.2. From this figure a difference between the CPP and current-in-the-plane (CIP) geometries is obvious: an electron contributing to electrical transport must pass through every plane in the CPP geometry. We also assume perfect periodicity in the planes parallel to the Co|Cu interface. A Co|Cu|Co junction consists of two identical Co|Cu interfaces. Let us first study spin-dependent transport through a single interface. We assume that the electric current through such an interface consists of independent majority and minority spin components. This approximation is called Mott’s “two current model” and it works well at low temperatures where the spin relaxation length,  $\lambda_{sf}$  (how far an electron can travel before it loses its spin information), is much larger than the elastic mean free path,  $\ell_e$  (the average distance an electron travels before it is elastically scattered at a defect) [12–14]. The resistance of a Co|Cu interface is represented within the two-current resistor model as two resistors in parallel, one for each spin channel. Most important is that these resistances are different so the current injected from Co into Cu will be spin-polarized. We can understand this by considering how electrons on the Fermi surface are transmitted (or reflected) at a Co|Cu(111) interface. Because

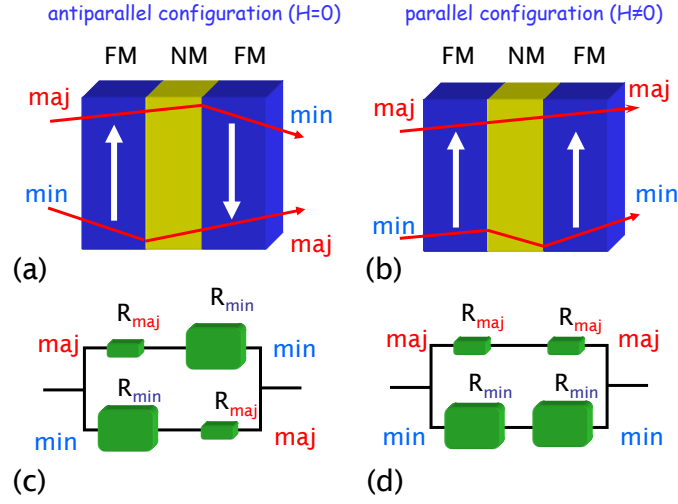


**Figure 1.4:** Schematic layout of two states of a spin-valve structure. In the antiparallel configuration (a) both type of electrons are subject to strong interface reflection while in the parallel configuration (b) only minority spin electrons encounter a highly reflective interface. The two current model shows that the parallel configuration (d) results in a lower resistance than the antiparallel configuration (c).

the momentum parallel to the interface is conserved, the transmission  $T$  depends on the two-dimensional Bloch wavevector  $\mathbf{k}_{\parallel}$  which we can use to label the electron states as well as the spin  $\sigma$ ,  $T = T_{\sigma}(\mathbf{k}_{\parallel})$ . Results of calculations of  $T_{\sigma}(\mathbf{k}_{\parallel})$  from Ref. [15] are shown in Fig. 1.3. In Fig. 1.3(a-d) we show projections of the Fermi surfaces for Co and Cu majority and minority spin electrons on a plane perpendicular to the [111] direction. As can be seen, the Fermi surface projection (FSP) for Cu (Fig. 1.3a) and Co majority spin (Fig. 1.3c) are very similar, as are the electron velocities and their wave function characters. The transmission from Co to Cu is almost perfect (unity) (Fig. 1.3e) and the resistance is small. In this figure the transmission  $T_{\sigma}(\mathbf{k}_{\parallel})$  is maximum in most of the points where the Cu and Co majority FSPs overlap. The FSPs of Cu and Co minority spin electrons as well as their velocities and wave function characters are quite different, therefore, strong scattering takes place (Fig. 1.3f). Thus, due to spin-dependent mismatch between the electronic properties of these two materials, spin filtering of a current injected from Co into Cu occurs at the interface.

Experimental measurements of the spin polarization of a current injected into a nonmagnetic material are complicated. This problem can be circumvented by adding another FM layer as shown in Fig. 1.4. We assume that the thickness of the NM layer is such that in the absence of an external magnetic field the magnetizations of the FM

layers are oriented antiparallel. As already mentioned the relative orientation can be switched to parallel if an external magnetic field of sufficient strength is applied. The electrical resistance of a magnetic junction in the parallel ( $P$ ) and antiparallel ( $AP$ ) configurations can be calculated using the two-current resistor model as illustrated in Fig. 1.4. According to this model, the  $AP$  conductance  $G_{AP} = 2/(R_{maj} + R_{min})$  while the  $P$  conductance  $G_P = (R_{maj} + R_{min})/(2R_{maj}R_{min})$ . For different  $R_{maj}$  and  $R_{min}$  the nonzero magnetoresistance is  $MR = (G_P - G_{AP})/G_{AP}$ .

Tunneling magnetoresistance (TMR) is observed in a magnetic tunnel junction (MTJ) in which the NM spacer layer is replaced with a nonmagnetic insulator (I). In a MTJ the conductance depends on the relative orientation of the FM magnetizations. However, in a FM|I|FM junction the electron transmission is characterized by quantum mechanical tunneling which is spin-dependent at a FM|I interface. The electrical resistance of the CPP FM|I|FM junction is larger than that of the CPP FM|NM|FM junctions which makes MTJs valuable for practical applications. It worth mentioning that the TMR effect was discovered in 1975 by M. Jullière [16] before the GMR effect. In his pioneering experiments Jullière measured a nonzero TMR in an Fe|Ge-oxide|Co system. Unfortunately, these results were difficult to reproduce<sup>4</sup> and it took about 20 years for experimentalists to make a system with a reproducible TMR effect. Successful room temperature magnetic tunneling transport measurements in CoFe|AlO<sub>x</sub>|Co junctions were performed by Moodera [17] in 1995. These results strongly accelerated study of spin-transport due to possible applications to magnetic sensors and magnetic memories. Aluminum oxide was for almost 10 years the most suitable and commonly-used insulator barrier. MTJs based on Al<sub>2</sub>O<sub>3</sub> are now routinely fabricated with very reproducible characteristics. With a proper choice of materials and an optimized junction preparation the TMR ratio can reach 70% at room temperature [18]. Since the discovery of much higher values of TMR in epitaxial MgO-based MTJs, research in this area is focused on the study of these materials systems. First experiments performed by Parkin *et al.* [19] and Yuasa *et al.* [20] on MgO-based CPP tunnel junctions reported values of TMR exceeding 200%. New records for room temperature TMR are regularly reported and current record is about 500% for FeCoB|MgO|FeCoB junction with amorphous FeCoB electrodes [21]. For more details on the GMR and TMR effects we refer to a number of reviews [22–29].

The MR effects just discussed can be used to make magnetic sensors and magnetic memories. The variation of electric resistance is used to detect small changes in magnetic fields by magnetoelectronic devices that can be found inside all modern computers and laptops: modern hard drives use a GMR spin valve, a device that reads information from disks. Such magnetic reading heads can be made small which enabled a thousand fold increase in the storage capacity of disk drives since it was introduced in 1998. A couple of years ago, TMR read heads were introduced by Seagate for laptop and desktop drives. Nowadays, the TMR head is mature technology for hard disk drives. A different application of TMR could be a new type of computer memory known as a MRAM (Magnetoresistive Random Access Memory). In 2006,

<sup>4</sup>as mentioned by A.Fert in his Nobel lecture



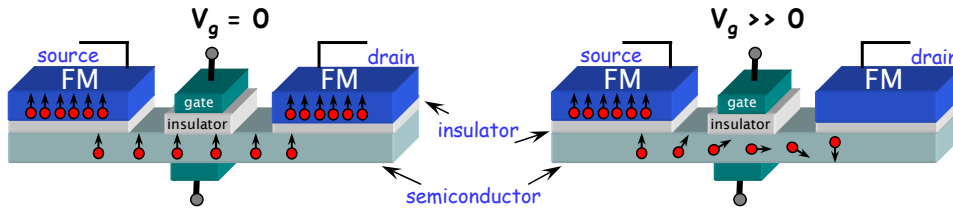


**Figure 1.5:** Datta-Das spin transistor. In the absence of gate voltage the electrons from FM source pass through the channel and are detected by the FM drain. With the gate voltage on, the electric field causes spins to precess (Rashba effect). Electrons with their spin misaligned with the drain magnetization direction are not detected as shown on the right.

the company Freescale began to market 1MB MRAM devices.

### 1.1.2 Spin injection into semiconductors

Since the 1970s conventional semiconductor microprocessors have operated with packets of electronic charge propagating along channels which are made smaller all the time. This progress is often summarized in Moore's Law according to which microprocessors will double in power every 18 months as more transistors are squeezed onto a chip. Although this trend will continue, it cannot continue forever as the size of individual devices approaches the dimension of atoms. This problem cannot be solved by spintronics. What spintronics could do is provide additional functionality such as programmable logic using the spin degree of freedom.

Many basic questions arise when attempts are made to combine semiconductors with magnetic metals in devices such as the field effect spin-transistor proposed in 1989 by Datta and Das [30]. Such a device consists of a semiconductor with a FM source to inject a current of spin-polarized electrons and a FM drain to detect spin-polarized electrons transported along a channel between them. This transistor is schematically shown in Fig. 1.5. As in a conventional field effect transistor there is a third electrode (gate) that generates an electric field to modulate the current in the two-dimensional transport channel by means of the Rashba effect. The magnetization directions of source and drain are assumed to be parallel. In case of zero gate voltage, every electron emitted from the source with its spin oriented along the magnetization direction should be able to enter the drain in the absence of spin flip during transport. When the gate voltage is non-zero the electric field causes the spins to precess. The electron current through the transistor is then modulated as the electrons with their spins not aligned with the direction of magnetization of the drain can not pass to the drain (Fig. 1.5 right panel). To realize this device requires: efficient injection of spin-polarized current from FM into SC; transfer of electrons through SC without losing their spin; detection of a spin-polarized current by FM electrode [31]. Already

the realization of efficient spin injection appeared to be rather difficult. Because the conduction electrons in a FM is spin-polarized, the most straightforward thing to try is to inject spins directly from FM into SC via an ohmic contact. However, it was shown experimentally that the efficiency of spin injection via ohmic contact into a SC is not large. The problem has been identified as the “conductivity mismatch” [32] between FM and SC. The effectiveness of the spin injection depends on the ratio of the (spin-dependent) FM conductivity  $\sigma_{FM}$  and the spin-independent SC conductivity  $\sigma_{SC}$ . A substantial spin injection occurs if  $\sigma_{FM} \approx \sigma_{SC}$ . For typical FM and SC  $\sigma_{FM} \gg \sigma_{SC}$ , and the spin injection efficiency is small. This problem can be resolved by introducing an additional tunneling barrier [33] at the FM|SC interface (see Fig. 1.5) or by means of a Schottky barrier formed at FM|SC interface like in Fe|GaAs junction. In Chapter. 2 we study the spin-dependence of the intrinsic interface resistance and how it depends on interface disorder. As an alternative approach one can use diluted magnetic semiconductors as spin injectors. Diluted magnetic semiconductors, however, have limited practical application due to low (of the order of 100 K) Curie temperature [36, 37]. One can also use half-metallic ferromagnets [38] as the 100% spin-polarized ferromagnetic injectors, although these are challenging materials with which to work.

## 1.2 Computational scheme

The spintronic effects introduced in the previous section are manifestations of electron spin-filtering at the interface between a FM and various nonmagnetic materials, at a FM|I interface in the case of the TMR effect, and at a FM|SC interface in the case of spin injection. To study such spin-dependent transport of electrons in inhomogeneous mainly layered, transition metal magnetic materials we use a so-called first-principles computational scheme because it is material specific and requires no empirical input data.

Our computational scheme can be divided into two parts: (i) the self-consistent calculations of “atomic” potentials and the corresponding electronic band structure and (ii) the transport calculations. In the first part we use the “tight-binding linear muffin-tin orbitals” method to find the self-consistent solutions of the Kohn-Sham equation in the local density approximation. In the second part we use the “wave function matching” method to calculate the transmission probability amplitudes used to calculate the spin-dependent conductance (resistance) in the linear-response regime from the Landauer-Büttiker formalism. In the rest of this section we discuss the major points of our method in more detail.

### 1.2.1 Landauer-Büttiker formalism

For a quantitative study of spin-dependent transport we have to be able to calculate spin-dependent conductances (resistances). The conductance of a macroscopic conductor that obeys Ohm’s law can be written as

$$G = \sigma \frac{A}{L} = 1/R, \quad (1.1)$$

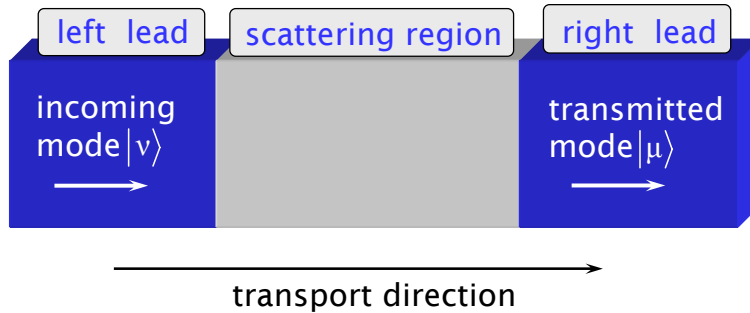


**Figure 1.6:** Schematic representation of a junction as a two-terminal device. Conductance through the scattering region (grey area) sandwiched between left and right semiinfinite leads with translational symmetry (dark areas on the left and right) can be expressed in terms of the transmission probability amplitudes  $t_{\mu,\nu}$  using the Landauer-Büttiker formula Eq. (1.2)

where  $A$  is the conductor cross section area,  $L$  is the length of the conductor,  $\sigma$  is its conductivity, and  $R$  is the electrical resistance. Eq. (1.1) does not hold on a scale shorter than the mean free path or when the wave character of electrons becomes dominant and electronic transport has to be treated quantum-mechanically. These corrections are taken into account by the Landauer-Büttiker scattering formalism [41–43] which we use to describe the electronic transport on mesoscopic scale. In the following we study electronic transport in a system that consists of a scattering region (an interface, junction etc.) connected by two semi-infinite ideal leads as shown in Fig. 1.6 to reservoirs (not shown). Landauer and Büttiker formulated the problem of electronic transport in terms of scattering matrices where the transmission matrix element  $t_{\mu,\nu}$  is the probability amplitude that a state  $|\nu\rangle$  incident on the scattering region from the left lead is scattered into a state  $|\mu\rangle$  in the right lead. Conductance in one spin channel in the linear response regime  $G = dI/dV|_{V=0}$  is then given by

$$G^{LB} = \frac{e^2}{h} \sum_{\mu,\nu} |t_{\mu,\nu}|^2 = \text{Tr}[\mathbf{t}\mathbf{t}^\dagger]. \quad (1.2)$$

The Landauer-Büttiker approach is intuitively very appealing because the electronic transport through nanostructures is naturally described in terms of transmission and reflection probability amplitudes. Explicit calculation of the scattering states is usually avoided by making use of the invariance properties of the trace in (1.2) to calculate the conductance directly from Green functions expressed in some convenient localized orbital representation [45]. Our computational scheme, however, allows us to calculate the full transmission and reflection matrices and to make explicit use of the scattering states to analyse the results.

## 1.2.2 Density Functional Theory

The transmission probability amplitudes (elements of the transmission matrix) can be calculated as soon as the incoming and transmitted modes are known. To find the full transmission matrix we have to find the wave function  $\Psi$  of a system, where  $\Psi$  is the solution of the Schrödinger equation

$$H\Psi = E\Psi, \quad (1.3)$$

and  $H$  is the Hamiltonian operator of the system under study. Analytical solution of (1.3) is only possible for very simple systems. To solve (1.3) for a system of many interacting particles, different methods have been developed. However, the only scheme capable of handling the complex systems we are interested in is the density functional theory (DFT) within the local density approximation (LDA). It is one of the most successful parameter-free, material-specific approaches in quantum mechanics giving an accurate description of the electronic ground state properties of a wide range of itinerant electron many-particle systems.

We start by considering a system that consists of  $N$  electrons and  $K$  ions. The Schrödinger equation for such a system is written as follows

$$H\Psi(\mathbf{r}_1, \mathbf{r}_2, \dots, \mathbf{r}_N) = E\Psi(\mathbf{r}_1, \mathbf{r}_2, \dots, \mathbf{r}_N), \quad (1.4)$$

where  $\mathbf{r}_i$  is the position operator of an electron. In specifying the Hamiltonian  $H$  we make use of the Born-Oppenheimer approximation and restrict ourselves to consideration of the electronic properties. The nuclear degrees of freedom are taken into account in the form of an external potential acting on the electrons, therefore, the wave function is an explicit function of the electronic coordinates only. The Born-Oppenheimer or adiabatic approximation is possible because nuclei are much heavier than electrons.  $H$  is then given by

$$H = \sum_{i=1}^N \left[ -\frac{\hbar^2}{2m} \nabla_i^2 + \frac{1}{2} \sum_{j \neq i}^N \frac{e^2}{|\mathbf{r}_i - \mathbf{r}_j|} + V_{\text{ext}}(\mathbf{r}_i) \right], \quad (1.5)$$

where the first term is the kinetic energy operator, the second term is the electron-electron interaction and the third term describes the electron-ion interaction.

The DFT which was first formulated by Hohenberg and Kohn [46] is based upon two theorems. The **first theorem** states that the energy of the interacting electron system in its ground state is a unique functional of the electron density

$$E[n(\mathbf{r})] = F[n(\mathbf{r})] + \int V_{\text{ext}}(\mathbf{r})n(\mathbf{r})d^3\mathbf{r}, \quad (1.6)$$

and the **second theorem** states that the density functional reaches its minimum at the exact ground state density  $n_{\text{GS}}(\mathbf{r})$  and the total energy of the ground state can be written as

$$E_{\text{GS}} = F[n_{\text{GS}}(\mathbf{r})] + \int V_{\text{ext}}(\mathbf{r})n_{\text{GS}}(\mathbf{r})d^3\mathbf{r}. \quad (1.7)$$

However, the DFT approach in the form of Eq. (1.7) is of a little practical use since the functional  $F$  is not known. The next step proposed by Kohn and Sham [47] was to map the complex system of many interacting particles in an external potential  $V_{\text{ext}}(\mathbf{r})$  onto a system of non-interacting particles in an effective potential  $V_{\text{eff}}(\mathbf{r})$ . For a system of non-interacting particles the electron density is given by the single-particle wave functions  $\psi_i$  as

$$n(\mathbf{r}) = \sum_{i=1}^N |\psi_i(\mathbf{r})|^2, \quad (1.8)$$

which can be obtained by solving a set of equations for  $N$  non-interacting particles

$$\left[-\frac{\hbar^2}{2m}\nabla^2 + V_{\text{eff}}(\mathbf{r})\right]\psi_i(\mathbf{r}) = \varepsilon_i\psi_i(\mathbf{r}), \quad (1.9)$$

in the effective potential

$$V_{\text{eff}}(\mathbf{r}) = V_{\text{ext}}(\mathbf{r}) + e^2 \int \frac{n(\mathbf{r}')}{|\mathbf{r} - \mathbf{r}'|} d^3\mathbf{r}' + \frac{\delta E_{\text{xc}}[n]}{\delta n(\mathbf{r})}. \quad (1.10)$$

Eqs. (1.8-1.10) are the so-called Kohn-Sham equations and they have to be solved self-consistently. Formally, these equations allow an exact treatment of the many-body system in the ground state. In the last term of Eq. (1.10)  $E_{\text{xc}} = E_x + E_c$  is the exchange-correlation energy. It is the only unknown term in the Kohn-Sham equations and an approximation has to be made in order to make further progress. Kohn and Sham proposed to use knowledge of the total energy of the homogeneous interacting electron gas of density  $n$  to define an exchange-correlation energy per electron  $\varepsilon_{\text{xc}}(n)$ . This approach is called the Local Density Approximation (LDA) for the exchange-correlation energy functional  $E_{\text{xc}}$  of the inhomogeneous systems with density  $n(\mathbf{r})$ . According to this approximation the exchange-correlation energy of an inhomogeneous system is approximated in terms of  $\varepsilon_{\text{xc}}(n)$  as

$$E_{\text{xc}}^{\text{LDA}} = \int n(\mathbf{r})\varepsilon_{\text{xc}}(n(\mathbf{r}))d\mathbf{r}, \quad (1.11)$$

There are several schemes available within the LDA for parameterizing the exchange-correlation energy. The most frequently employed parameterizations are due to von Barth and Hedin [48], Ceperley and Alder [49] as parameterized by Perdew and Zunger [50] and Vosko, Wilk and Nusair [51].

### 1.2.3 Tight-Binding Muffin-Tin Orbitals

In the previous subsection the problem of finding a solution of the Schrödinger equation for an interacting many-particle system was reduced to the problem of finding a solution of the Kohn-Sham equations for a system of non-interacting particles. Here, we briefly discuss the method which we use to solve the Kohn-Sham equations self-consistently.

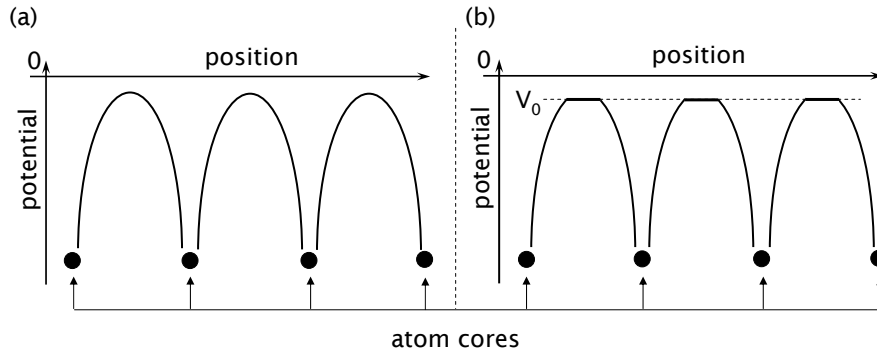


**Figure 1.7:** (a) Atomic potentials in a crystalline structure, and (b) the muffin-tin approximation to this potential. In the interstitial regions between the atoms the potential is set to constant  $V_0$ .

There are many different basis sets which can be used to express the Kohn-Sham wavefunctions. For practical purposes the basis set is always truncated. On the one hand the accuracy of calculations depends on the size of a basis set. On the other hand the size of a basis set determines the computational effort that is required. We are interested in studying both ideal and, more realistic, disordered systems consisting of many atoms. This requires use of as small a basis set as possible. The small size should not prevent us from treating complex electronic structures (like ferromagnetic metals) efficiently. These requirements are met by the tight-binding linearized muffin-tin orbitals (TB LMTO) method which forms a flexible, minimal basis set leading to highly efficient computational schemes for solving the Kohn-Sham equations [52–54]. We use the TB-LMTO surface Green function approach which is suitable to study the electronic structure of interfaces and layered systems. When combined with the coherent-potential approximation, it allows self-consistent calculation of the electronic structure, charge and spin densities of layered materials with disorder [55]. Below we review the TB-LMTO method in more detail.

To introduce the muffin-tin orbitals (MTO) we begin with an observation about the external electrostatic potential  $V_{\text{ext}}(\mathbf{r})$  sketched in Fig. 1.7(a). As can be seen from the figure, the potential can be divided into two parts: a rapidly changing part in a region near the atomic cores and a smoothly varying part between the atoms (the interstitial region). It suggests approximating the external potential by the spherically symmetric potential  $V_{\text{ext}}(\mathbf{r}) \rightarrow V_{\text{ext}}(r)$  within each sphere, and constant potential  $V_{\text{ext}}(\mathbf{r}) \rightarrow V_0$  in the interstitial region as shown in Fig. 1.7(b). This so-called “muffin-tin potential” was introduced by Slater in 1937 [56]. The muffin-tin potential allows for considerable simplification, since the wavefunction can be represented in terms of the solutions of the Schrödinger equation in each region: product of spherical harmonics and radial wave functions inside the sphere and plane

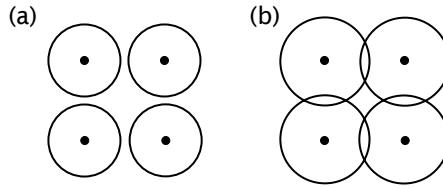


**Figure 1.8:** (a) Illustration of the “muffin-tin” approximation of the effective potential of a simple square lattice. It allows representing wavefunctions differently in the different regions. (b) Illustration of the atomic sphere approximation (ASA) in which the muffin-tin spheres are chosen such that their total volume is equal to the volume of a crystal. In both cases black dots correspond to atom cores. The ASA can be used for both close-packed and open structures. In the former case so-called “empty spheres” are used to make the open structures close-packed.

waves in the interstitial region.

In 1971 Andersen [57] proposed a new minimal, atom-centered basis set. In the following we concentrate on the atomic spheres approximation (ASA) where (i) the radius of muffin-tin spheres is expanded until they fill all the space (compare the muffin-tin spheres and atomic spheres in Fig. 1.8(a) and Fig. 1.8(b), respectively) and (ii) the kinetic energy in the interstitial region is taken to be zero  $\kappa = \sqrt{E - V_0} = 0$ . On the one hand, the MTO-ASA approach results in the simplest version of the MTO equations which allows dramatic simplification of electronic band structure calculation demonstrated below. On the other hand, it also gives accurate results especially for close-packed structures.

The MTO-ASA approach can be understood by just considering a single atomic sphere with a flat potential in all space outside the sphere. We mentioned above that the effective potential inside an atomic sphere of radius  $s$  is spherically symmetric, therefore, the wave function inside the spheres can be found by solving numerically the radial Schrödinger equation<sup>5</sup>. Outside the spheres the wave function is a solution of the Laplace equation  $\nabla^2\Psi = 0$  which can also be solved in spherical coordinates. The energy dependent MTO can be written as

$$\Phi_L(\varepsilon, \mathbf{r}) = i^l Y_L(\hat{r}) \begin{cases} u_l(\varepsilon, r) & \text{if } r \leq s; \\ \left[ \frac{D_l + l + 1}{2l + 1} \left(\frac{r}{s}\right)^l + \frac{l - D_l}{2l + 1} \left(\frac{r}{s}\right)^{-l-1} \right] u_l(\varepsilon, s) & \text{if } r > s, \end{cases} \quad (1.12)$$

where  $L$  stands for both  $l$  and  $m$  quantum numbers,  $u_l(\varepsilon, r)$  is a solution of the radial Schrödinger equation and  $Y_L(\hat{r})$  is a spherical harmonic.  $D_l(\varepsilon) = s u_l'(\varepsilon, s) / u_l(\varepsilon, s)$  is the logarithmic derivative of  $u_l(\varepsilon, r)$  at  $r \equiv s$ . However, this function can not be normalized because of  $(r/s)^l$  “tail” outside the atomic sphere. By subtracting from

<sup>5</sup>Spherical symmetry allows us to separate the Schrödinger equation into angular and radial parts

(1.12), both inside and outside the atomic sphere, the  $(r/s)^l$  term which is irregular at infinity, a new orbital is formed which is regular, continuous and differentiable in all space

$$\phi_L(\varepsilon, \mathbf{r}) = i^l Y_L(\hat{r}) \begin{cases} \frac{2l+1}{l-D_l} \frac{u_l(\varepsilon, r)}{u_l(\varepsilon, s)} - \frac{P_l(\varepsilon)}{2(2l+1)} \left(\frac{r}{s}\right)^l & \text{if } r \leq s; \\ \left(\frac{r}{s}\right)^{-l-1} & \text{if } r > s, \end{cases} \quad (1.13)$$

where the so-called potential function  $P_l(\varepsilon)$  is

$$P_l(\varepsilon) = 2(2l+1) \frac{D_l(\varepsilon) + l + 1}{D_l(\varepsilon) - l}. \quad (1.14)$$

Note that Eq.(1.13) is no longer a solution of the Schrödinger equation inside the atomic sphere because of the  $(r/s)^l$  term.

We now consider a crystal by centering an atomic sphere on every atom as illustrated in Fig. 1.8(b). Inside every atomic sphere the wave function is the sum of the “head function” given by Eq. (1.13) for  $r \leq s$  and “tails” of the MTO given by Eq. (1.13) for  $r > s$  coming from the other atomic spheres. However, we know that the solution of the radial equation inside an atomic sphere is  $u_l(\varepsilon, r)$ . Therefore, the linear combination of MTOs centered on different atoms given by

$$\Psi(\varepsilon, \mathbf{r}) = \sum_{R,L} \phi_L(\varepsilon, \mathbf{r}_R) C_{RL}, \quad (1.15)$$

will be a solution of the Schrödinger equation for the crystal if all of the  $(r/s)^l$  terms cancel on the central site. If we expand the tails from sites  $\mathbf{R}' \neq 0$  on the central site as

$$i^l Y_L(\hat{r}_R) \left(\frac{r_R}{s}\right)^{-l-1} = - \sum_{L'} \left(\frac{r_{R'}}{s}\right)^{l'} \frac{1}{2(2l'+1)} i^{l'} Y_{L'}(\hat{r}_{R'}) S_{R'L',RL} \quad (1.16)$$

where  $\mathbf{r}_R \equiv \mathbf{r} - \mathbf{R}$ ,  $r_R \equiv |\mathbf{r} - \mathbf{R}|$  and  $S_{R'L',RL}$  are the expansion coefficients called structure constants, then this so-called “tail-cancellation condition” can be expressed as

$$\sum_{R',L'} [P_{RL}(\varepsilon) \delta_{RR'} \delta_{LL'} - S_{RL,R'L'}] C_{R'L'} = 0. \quad (1.17)$$

All information about the crystal structure is contained in the structure constants  $S_{RL,R'L'}$ , and all information about the atomic potentials is in the potential functions  $P_{RL}(\varepsilon)$ . This equation can be used to determine the electronic band structure  $\varepsilon(\mathbf{k})$  if the summation of  $R'$  in (1.17) is over all sites in a crystal and the wavefunction is a Bloch state.

By introducing a set of “screening” parameters  $\{\beta_l\}$  as follows

$$P^\beta(\varepsilon) = P(\varepsilon) (1 - \beta P(\varepsilon))^{-1}, \quad (1.18)$$

and

$$S^\beta = S (1 - \beta S)^{-1}, \quad (1.19)$$



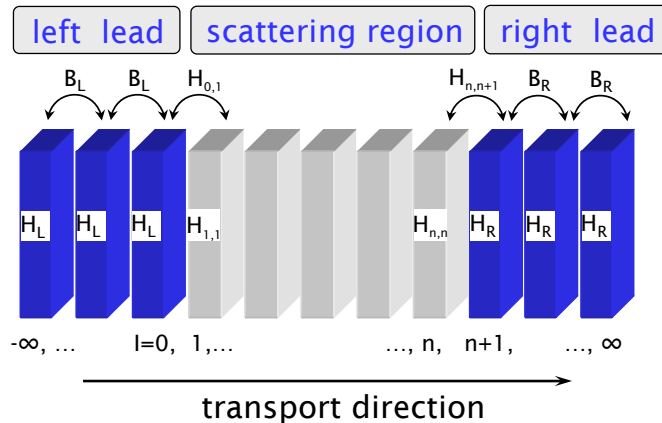


**Figure 1.9:** Tight-binding model of an infinite junction divided into slices (principal layers). The left and right ideal leads span the cells from  $I = -\infty, \dots, 0$  and  $I = n + 1, \dots, \infty$ , respectively. Scattering region spans cell  $I = 1, \dots, n$ . Leads are characterized by the on-site and hopping matrix elements  $H_{L/R}$  and  $B_{L/R}$ . The scattering region has site-dependent matrix elements  $H_{I,I}$  and  $H_{I,J}$ .

a short range (“tight-binding”) MTO (TB-MTO) can be defined [52–54] allowing us to consider only the first and second nearest neighbors in the case of close-packed structure. It turns out that the form of the tail-cancellation condition remains unchanged when rewritten with the screening transformation. A big disadvantage of Eq. (1.17) is that it contains an energy dependence in the potential function  $P^\beta(\varepsilon)$  which complicates the calculation of the band structure from Eq. (1.17). The problem can be solved using energy-independent, Linearized MTOs (LMTO). However, for transport calculations we need to know only the potential function at the Fermi energy, therefore, the linearization is only used for the self-consistent calculations.

#### 1.2.4 Wave function matching

In the previous subsection a brief description of the method we use to solve the Kohn-Sham equations was presented. However, the electronic transport problem for the infinite system consisting of the scattering region (an interface, junction etc.) sandwiched between two semi-infinite ideal leads (which have perfect lattice periodicity; see Fig. 1.6) can not be solved directly. Here we review the wave-function matching (WFM) method [58] used to calculate the transmission and reflection matrices [15]. In this method the semi-infinite leads are replaced by appropriate energy dependent boundary conditions, which allows us to reduce an infinite system to a system of finite size. More details of the formalism can be found in [15, 59–61].

We start by setting up a tight-binding representation of the Hamiltonian and

divide the system into slices (“principal layers”) perpendicular to the transport direction (see Fig. 1.9). A principal layer is a slice chosen so thick that there is only an interaction between neighbouring slices. The thickness of a principal layer depends on the spacial extent of the basis, the more localized the better. Then the Schrödinger equation has the form of an infinite chain of equations with  $I$  (a composite layer index) running from  $-\infty$  to  $\infty$

$$-H_{I,I-1}\mathbf{c}_{I-1} + (E\mathbf{I} - H_{I,I})\mathbf{c}_I - H_{I,I+1}\mathbf{c}_{I+1} = 0, \quad (1.20)$$

where  $\mathbf{c}_I$  is a vector containing the wave function coefficients and  $H_{I,I}$  and  $H_{I,I\pm 1}$  are the on-site and hopping matrices of the Hamiltonian, respectively.  $\mathbf{I}$  is the identity matrix. By construction the Hamiltonian matrix is the same for each slice in the leads  $H_{I,I} \equiv H_{L/R}$ ,  $H_{I,I-1} \equiv B_{L/R}$ , and  $H_{I,I+1} \equiv B_{L/R}^\dagger$  for left/right leads respectively (see Fig. 1.9). Using the tail-cancellation condition (1.17) instead of the Hamiltonian (1.20), we have

$$-S_{I,I-1}^{\mathbf{k}_\parallel}\mathbf{C}_{I-1} + [P_{I,I}(\varepsilon) - S_{I,I}^{\mathbf{k}_\parallel}]\mathbf{C}_I - S_{I,I+1}^{\mathbf{k}_\parallel}\mathbf{C}_{I+1} = 0, \quad (1.21)$$

where  $\mathbf{C}_I \equiv C_{IRL}$  is a vector of size  $M$  which is a product of the number of orbitals per atom  $(l_{max} + 1)^2$  ( $l_{max} = 2$  i.e.  $s, p, d$  basis set in most of our calculations) times the number of atoms (sites) per principal layer. We have assumed two-dimensional translational symmetry in-plane and

$$S_{I,J}^{\mathbf{k}_\parallel} = \sum_{\mathbf{T} \in \{\mathbf{T}_{I,J}\}} S^\beta(\mathbf{T}) e^{i\mathbf{k}_\parallel \mathbf{T}}, \quad (1.22)$$

is the Bloch summation of the screened structure constant matrix over the set of vectors  $\mathbf{T}_{I,J}$  that connects one lattice site in the  $I$ -th layer with lattice sites in layer  $J$ . Screening parameters  $\beta$  are chosen to minimize the range of hopping. Potential functions  $P_{I,I}$  and  $S_{I,J}^{\mathbf{k}_\parallel}$  are  $M \times M$  matrices,  $P_{I,I}$  is diagonal. Explicit reference to  $\mathbf{k}_\parallel$ ,  $\varepsilon$  and  $\beta$  is omitted from now on.

Following Ando the first step is to find solutions for the left and right leads. The periodicity in the leads imposes Bloch symmetry on the lead solutions (modes) i.e.  $\mathbf{C}_I = \lambda\mathbf{C}_{I-1}$  and  $\mathbf{C}_{I+1} = \lambda^2\mathbf{C}_{I-1}$ , where  $\lambda$  is the Bloch factor. Substituting this into Eq. (1.21) written for  $I = -\infty, \dots, -1$  and  $I = n+2, \dots, \infty$  i.e. for the left and right leads, respectively transforms Eq. (1.21) into a generalized linear eigenvalue problem for  $\lambda$ . By calculating the eigenvectors and velocities of the lead modes for a given energy (usually the Fermi energy) and  $\mathbf{k}_\parallel$ , the right- and left-going propagating and evanescent modes can be found<sup>6</sup>.

Let  $\mathbf{u}_1(-), \dots, \mathbf{u}_M(-)$  stand for the left-going solutions of  $\mathbf{C}_0$  corresponding to eigenvalues  $\lambda_1(-), \dots, \lambda_M(-)$  and  $\mathbf{u}_1(+), \dots, \mathbf{u}_M(+)$  the right-going solutions of  $\mathbf{C}_0$  corresponding to eigenvalues  $\lambda_1(+), \dots, \lambda_M(+)$ . Define the matrix  $U(\pm)$  as

$$U(\pm) = [\mathbf{u}_1(\pm) \dots \mathbf{u}_M(\pm)], \quad (1.23)$$

<sup>6</sup>for the evanescent modes  $|\lambda| \geq 1$ , and for the propagating modes  $|\lambda| = 1$

and the matrix  $\Lambda(\pm)$  as the diagonal matrix with elements  $\lambda_1(\pm), \dots, \lambda_M(\pm)$ . Following Ando, we introduce the matrix of Bloch factors (including evanescent states)

$$\mathbf{F}(\pm) \equiv U(\pm)\Lambda_{\pm}U^{-1}(\pm). \quad (1.24)$$

By means of this  $\mathbf{F}$  matrix it is possible to translate a general solution of Eq. (1.21) from layer  $J$  to layer  $I$  in the leads using the recursion relation

$$\mathbf{C}_I(\pm) = \mathbf{F}^{I-J}(\pm)\mathbf{C}_J(\pm). \quad (1.25)$$

We now consider the scattering problem. The scattering region is defined by  $I = 1, \dots, n$ , see Fig. 1.9. Using the recursion relation Eq. (1.25) for states in the leads we can write

$$\begin{aligned} \mathbf{C}_{-1} &= \mathbf{F}_L^{-1}(+)\mathbf{C}_0(+) + \mathbf{F}_L^{-1}(-)\mathbf{C}_0(-) \\ &= [\mathbf{F}_L^{-1}(+) - \mathbf{F}_L^{-1}(-)]\mathbf{C}_0(+) + \mathbf{F}_L^{-1}(-)\mathbf{C}_0, \end{aligned} \quad (1.26)$$

with  $\mathbf{C}_0 = \mathbf{C}_0(+) + \mathbf{C}_0(-)$  and

$$\mathbf{C}_{n+2} = \mathbf{F}_R(+)\mathbf{C}_{n+1}(+) + \mathbf{F}_R(-)\mathbf{C}_{n+1}(-), \quad (1.27)$$

where the subscripts L and R distinguish between the  $\mathbf{F}$  matrices of the left and right leads. Equations (1.26) and (1.27) truncate the infinite chain of equations Eq. (1.21) from the left and right side, respectively, because  $\mathbf{C}_{-1}$  and  $\mathbf{C}_{n+2}$  can be eliminated from the chain. To set up the boundary conditions the vector  $\mathbf{C}_0(+)$  is treated as the incoming wave,  $\mathbf{C}_0(-)$  stands for the reflected wave and  $\mathbf{C}_{n+1}(+)$  is a transmitted wave. We also assume that there is no incoming wave from the right lead by setting  $\mathbf{C}_{n+1}(-) = 0$

Having set the boundary conditions we can rewrite Eq. (1.21) using Eqs. (1.26) and (1.27) in the new region  $I = 0, \dots, n+1$

$$-S'_{I,I-1}\mathbf{C}_{I-1} + [P_{I,I} - S'_{I,I}]\mathbf{C}_I - S'_{I,I+1}\mathbf{C}_{I+1} = Q_I\mathbf{C}_0(+), \quad (1.28)$$

with a modified structure constants matrix  $S'$  whose matrix elements are identical to those of the original structure constant matrix, except for the first and the last diagonal elements, which are

$$S'_{0,0} = S_{0,0} + S_{0,-1}\mathbf{F}_L^{-1}(-); \quad S'_{n+1,n+1} = S_{n+1,n+1} + S_{n+1,n+2}\mathbf{F}_R(+). \quad (1.29)$$

$Q$  is a “source” vector of length  $n+2$ , whose elements are zero, except for the first element

$$Q_0 = S_{0,-1}[\mathbf{F}_L^{-1}(+) - \mathbf{F}_L^{-1}(-)]. \quad (1.30)$$

Eq. (1.28) describes the wave function in the scattering region which is matched to the wave functions in the leads. This procedure gives the name to the method.

To summarize, we have replaced an infinite dimensional problem, Eq. (1.21), by a finite dimensional one, Eq. (1.28). Now, the set of equations (1.28) can be solved using standard methods to find the total wave function  $C_I$ . The transmission probability

amplitude given by the amplitude of the wave function in the right lead normalized to the amplitude of the incoming wave can be written as follows

$$t_{\mu\nu} = \left( \frac{v_\mu}{v_\nu} \right)^{1/2} \{ U_R^{-1}(+) g_{N+1,0} S_{0,-1} [F_L^{-1}(+) - F_L^{-1}(-)] U_L(+)\}_{\mu\nu} \quad (1.31)$$

where  $g_{N+1,0}$  is a block of matrix elements of the Green function  $\mathbf{g} = (\mathbf{P} - \mathbf{S}')^{-1}$ , and  $v_\mu$ ,  $v_\nu$  are the components of the corresponding group velocities in the transport direction.

Finally we calculate the total conductance through the scattering region given by Eq. (1.2) using Eq. (1.31).

### 1.3 Thesis outline

In this thesis we study the influence of interface disorder on spin injection (into a semiconductor) and on tunneling magnetoresistance using the methods which were briefly described in the previous section. The experience gained doing this led us to propose a new material system with ideal spin injection and filtering properties.

In Chapter 2 we present a detailed study of spin injection from a ferromagnetic metal into a semiconductor choosing Fe|InAs and Fe|Au|InAs junctions. It has been suggested that in the absence of disorder a large spin-dependent interface resistance might solve the conductivity mismatch problem. However, interface disorder reduces the interface resistance significantly [34]. From our study we have found a decrease of the polarization of the current injected from Fe into InAs that is proportional to interface disorder. To prevent intermixing of FM and SC (interface disorder) we propose using a buffer layer of Au. We demonstrate a decrease in the sensitivity of the spin-dependent interface resistance to the interface disorder in the Fe|Au|InAs system.

In Chapters 3 and 4 we study transport in a semirealistic Fe|vacuum|Fe model tunneling junction. In particular we show that resonant tunneling plays an important role in this ideal magnetic tunnel junction. It dominates the conductance of the minority spin channel in the parallel configuration leading to huge values of the TMR. In Chapter 3 we study the effect of interface roughness and magnetic alloy disorder in the leads on the tunneling magnetoresistance and compare it with that of the ideal case. Observation of a new relation between the parallel and the antiparallel conductances has led us to a better understanding of Julliere's model. The results of this study are presented in Chapter 4.

In Chapters 5 and 6 we propose a completely new family of systems for spintronic devices. For minority spin electrons there is no overlap between the Fermi surface projections of graphite and Ni or Co (in both fcc and hcp cases) leading us to predict perfect spin-filtering at a graphite|FM(111) interface. We predict maximum magnetoresistance in a FM|graphite|FM(111) system. We also observe a weak sensitivity of the MR to interface roughness and alloy disorder. Furthermore, based on the fact that filtering occurs at one interface, we study systems like FM|graphite|NM(111) to demonstrate that perfect spin-injection (100% spin polarization of injected current)

into NM takes place. We hope that low temperature Andreev reflection experiments would allow this to be proved experimentally. From our first principles calculations we predict that two-dimensional hexagonal-BN and BC<sub>2</sub>N are a direct gap insulator and semiconductor, respectively. These results allow us to introduce new family of highly planar devices.

## Bibliography

- [1] W. Gerlach and O. Stern, Zeits. f. Physik **9**, 349 (1922).
- [2] O. Stern, Zeits. f. Physik **7**, 249 (1921).
- [3] G. Uhlenbeck and S. Goudsmit, Nature **117**, 164 (1926).
- [4] W. Pauli, Zeits. f. Physik **43**, 601 (1927).
- [5] P. Grünberg, R. Schreiber, Y. Pang, M. B. Brodsky, and H. Sowers, Phys. Rev. Lett. **57**, 2442 (1986).
- [6] S. S. P. Parkin, N. More, and K. P. Roche, Phys. Rev. Lett. **64**, 2304 (1990).
- [7] S. S. P. Parkin, R. Bhadra, and K. P. Roche, Phys. Rev. Lett. **66**, 2152 (1991).
- [8] S. S. P. Parkin, Phys. Rev. Lett. **67**, 3598 (1991).
- [9] M. N. Baibich *et al.*, Phys. Rev. Lett. **61**, 2472 (1988).
- [10] G. Binasch, P. Grünberg, F. Saurenbach, and W. Zinn, Phys. Rev. B **39**, 4828 (1989).
- [11] W. Thomson, Proc. Roy. Soc. of London **8**, 546 (1857).
- [12] N. F. Mott, Proc. R. Soc. London, Ser. A **153**, 699 (1936).
- [13] N. F. Mott, Proc. R. Soc. London, Ser. A **156**, 368 (1936).
- [14] N. F. Mott, Adv. Phys. **13**, 325 (1964).
- [15] K. Xia, M. Zwierzycki, M. Talanana, P. J. Kelly, and G. E. W. Bauer, Phys. Rev. B **73**, 064420 (2006).
- [16] M. Julliere, Phys. Lett. A **54**, 225 (1975).
- [17] J. S. Moodera, L. R. Kinder, T. M. Wong, and R. Meservey, Phys. Rev. Lett. **74**, 3273 (1995).
- [18] D. Wang, C. Nordman, I. M. Daughton, Z. Qian, and J. Fink, IEEE Trans. Mag. **40**, 2269 (2004).
- [19] S. S. P. Parkin *et al.*, Nature Materials **3**, 862 (2004).

- 
- [20] S. Yuasa, T. Nagahama, A. Fukushima, Y. Suzuki, and K. Ando, *Nature Materials* **3**, 868 (2004).
- [21] Y. M. Lee, J. Hayakawa, S. Ikeda, F. Matsukura, and H. Ohno, *Appl. Phys. Lett.* **90**, 212507 (2007).
- [22] M. A. M. Gijs and G. E. W. Bauer, *Adv. Phys.* **46**, 285 (1997).
- [23] J.-P. Ansermet, *J. Phys.: Condens. Matter.* **10**, 6027 (1998).
- [24] J. Bass and W. P. Pratt Jr., *J. Magn. & Magn. Mater.* **200**, 274 (1999).
- [25] E. Y. Tsymbal and D. G. Pettifor, *Solid State Physics* **56**, 113 (2001).
- [26] see the collection of articles, *Advances in condensed matter science, in Spin Dependent Transport in Magnetic NanoStructures*, edited by S. Maekawa and T. Shinjo Vol. 3, Taylor & Francis, London and New York, 2002.
- [27] E. Y. Tsymbal, O. N. Mryasov, and P. R. LeClair, *J. Phys.: Condens. Matter.* **15**, R109 (2003).
- [28] S. Yuasa and D. D. Djayaprawira, *J. Phys. D: Appl. Phys.* **40**, R337 (2007).
- [29] A. Brataas, G. E. W. Bauer, and P. J. Kelly, *Phys. Rep.* **427**, 157 (2006).
- [30] S. Datta and B. Das, *Appl. Phys. Lett.* **56**, 665 (1990).
- [31] I. Žutić, J. Fabian, and S. D. Sarma, *Rev. Mod. Phys.* **76**, 323 (2004).
- [32] G. Schmidt, D. Ferrand, L. W. Molenkamp, A. T. Filip, and B. J. van Wees, *Phys. Rev. B* **62**, R4790 (2000).
- [33] A. Fert and H. Jaffres, *Phys. Rev. B* **64**, 184420 (2001).
- [34] M. Zwierzycki, K. Xia, P. J. Kelly, G. E. W. Bauer, and I. Turek, *Phys. Rev. B* **67**, 092401 (2003).
- [35] D. L. Smith and R. N. Silver, *Phys. Rev. B* **64**, 045323 (2001).
- [36] H. Ohno *et al.*, *Appl. Phys. Lett.* **69**, 363 (1996).
- [37] F. Matsukura, H. Ohno, A. Shen, and Y. Sugawara, *Phys. Rev. B* **57**, R2037 (1998).
- [38] R. A. de Groot, F. M. Mueller, P. G. van Engen, and K. H. J. Buschow, *Phys. Rev. Lett.* **50**, 2024 (1983).
- [39] Y. V. Sharvin, *Zh. Eksp. Teor. Fiz.* **48**, 984 (1965), [*Sov. Phys. JETP* **21**, 655 (1965)].
- [40] B. J. van Wees *et al.*, *Phys. Rev. Lett.* **60** (1988), 848–850.

- 
- [41] R. Landauer, IBM J. Res. Dev. **1**, 223 (1957).
- [42] R. Landauer, Phil. Mag. **21**, 863 (1970).
- [43] M. Büttiker, Y. Imry, R. Landauer, and S. Pinhas, Phys. Rev. B **31**, 6207 (1985).
- [44] S. Datta, *Electronic Transport in Mesoscopic Systems* (Cambridge University Press, Cambridge, 1995).
- [45] C. Caroli, R. Combescot, P. Nozières, and D. Saint-James, J. Phys. C: Sol. State Phys. **4**, 916 (1971).
- [46] P. Hohenberg and W. Kohn, Phys. Rev. **136**, B864 (1964).
- [47] W. Kohn and L. J. Sham, Phys. Rev. **140**, A1133 (1965).
- [48] U. von Barth and L. Hedin, J. Phys. C: Sol. State Phys. **5**, 1629 (1972).
- [49] D. M. Ceperley and B. J. Alder, Phys. Rev. Lett. **45**, 566 (1980).
- [50] J. P. Perdew and A. Zunger, Phys. Rev. B **23**, 5048 (1981).
- [51] S. H. Vosko, L. Wilk, and M. Nusair, Canadian Journal of Physics **58**, 1200 (1980).
- [52] O. K. Andersen and O. Jepsen, Phys. Rev. Lett. **53**, 2571 (1984).
- [53] O. K. Andersen, O. Jepsen, and D. Glötzel, Canonical description of the band structures of metals in, in *Highlights of Condensed Matter Theory*, edited by F. Bassani, F. Fumi, and M. P. Tosi, International School of Physics ‘Enrico Fermi’, Varenna, Italy, pp. 59–176, North-Holland, Amsterdam, 1985.
- [54] O. K. Andersen, Z. Pawłowska, and O. Jepsen, Phys. Rev. B **34**, 5253 (1986).
- [55] I. Turek, V. Drchal, J. Kudrnovský, M. Šob, and P. Weinberger, *Electronic Structure of Disordered Alloys, Surfaces and Interfaces* (Kluwer, Boston-London-Dordrecht, 1997).
- [56] J. C. Slater, Phys. Rev. **51**, 846 (1937).
- [57] O. K. Andersen, in *Computational Methods in Band Theory* (Plenum, New York, 1971).
- [58] T. Ando, Phys. Rev. B **44**, 8017 (1991).
- [59] P. A. Khomyakov and G. Brocks, Phys. Rev. B **70**, 195402 (2004).
- [60] P. A. Khomyakov, G. Brocks, V. Karpan, M. Zwierzycki, and P. J. Kelly, Phys. Rev. B **72**, 035450 (2005).
- [61] M. Zwierzycki *et al.*, phys. stat. sol. B **245**, 623 (2008).





## Chapter 2

# Spin injection from Fe into InAs

*It has been proposed that the interface resistance of a defect-free (001) interface between bcc Fe and zinc blende semiconductors (such as GaAs, InAs or ZnSe) can be so large and spin-dependent [1, 2] that direct spin injection should be possible. In [2] however, it was pointed out that even a modest amount of interface disorder would be sufficient to destroy the spin-dependence. In this chapter, we extend our earlier ab-initio study to much lower concentrations of disorder. We show that the minority-spin transmission is very sensitive to local interface geometry and the factors governing the polarization quenching are identified in the dilute limit where a single Fe atom occupies an interface In or As site. In principle, the equilibrium geometry of these configurations could be determined by total energy minimization. However, because interface structures are frequently kinetically determined, there is no guarantee that the lowest energy configurations will dominate the interface transmission behaviour. Rather than attempting such a computationally very demanding total-energy study, we attempt to circumvent the problem entirely by inserting a buffer layer (BL) between Fe and InAs to prevent Fe minority-spin states coupling to the semiconductor directly while still preserving the transmission spin-polarization. We identify a candidate BL and demonstrate by explicit calculation that it preserves the transmission polarization of the ideal epitaxial structure remarkably well. Disorder at the Fe|BL interface are shown to have small effect on the large transmission polarization. However, we have found that spin polarization depends sensitively on the disorder at nonmagnetic BL|InAs interface. We expect the BL to work similarly for Fe|GaAs and Fe|MgO interfaces.*

### 2.1 Introduction

Achieving efficient injection of a spin-polarized current into a semiconductor is a necessary condition for realizing “spintronic” devices which combine traditional semicon-

ductor-based electronics with control over spin degrees of freedom. Thanks to the robustness (high Curie temperature,  $T_C$ ) of their magnetism, elemental metallic ferromagnets such as Fe, Co and Ni should be ideal sources of polarized electrons. Unfortunately devices based upon metals suffer from the “conductivity mismatch” problem [3]. The very large, spin-independent resistivity of the semiconductor dominates the potential drop throughout the device and the spin-dependent contribution of the metallic polarizer is by comparison negligible. One way around this problem is to use magnetic semiconductors but at the moment the Curie temperatures of these materials are still too low for practical applications. Another solution is to introduce a large spin-dependent interface resistance. To date, spin injection has been demonstrated in systems where such a resistance originates either from an intrinsic Schottky barrier (SB) (Fe|GaAs [4] and Fe|GaAlAs [5–7]) or from an additional insulating layer [8]. The record room temperature polarization for injection from metallic electrodes currently stands at 32% using the latter technique [9]. However, such barriers have drawbacks. They limit the maximum current which can be passed through the interface and can lead to large thermal dissipation at the interface. An ideal system for realizing spin-injection would be an Ohmic contact between a metallic ferromagnet and a semiconductor. One possible candidate is the Fe|InAs system. Unlike Fe and GaAs which are almost perfectly lattice matched, there is a large (5.4%) lattice mismatch between Fe and InAs. Nevertheless, it has been demonstrated that Fe films can be grown epitaxially on top of InAs [10, 11]. In spite of the absence of a Schottky barrier, it has been pointed out [2] that the interface resistance (IR) resulting from differences in the electronic structures is quite sizable and its spin dependence sufficiently large to overcome the conductivity mismatch problem. Unfortunately the spin-asymmetry of the transmission through a Fe|InAs interface was found to be quenched by disorder.

In this chapter we present a more detailed theoretical study of the Fe|InAs(001) system focussing on interfaces with low concentrations of substitutional impurities. We study the properties of a Fe|BL|InAs system with an additional buffer layer (BL) or bilayer introduced between Fe and InAs. The chapter is organized as follows. In the next section we describe the method used to calculate the interface resistance. Our new results on spin injection from Fe into InAs are given in Section 2.3 where we explicitly demonstrate that the quenching of spin injection is proportional to the interface disorder. In Section 2.4 we study the effect of a buffer layer introduced to reduce the sensitivity of spin polarization to interface disorder. We study the effect of disorder at both interfaces formed with the buffer layer and finish with some conclusions.

## 2.2 Method

The method we use is essentially the same as that employed in the earlier short study by Zwierzycki *et al.* [2] and discussed in more detail in [12]. In the first step, a potential profile for the Fe|InAs interface is calculated self-consistently within the local spin density approximation (LSDA) of density-functional theory (DFT).

This was done using the layer TB-LMTO (tight-binding linearized muffin-tin orbital) [13] surface Green's function (SGF) method [14] in the atomic-sphere approximation (ASA) [15]. Throughout this study the exchange and correlation potentials we use are those calculated by Ceperley and Alder [16] and parameterized by Perdew and Zunger [17]. The lattice mismatch between Fe ( $a_{\text{Fe}} = 2.866\text{\AA}$ ) and InAs ( $a_{\text{InAs}} = 6.058\text{\AA}$ ) was taken into account by tetragonally distorting iron so that the in-plane lattice constants of the two materials match. The height of the Fe unit cell was reduced in order to preserve its volume. The interlayer separation at the interface was calculated using the condition of local space-filling with atomic sphere radii kept at their bulk values. A similar procedure was used on introducing buffer layers.

Since the atomic spheres approximation (ASA) [15] for the potential works very well for close-packed solids, we adopt the usual procedure [18] of introducing additional "empty spheres" at the tetrahedral interstitial positions in the zinc blende (zb) structure, *i.e.* atomic spheres without nuclear charge, effectively converting the open diamond structure into a close-packed one where every sphere has eightfold coordination. Besides In and As atoms at  $(0, 0, 0)$  and  $(\frac{1}{4}, \frac{1}{4}, \frac{1}{4})$ , the unit cell of InAs then contains two types of empty spheres,  $E_1$  and  $E_2$  at  $(\frac{1}{2}, \frac{1}{2}, \frac{1}{2})$  and  $(\frac{3}{4}, \frac{3}{4}, \frac{3}{4})$  positions, respectively, all in units of InAs lattice constant. For simplicity, equal sphere sizes are used for In, As,  $E_1$  and  $E_2$ .

A well-documented deficiency of DFT is the failure of the Kohn-Sham eigenvalue spectrum to reproduce the single particle gap of even weakly correlated semiconductors and insulators. This is systematically and seriously underestimated in the LDA [19]. In particular, the experimental band gap of InAs is 0.42 eV [20] but no gap or a much smaller gap is found in LDA calculations. In our study, the gap in InAs was opened using a "scissor operator" correction applied as follows: an attractive constant term was added to the potential inside the As atomic sphere and the Kohn-Sham equations iterated to self-consistency. This procedure was carried out for different values of the constant until a value was found which reproduced the experimental band gap. Once the correct gap was obtained, the InAs and Fe electronic structures were lined up by applying a constant shift to the InAs potential until the bottom of the InAs conduction band ( $E_C$ ) and the Fermi energy ( $E_F$ ) were aligned. In most calculations we chose  $E_F - E_C = 0.02$  eV, corresponding to a doping concentration of about  $10^{17}\text{cm}^{-3}$ . The resulting band structure is plotted in Fig. 2.4(d) in the  $k_z$  direction for  $\mathbf{k}_{\parallel} = 0$ , *i.e.*, the  $\Gamma$ -X direction for bulk InAs or the point  $\bar{\Gamma}$  in the two-dimensional BZ (2D BZ). Since there are two Fe atoms in 2D unit cell, its 2D BZ is folded down and additional states, marked with dashed lines in Fig. 2.4(a,b), appear at  $\bar{\Gamma}$ . These states come from the corners of the unfolded 2D BZ and correspond to the P-N direction in the original 3D BZ.

In the second step, the self-consistent ASA potentials are used to calculate energy dependent transmission matrices using a TB-MTO wave-function matching [21] (WFM) scheme [12, 22]. The conductance (in units of  $e^2/h$ ) is given by the Landauer-Büttiker formula

$$G_{\sigma} = \sum_{\mu, \nu, k_{\parallel}} |t_{\mu\nu}(\mathbf{k}_{\parallel})|^2, \quad (2.1)$$

where  $t_{\mu\nu}(\mathbf{k}_{\parallel})$  is a transmission coefficient and  $\nu$  and  $\mu$  denote incoming and transmitted Bloch waves, respectively. The resistance  $R = 1/G$ , calculated as the inverse of the conductance given by Eq. 2.1, cannot be interpreted as an interface resistance because if this procedure is applied to an “interface” between two identical materials,  $R$  does not vanish. The reason is that the conductance (per unit area) of perfect crystalline materials is finite [23]. To calculate interface resistances (IR) we must use an expression derived by Schep *et al.* which corrects for the Sharvin conductance in the limiting case of two identical materials [24]:

$$R_{\text{Fe/InAs}} = \frac{h}{e^2} \left[ \frac{1}{\sum |t_{\mu\nu}|^2} - \frac{1}{2} \left( \frac{1}{N_{\text{Fe}}} + \frac{1}{N_{\text{InAs}}} \right) \right] \quad (2.2)$$

The first term is the inverse of the Landauer-Büttiker conductance and  $N_{\text{Fe(InAs)}}$  is the Sharvin conductance (in units of  $e^2/h$ ) of Fe (InAs). The integration over the 2D BZ is performed with a sampling density corresponding to  $10^6$  k-points for the  $1 \times 1$  interface unit cell. Disorder is modeled using lateral supercells [12, 22] with the potentials calculated using a version of the coherent potential approximation [14, 25] (CPA) generalized to treat disorder which is only homogeneous within a layer. Where necessary, a large number of disorder configurations (usually more than 10) was considered in order to estimate an error bar. To study low concentrations of disorder in this way, large supercells are required. In the present study, lateral supercells containing 32 In (or As) or 64 Fe atoms in each atomic layer were used.

Little is known about the microscopic structure of Fe|InAs interfaces. In particular, we are not aware of structure relaxation calculations for this system. However the results obtained for the closely related Fe|GaAs interface [26, 27] suggest that As-termination is energetically favorable for GaAs. Though experimental results [11] suggest the formation of an FeAs alloy at the Fe|InAs(001) interface, we will examine both terminations and model interface disorder as one layer of  $\text{Fe}_x\text{As}_{1-x}$  ( $\text{Fe}_x\text{In}_{1-x}$ ) with Fe substituting interfacial As (In) atoms in case of As (In) terminated InAs interface.

## 2.3 FeInAs revisited

It was shown in Ref. [2] that while a perfect Fe|InAs (001) interface acts as a very effective spin-filter, the spin-dependence of the interface transmission (or of the corresponding IR) is very sensitive to interface disorder. In particular, even the smallest amount of disorder considered at the time, corresponding to 1 in 8 In (or As) atoms substituted by Fe, was capable of quenching the polarization almost completely. It is natural to ask how much disorder can be tolerated while still maintaining an acceptable polarization. To answer this question we revisit the problem using larger lateral supercells that allow us to study concentrations of disorder 4 times lower than previously [2]. The results are summarized in Fig. 2.1, where in the top (bottom) left panels we show majority and minority conductances as a function of the number of As (In) atoms substituted by Fe for As (In)-terminated interfaces. The symbols denote the values calculated for various randomly generated configurations of disorder and the lines connect the average values. The corresponding IRs are shown

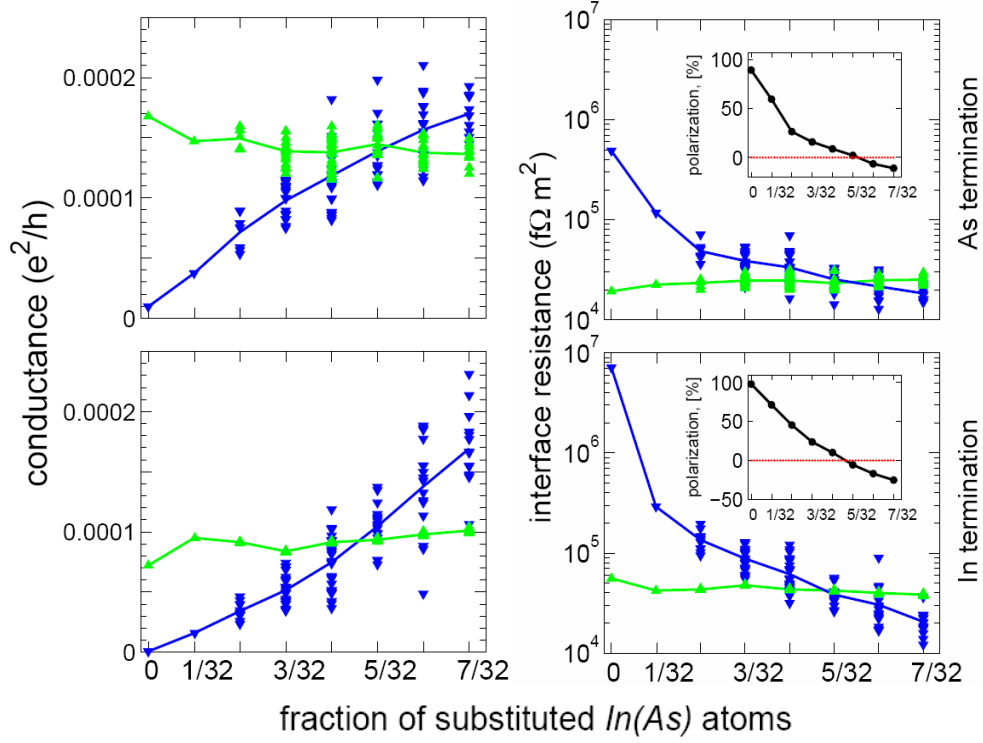


**Figure 2.1:** Conductance (on the left) and interface resistance (on the right) for As- (upper panels) and In-terminated (lower panels) FeInAs interfaces as a function of the fraction of interfacial In atoms substituted by Fe for majority ( $\blacktriangle$ ) and minority ( $\blacktriangledown$ ) spins. The green and blue lines connect the values averaged over configurations. Corresponding polarizations are shown in the insets.

in the panels on the right in Fig. 2.1 where the average polarizations are shown as insets. Starting with perfect interfaces, we see spin-polarizations approaching 100% for both interface terminations, with the majority channel dominating over a much less conducting minority channel. As explained in Refs. [1, 2], this is the result of a symmetry-related selection rule. For perfect  $\mathbf{k}_{\parallel}$ -preserving interfaces, transmission occurs only in the small area around the center of the 2D BZ ( $\bar{\Gamma}$  point) corresponding to the occupied states at the bottom of the InAs conduction band (see Fig. 2.4). At  $\bar{\Gamma}$ , these states have the full  $\Delta_1^{zb}$  symmetry of the  $C_{2v}$  group. The very similar  $\Delta_1$  states (of the  $C_{4v}$  symmetry group) in the Fe majority band can transmit into InAs very efficiently with probability approaching unity. In the Fe minority spin channel there are  $\Delta_{2'}$  states which are formally compatible with the InAs  $\Delta_1^{zb}$  symmetry states. However the differences in spatial distribution and orbital composition of these states (in-plane  $d_{xy}$  for  $\Delta_{2'}$  versus predominantly  $s$  and  $p_z$  for  $\Delta_1^{zb}$ ) reduces the

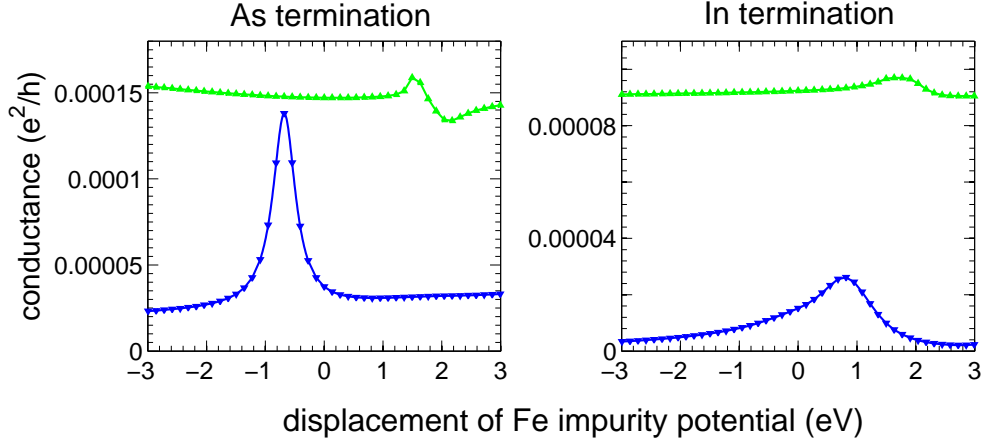


**Figure 2.2:** Conductance for As- (left panel) and In-terminated (right panel) Fe|InAs interfaces as a function of single Fe impurity potential shift in a supercell of 32 atoms for majority (▲) and minority (▼) spins.

transmission probability at  $\bar{\Gamma}$  to the  $10^{-2}$  range. As seen in Fig. 2.1 the introduction of disorder in the form of Fe substituting some of the interfacial In or As atoms, has a quite small effect in the majority channel. In the minority channel, the picture changes much more dramatically where disorder breaks the symmetry and overrides the selection rule which prevented transmission of minority spin states. This leads to the opening of new channels for transmission through the interface and the average conductance increases roughly in proportion to the fraction of substituted atoms, as seen in Fig. 2.1 for both As and In terminated Fe|InAs interfaces. The polarization, originally close to 100% and positive, decreases to zero at a disorder concentration of about  $5/32$  and becomes negative when the fraction of substituted atoms is increased. The increase of transmission in the minority channel occurs via diffusive scattering<sup>1</sup> which dominates the transmission even for the lowest concentration ( $1/32$ ) shown in Fig. 2.1 and accounts for 80% and 93% of the total value for As- and In-termination, respectively.

It might, however, be misleading to consider only average values of the transmission since some configurations of disorder presumably have a lower energy than others and may be present at the interface with a correspondingly higher probability. Fig. 2.1 exhibits a very substantial spread of values for microscopically different configurations of disorder, especially in the minority channel. In fact the distribution of values for majority and minority channels overlaps for concentrations above  $2/32$ . Interestingly, there seems to be a positive correlation between the value of the minority conductance and the degree of clustering of the Fe impurities.

The spread in conductances in Figs. 2.1 for different configurations of disorder

<sup>1</sup>By diffusive we mean scattering into the states with different  $\mathbf{k}_{\parallel}$ .

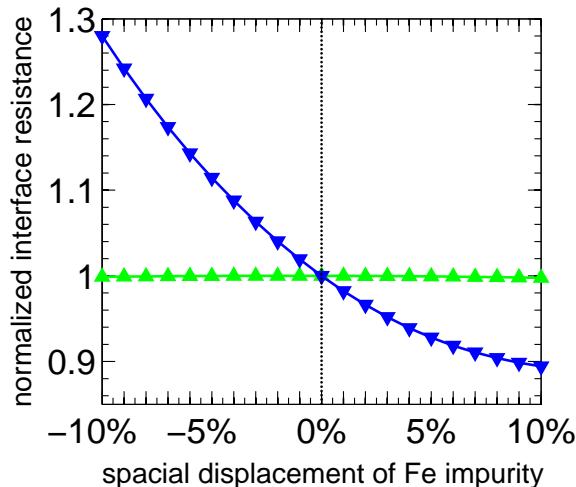


**Figure 2.3:** Normalized interface resistance of As-terminated and Fe|InAs interfaces as a function of a single Fe impurity displacement in  $4 \times 4$  lateral supercells in units of Fe|InAs interface distance for majority (▲) and minority (▼) spins.

indicates a strong sensitivity of the Fe|InAs interface transmission to fine details of the interface structure. If we were to allow the atoms to relax to their minimum energy configurations, it is conceivable that we would observe sizeable changes in the conductance. Since a geometry optimization for a system of this size is not possible [26, 27], we instead illustrate the sensitivity with model calculations in the spirit of a tight-binding Hamiltonian. We focus on the dilute limit of a single substitutional Fe atom on one of 32 interface In (or As) sites.

In the first of two model studies, we added, non self-consistently, a constant attractive or repulsive potential shift inside the atomic sphere of the single Fe impurity. The effect on the minority and majority conductances is shown in Fig. 2.2 as a function of the potential shift. The shift is seen to have only a limited effect in the majority channel. For minority spins however there are large resonant-like transmission peaks which can be moved in and out of resonance by the shift. The effect is especially large for As where it can lead to almost complete quenching of the polarization. Such features were not observed when the same potential shift was applied to one of the interface In (or As) atoms in the absence of Fe impurities. The potential shifts applied in Fig. 2.2 are of course entirely arbitrary. One can however imagine that they correspond qualitatively to changes in the position of Fe  $d$  state which might result from changes in the local geometry and chemical coordination of an Fe impurity if it were allowed to relax.

The sensitivity to the structure is further illustrated in Fig. 2.3 where we show the effect on the interface resistance of displacing a single Fe impurity along the (001) axis, perpendicular to the interface. The atomic sphere potential is not recalculated self-

consistently for each displacement but is displaced rigidly. Negative displacements correspond to displacements towards the Fe lead and positive ones in the direction of the InAs lead. Displacements are given in units of the Fe-InAs interfacial distance which is about  $1.4\text{\AA}$  in our calculations. The values of IR are given relative to their zero-displacement values. While the majority channel is not changed at all, the minority one varies by as much as 40% for the range of displacement studied.

In view of the great sensitivity of the transmission through an Fe|InAs interface to the details of its structure and composition, it is difficult to make any detailed interpretation of experimental observations without having much more information about the interfaces which were studied, or to make useful predictions if the interface structure and composition cannot be controlled experimentally. Though it is, in principle, possible to theoretically determine relaxed interface geometries by total energy minimization, in practice an extensive study of systems of this size are prohibitively expensive. Even if it were possible, the relevance of the results of such calculations to real experiments is doubtful because real interfaces are frequently metastable and their structures depend on the growth conditions, annealing etc. Even though Fig. 2.1 shows that spin-injection is in theory possible, it may be impossible to approach this limit in practice if Fe reacts with InAs during growth.

The resonant features of Fig. 2.2 indicate that the effectiveness with which Fe impurities facilitate forward scattering in the minority channel quenching the polarization, is determined in large part by the local electronic structure of the impurity and the way it bonds with the InAs host. This in turn suggests that the spin-injection properties of the system could be improved if Fe with its open  $d$ -shell were prevented from reacting with the InAs substrate during growth. In the following sections we study the properties of systems where such reactions are prevented by introducing a buffer layer (BL) of non-magnetic metal at the Fe|InAs interface.

## 2.4 Fe|BL|InAs system

A suitable buffer layer would be a nonmagnetic metal whose lattice constant matched those of both the ferromagnet and the semiconductor to permit epitaxial growth. It should not act as a barrier to transmission of  $\Delta_1$  states from Fe into InAs. The latter condition is met by *e.g.* noble metals with their Fermi level-crossing bands possessing  $\Delta_1$  symmetry along  $\Gamma - X$  direction. In the following we present calculations for a Au buffer layer. The lattice constants of fcc gold and bcc Fe are known to match very well and near perfect interfaces can be prepared experimentally. It has also been shown that, despite the lattice mismatch, crystalline Au can be grown on top of InAs [28]. In the following, we assume a thin layer of face-centered tetragonal Au whose in-plane lattice constant has been adjusted to match that of InAs. The out-of-plane lattice constant is chosen to preserve the volume of the bulk cubic unit cell with  $a_{\text{Au}} = 4.078\text{\AA}$ .



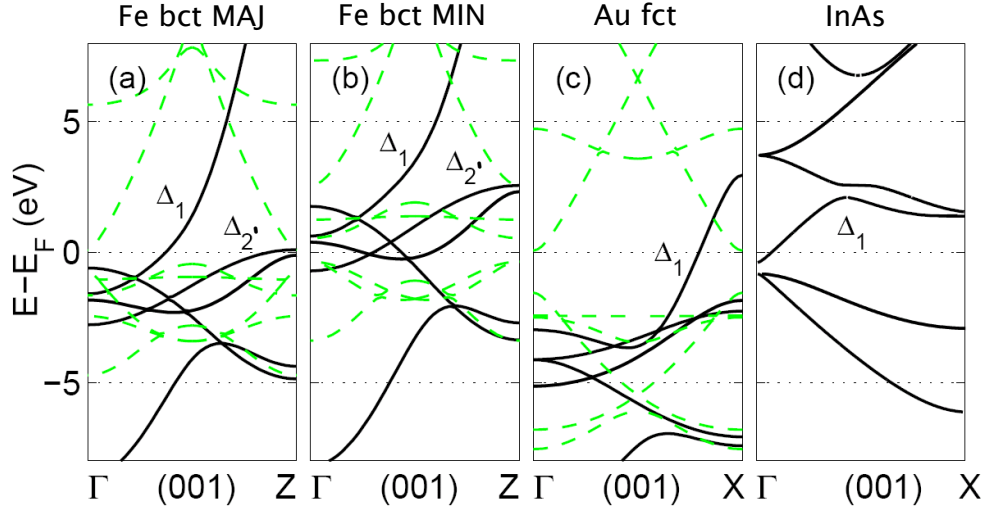


**Figure 2.4:** Band structure of Fe bct majority and minority, Au fct and InAs in (001) growth direction. Downfolded bands are marked with green dashed lines. Only unfolded bands are labeled with the names of their irreducible representations.

### 2.4.1 Ideal Fe|Au|InAs junction

We first present results for a junction with specular Fe|Au and Au|InAs interfaces. In Fig. 2.5 the conductance is shown as a function of the distance between the Fermi energy and the bottom of the InAs conduction band,  $E_F - E_C$ , for a junction with a five monolayer (ML) thick Au buffer layer. The Au layer should not have to be so thin that pinholes might occur during growth. It should not be so thick that spin-flip scattering becomes appreciable. Results for both In- and As-terminations are shown in the figure. We see that the polarization of injected current is higher than 90% for a wide range of values of  $E_F - E_C$ . We can understand these results in terms of the band structures shown in Fig. 2.4. In the center of the 2D BZ, the  $\Delta_1$  states of Au couple effectively with the states of the same symmetry in majority spin Fe and with  $\Delta_1^{zb}$  in InAs thus preserving the high transmission of the majority channel. The filtering of minority carriers on the other hand is even more effective than for pure Fe|InAs. Unlike the  $\Delta_1^{zb}$  states in InAs, the  $\Delta_1$  states of Au are strictly orthogonal to  $\Delta_{2'}$  in Fe which are thus forced to tunnel through the buffer layer to reach the semiconductor. These arguments only hold strictly for the states at  $\bar{\Gamma}$  where distinct symmetries are well defined. As  $E_F - E_C$  increases and a larger area of the 2D BZ around  $\bar{\Gamma}$  becomes occupied with InAs conduction band states, the effectiveness of the above selection rule decreases leading to a gradual reduction of the polarization.

The results shown in Fig. 2.5 were obtained for a single thickness of buffer layer, 5 ML of Au. Multiple reflections occur in ideal layered structure and can sometimes lead to substantial thickness-dependence of the transmission. Therefore, before pro-

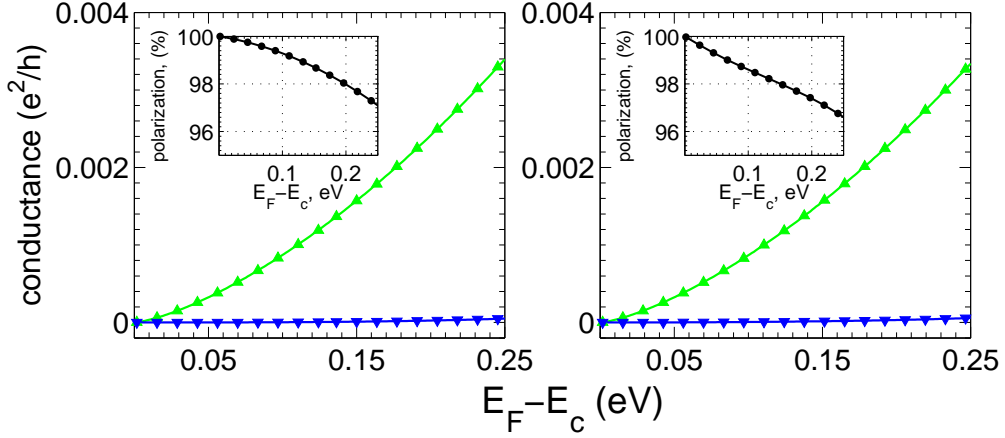


**Figure 2.5:** Conductance (in units of  $e^2/h$ ) through ideal Fe|Au5|InAs junction for As-terminated (left panel) and In-terminated (right panel) Au|InAs interfaces as a function of concentration of dopants in InAs for majority (▲) and minority (▼) spins. Corresponding polarizations are shown on the insets.

ceeding to study the effect of interface disorder, we should study how the results presented in Fig. 2.5 are modified by size effects. As just discussed, the situation in the majority channel is simple. The Au  $\Delta_1$  state matches the  $\bar{\Gamma}$  states in Fe and InAs very well and is therefore only very weakly confined within the buffer layer. We expect the modulation of the majority spin transmission probabilities to be very weak and, for finite values of  $E_F - E_C$ , to be washed out in course of the 2D BZ integration. Note that confinement occurring outside the central area of 2D BZ, where there are no states in InAs, will not affect transport properties. The minority spin channel, where Au  $\Delta_1$  states encounter the “symmetry gap” in Fe (see Fig. 2.4), is more complicated.

Fig. 2.6 shows the  $\Delta_1$ -symmetry local density of states (LDOS) on the interface Fe atoms at  $\mathbf{k}_{\parallel} = \bar{\Gamma}$  as a function of energy for a large range of Au thickness. A small imaginary part ( $z = 0.001$  Ry) was added to the energy in order to make the DOS plots smoother (transport calculations are performed for real energies). The top and bottom panels of the figure show the minority spin  $\Delta_1$ -symmetry bulk DOS for tetragonal Fe and cubic InAs, respectively. The symmetry gap in Fe for minority spin states with  $\Delta_1$ -symmetry can be seen in the vanishing DOS in the energy range -1 to +0.2 eV with respect to the Fermi energy in the top panel of the figure. The 0.42 eV InAs gap is clearly visible between -0.44 and -0.02 eV in the bottom panel. For junctions with more than 11 MLs of Au, the potentials were prepared non-self-consistently by repeating the potential of the central Au layer. For energies falling within the band gap of InAs, Au minority-spin  $\Delta_1$  states are perfectly confined inside the buffer layer leading to the formation of quantum well (QW) states, well documented in the literature [29]. These are visible in Fig. 2.6

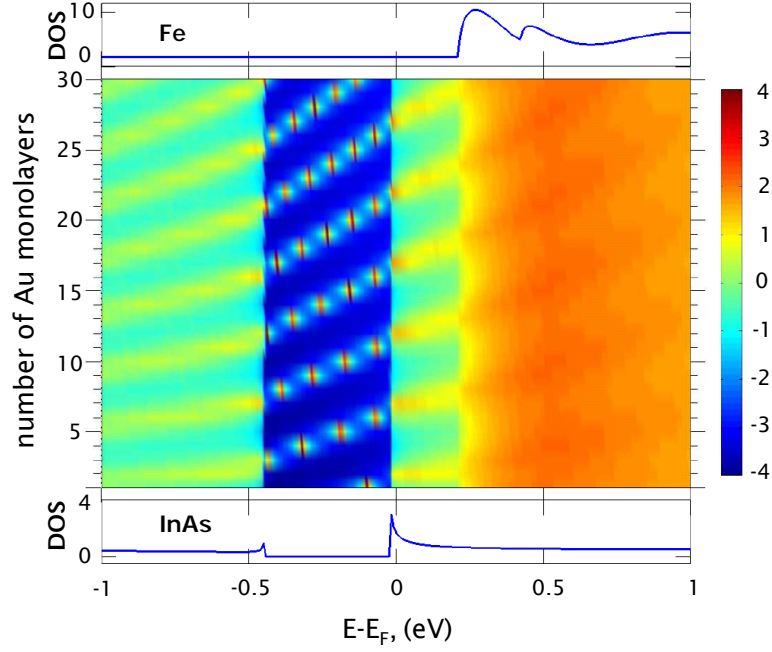


**Figure 2.6:** Local density of minority spin states with  $\Delta_1$  symmetry (on a logarithmic colour scale) for interface Fe atoms at the  $\Gamma$  point as a function of the energy and the thickness of the Au buffer layer. The minority spin local DOS for  $\Delta_1$ -symmetry states is shown on a linear scale for bulk Fe (upper panel) and InAs (lower panel).

as sharp, well quantized resonances. Below and above the InAs gap, Au states are able to spill into the semiconductor by coupling to the InAs  $\Delta_1^{zb}$  band. The sharp resonances are then replaced by a relatively weakly modulated DOS on the interface Fe atoms. At about 0.2 eV above the Fermi energy, the Fe  $\Delta_1$  symmetry gap ends, the Au minority-spin  $\Delta_1$  states are not confined on either side and changing the thickness of Au does not lead to any significant modulation of the interface Fe DOS. For the energies we are primarily interested in - low in the conduction band of InAs and in the Fe symmetry gap - the LDOS modulation visible on the logarithmic scale used in Fig. 2.6 is rather weak on an absolute scale and unlikely to substantially alter the transmission from the poorly matched  $\Delta_2'$  states of Fe. As we move away from  $\bar{\Gamma}$  and have to integrate over a larger region of reciprocal space about  $\bar{\Gamma}$ , the confinement at the Fe|Au interface decreases, the quantization becomes weaker (the maxima occurring at different energies) and the net effect decreases. To test the above picture explicitly, we calculated the conductance as a function of  $E_F - E_C$  for a range of buffer layer thicknesses (1 – 10 ML) and found no signs of  $\Delta_1$  QW effects in either spin-channel.

In the minority channel the downfolded “corner” states (dashed lines close to zero energy in Fig. 2.4(c)) are strongly confined within the Au layer leading to the formation of QW states with a symmetry different to the  $\Delta_1$  symmetry discussed in the context of Fig. 2.6. The confinement follows from a combination of the orbital character of these states (which is free-electron-like  $p_x, p_y$ ) and the in-plane Bloch phase coming from downfolding the states at the “corner” of the Au surface BZ onto the origin  $\bar{\Gamma}$  of the smaller, common interface BZ which is determined by the material with the largest lattice constant InAs. This Bloch phase factor dictates that even though the orbital composition of the Au states is qualitatively similar to that of the four  $\Delta_5$  states in the Fe minority band, the coupling between them is identically zero at  $\bar{\Gamma}$  and remains weak around it. If the Au “corner” states are brought down to the Fermi level, *e.g.* by altering the amount of the tetragonal distortion of Au, then resonant transport can occur, allowing minority  $\Delta_5$ -derived states in Fe to be transmitted into InAs for some values of  $\mathbf{k}_{\parallel}$ . The effect can lead to a substantial reduction of the polarization but occurs only for specific combinations of  $E_C - E_F$  and thickness of the Au buffer layer. Consequently it should be possible to avoid it in experiment, especially as it is unlikely to survive the presence of disorder.

## 2.4.2 Disordered Fe|Au|InAs junction

The next step is to study the effect of interface disorder on the transmission through a Fe|Au|InAs junction. We fix the Au thickness at 5 ML and start by introducing disorder at the magnetic Fe|Au interface while keeping the Au|InAs interface clean. We consider substitutional disorder with Fe impurities replacing Au on some interface sites. The calculated spin-dependent resistances are shown in Fig. 2.7 as a function of the fraction of the substituted Au atoms. Note that while the maximum fraction considered here (14/64) is formally the same as in Fig. 2.3, the actual areal density of impurities is twice as large here because there are twice as many Au atoms per unit area which can be substituted with Fe as there are In (or As) sites. We see the same main trends as we saw in Fig. 2.7: for both terminations the majority channel is almost unaffected by disorder while the minority resistances are substantially reduced. Comparing Figs. 2.3 and 2.7, we note, however, that the minority resistances are almost an order of magnitude larger than in the original Fe|InAs system. Consequently, average polarizations do not vanish as they did previously but remain positive. However, the configuration spread in the minority channel remains substantial and, for In termination, overlap with the majority values occurs.

As a further test of the stability of these results, calculations similar to those of Fig. 2.3 were performed by displacing a single Fe impurity perpendicular to the interface. The change in interface resistance is shown in Fig. 2.8 as a function of the displacement of one Fe impurity (1/64) given as a percentage of the Fe–Au distance (1.57 Å). Negative displacements are towards the Fe electrode, positive ones towards Au. The calculations were performed non-self-consistently and the resistances in the plot are normalized to their zero displacement values. Comparing Figs. 2.3 and 2.8 we see that the relative change in the minority channel is about 4 times smaller in the present case.

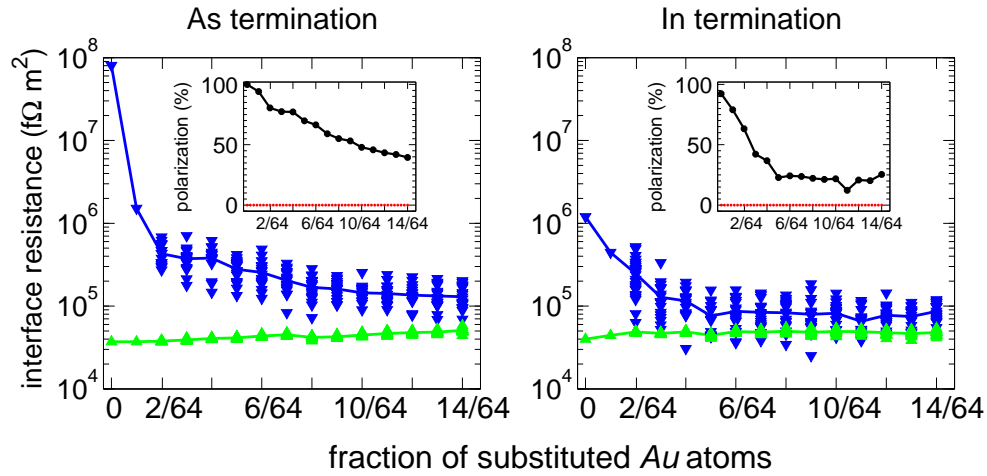


**Figure 2.7:** Interface resistance of As- (left panel) and In- (right panel) terminated Fe|Au|InAs junctions as a function of the fraction of interfacial Au atoms substituted by Fe for majority (▲) and minority (▼) spins.

Turning now to disorder at the non-magnetic Au|InAs interface, we consider two scenarios for substitutional disorder: (i) with In (As) atoms substituting Au in the buffer layer, for which results are shown in the left-hand panels of Fig. 2.9 and (ii) with Au atoms substituting In (As), for which results are shown in the right-hand panels of Fig. 2.9. The upper panels are for As termination, the lower panels for In termination. As before, the results for the majority spin case are quite insensitive to disorder and do not need to be discussed in any detail.

In scenario (i), the In (As) impurities can occupy either of two inequivalent sets of sites as there are two Au atoms for each In (As) interface atom. The two inequivalent sites are considered separately and the results are shown as filled and empty symbols for the minority spin case. Mixed configurations were not considered. The configuration averaged results, shown as continuous and dashed lines, scarcely differ for As termination (upper left) but are very different for In termination (lower left). For both terminations, the configuration averaged resistances for the majority and minority channels are well separated. The configuration spread for As-termination is exceptionally large for the sites depicted with open triangles and dashed line yielding zero polarization for some higher concentration configurations. Clearly, it would be important to establish the relative stability of the two different sites by determining the difference in their energies. Results for the second scenario, with Au substituting In or As interface atoms, are shown on the right-hand side of Fig. 2.9. The minority spin resistance is seen to be quenched much more rapidly by disorder at the non-magnetic interface than by disorder at the magnetic interface, with the average polarization dropping quickly to zero and becoming negative. For all but the

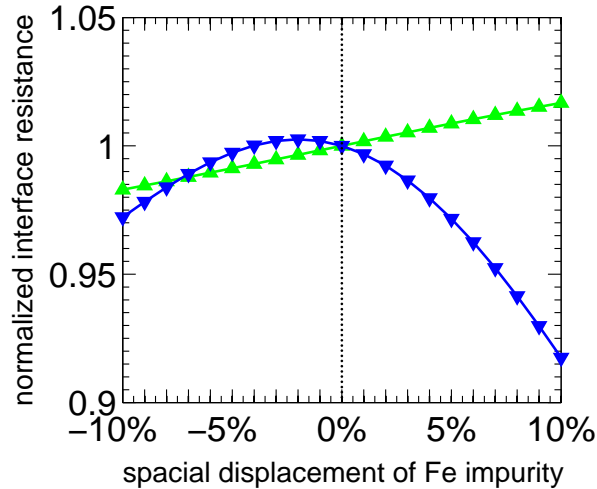


**Figure 2.8:** Normalized interface resistances of As-terminated Fe|Au<sub>5</sub>|InAs junction as a function of a single Fe impurity displacement in units of Fe|Au interface distance for majority (▲) and minority (▼) spins.

lowest concentrations of disorder considered, some minority-spin configurations have resistances which are lower than the majority spin resistance making it important to know whether such configurations are energetically favoured or not.

Comparison of Figs. 2.7 and 2.9 with Fig. 2.1 shows that overall, introducing a gold buffer layer leads to a higher minority channel interface resistance and a higher polarization for a given level of interface disorder. However, the results are also sensitive to the details of the interface disorder: the chemical nature of a substitution, its local atomic structure and how a given concentration of impurity atoms is configured. In many cases the spread of resistance values in the minority channel is very large, with resistances for some configurations overlapping with that of the majority channel, even when average values remain well separated. Surprisingly, the polarization seems to be more sensitive to the disorder at the non-magnetic Au|InAs interface. This is unfortunate because while it is probably possible to prepare nearly ideal Fe|Au interfaces [30], the same is less likely for the non-magnetic Au|InAs interface. The situation is also likely to deteriorate if there is disorder present at both interfaces simultaneously.

## 2.5 Conclusions

In this chapter an earlier study [2] of the effect of interface disorder on the transmission properties of Fe|InAs interfaces has been extended. In particular, it has been shown that for small concentrations of substitutional disorder, with Fe substituting interface In or As atoms, a proportionality between the minority spin conductance

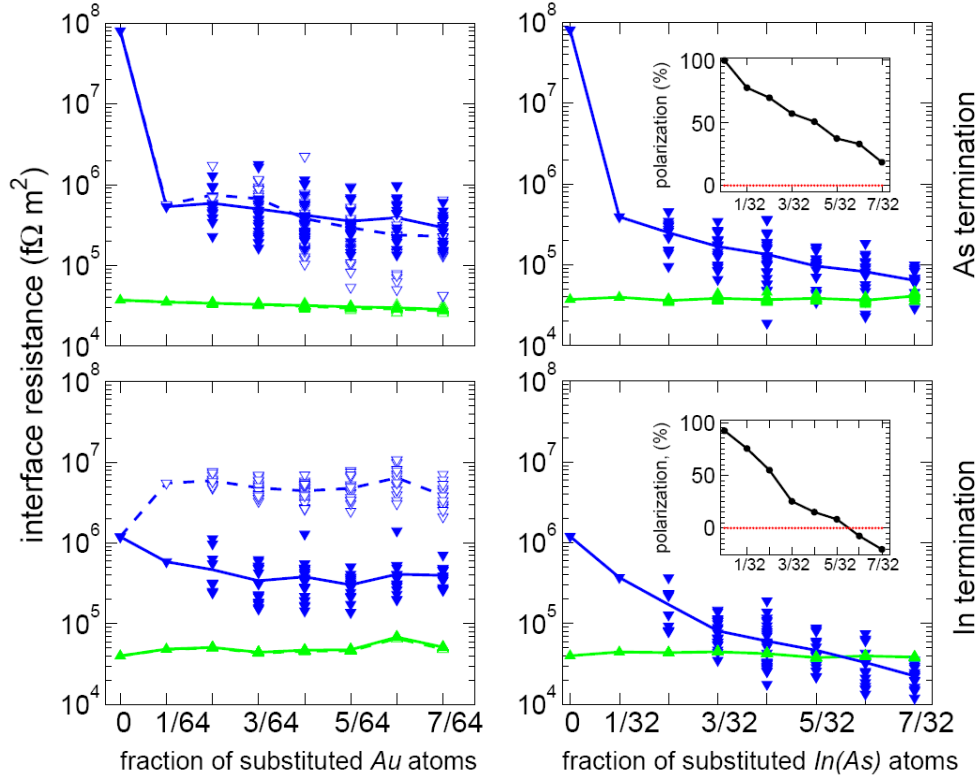


**Figure 2.9:** Majority- ( $\blacktriangle$ ,  $\triangle$ ) and minority- ( $\blacktriangledown$ ,  $\triangledown$ ) spin resistance of a Fe|Au|InAs junction for In- and As-terminated interface in case of Au|InAs interface disorder with In(As) substituting Au atoms. Filled and empty symbols denote the configurations where As (In) impurities occupy only one of the two inequivalent Au sites shown on the left top(bottom) panels. Majority ( $\blacktriangle$ ) and minority ( $\blacktriangledown$ ) spins resistance of Fe|Au|InAs junction for In- and As-terminated in case of Au|InAs interface disorder with Au substituting As(In) atoms shown on the right top(bottom) panels.

and the concentration of disorder is observed. Interface disorder results in quenching of the spin polarization of current injected from Fe into InAs. It has been possible to demonstrate that in the dilute limit of a single interface impurity, the interface transmission is very sensitive to the details of the interface atomic structure by applying a shift to the potential and/or position of the Fe impurity atom. This suggests trying to improve the spin-injection efficiency by preventing Fe from directly interacting with InAs by introducing a buffer layer which is reasonably lattice-matched to both Fe and InAs. A suitable candidate is Au which is unlikely to mix with Fe [30]. Au is a noble metal which at the Fermi level has only states with  $\Delta_1$  symmetry along the  $\Gamma - X$  direction. We showed that Au buffer layer increases the efficiency of spin

injection in an ideal Fe|Au|InAs system compared to an ideal Fe|InAs interface. A thin metal layer like Au can form quantum well states for energies and  $\mathbf{k}_{\parallel}$  vectors for which the transmission into Fe and InAs is poor. These states, however, play an important role only for clean interfaces and they are quenched by small amounts of interface disorder which destroy the translational symmetry and conservation of crystal momentum parallel to the interface.

The most important part of these work concerns the effect of interface disorder on the polarization of current injected into InAs in the Fe|Au|InAs junction. The effect was again studied using larger lateral supercells to model disorder. We found that disorder at the Fe|Au interface reduces the polarization but to a smaller degree than for Fe|InAs. Unfortunately, disorder on the non-magnetic Au|InAs interface is shown to have much stronger impact and can quench the polarization or change its sign.

## Bibliography

- [1] O. Wunnicke, P. Mavropoulos, R. Zeller, P. H. Dederichs, and D. Grundler, Phys. Rev. B **65**, 241306 (2002).
- [2] M. Zwierzycki, K. Xia, P. J. Kelly, G. E. W. Bauer, and I. Turek, Phys. Rev. B **67**, 092401 (2003).
- [3] G. Schmidt, D. Ferrand, L. W. Molenkamp, A. T. Filip, and B. J. van Wees, Phys. Rev. B **62**, R4790 (2000).
- [4] H. J. Zhu *et al.*, Phys. Rev. Lett. **87**, 016601 (2001).
- [5] A. T. Hanbicki, B. T. Jonker, G. Itskos, G. Kioseoglou, and A. Petrou, Appl. Phys. Lett. **80**, 1240 (2002).
- [6] A. T. Hanbicki *et al.*, Appl. Phys. Lett. **82**, 4092 (2003).
- [7] T. J. Zega, A. T. Hanbicki, S. C. Erwin, I. Zutic, and G. Kioseoglou, Phys. Rev. Lett. **96**, 196101 (2006).
- [8] A. Fert and H. Jaffres, Phys. Rev. B **64**, 184420 (2001).
- [9] X. Jiang *et al.*, Phys. Rev. Lett. **94**, 056601 (2005).
- [10] Y. B. Xu, E. T. M. Kernohan, M. Tselepi, J. A. C. Bland, and S. Holmes, Appl. Phys. Lett. **73**, 399 (1998).
- [11] L. Ruppel *et al.*, Phys. Rev. B **66**, 245307 (2002).
- [12] K. Xia, M. Zwierzycki, M. Talanana, P. J. Kelly, and G. E. W. Bauer, Phys. Rev. B **73**, 064420 (2006).



- 
- [13] O. K. Andersen, O. Jepsen, and D. Glötzel, Canonical description of the band structures of metals in, in *Highlights of Condensed Matter Theory*, edited by F. Bassani, F. Fumi, and M. P. Tosi, International School of Physics ‘Enrico Fermi’, Varenna, Italy, pp. 59–176, North-Holland, Amsterdam, 1985.
- [14] I. Turek, V. Drchal, J. Kudrnovský, M. Šob, and P. Weinberger, *Electronic Structure of Disordered Alloys, Surfaces and Interfaces* (Kluwer, Boston-London-Dordrecht, 1997).
- [15] O. K. Andersen, Phys. Rev. B **12**, 3060 (1975).
- [16] D. M. Ceperley and B. J. Alder, Phys. Rev. Lett. **45**, 566 (1980).
- [17] J. P. Perdew and A. Zunger, Phys. Rev. B **23**, 5048 (1981).
- [18] D. Glötzel, B. Segall, and O. K. Andersen, Sol. State Comm. **36**, 403 (1980).
- [19] R. M. Martin, *Electronic Structure: Basic Theory And Practical Methods* (Cambridge University Press, Cambridge, United Kingdom, 2004), pp. 42–44.
- [20] S. M. Sze, *Physics of Semiconductor Devices*, second ed. (John Wiley & Sons, New York, United States of America, 1981).
- [21] T. Ando, Phys. Rev. B **44**, 8017 (1991).
- [22] K. Xia *et al.*, Phys. Rev. B **63**, 064407 (2001).
- [23] Y. V. Sharvin, Zh. Eksp. Teor. Fiz. **48**, 984 (1965), [Sov. Phys. JETP **21**, 655 (1965)].
- [24] K. M. Schep, J. B. A. N. van Hoof, P. J. Kelly, G. E. W. Bauer, and J. E. Inglesfield, Phys. Rev. B **56**, 10805 (1997).
- [25] P. Soven, Phys. Rev. **156**, 809 (1967).
- [26] S. Mirbt, B. Sanyal, C. Isheden, and B. Johansson, Phys. Rev. B **67**, 155421 (2003).
- [27] S. C. Erwin, S.-H. Lee, and M. Scheffler, Phys. Rev. B **65**, 205422 (2002).
- [28] C. Ohler, C. Daniels, A. Förster, and H. Lüth, J. Vac. Sci. Technol. B **15**, 702 (1997).
- [29] M. Milun, P. Pervan, and D. P. Wooldruff, Rep. Prog. Phys. **65**, 99 (2002).
- [30] F. J. A. den Broeder, D. Kuiper, A. P. van de Mosselaer, and W. Hoving, Phys. Rev. Lett. **60**, 2769 (1988).



## Chapter 3

# Influence of Roughness and Disorder on Tunneling Magnetoresistance

*In this chapter we present a systematic, quantitative study of the effect of interface roughness and lead disorder on the transport properties of Fe|vacuum|Fe and FeCo|vacuum|FeCo MTJs. From parameter-free, electronic structure based calculations we find that surface roughness has very strong effect on the spin-polarized transport. The effect of lead disorder is weaker but still sufficient to suppress the huge TMR predicted for ideal systems.*

### 3.1 Introduction

Spintronics is a rapidly developing branch of a modern condensed matter physics. It aims at exploiting the quantum spin state of the electrons as well as their charge. Control over additional degree of freedom leads to observation of new effects. Most important for practical applications is the magnetoresistance - dependence of resistance of a system on external magnetic field. Here we concentrate on the tunneling magnetoresistance (TMR) which refers to the dependence of the resistance of a FM<sub>1</sub>|I|FM<sub>2</sub> (ferromagnet|insulator|ferromagnet) magnetic tunnel junction (MTJ) on the relative orientation of the magnetization directions of the ferromagnetic electrodes when these are changed from being antiparallel (AP) to parallel (P):  $TMR = (R_{AP} - R_P)/R_P \equiv (G_P - G_{AP})/G_{AP}$ . Since the discovery of large values of TMR in MTJs based upon ultrathin layers of amorphous Al<sub>2</sub>O<sub>3</sub> as insulator, [1] a considerable effort has been devoted to exploiting the effect in sensors and as the basis for non-volatile memory elements. Understanding TMR has been complicated by the difficulty of experimentally characterizing FM|I interfaces. The chemical composition of the interface has been shown [2] to have a strong influence on the magnitude and polarization of the TMR and knowledge of the interface structure is a neces-

sary preliminary to analyzing MTJs theoretically. In the absence of detailed structural models of the junctions and the materials-specific electronic structures which could be calculated with such models, the effect was interpreted in terms of electrode conduction-electron spin polarizations  $P_i$ , using a model suggested by Julliere [3] in which the  $\text{TMR} = 2P_1P_2/(1 - P_1P_2)$ . A great deal of discussion has focused on the factors contributing to the quantity [4]  $P$  but the use of amorphous oxide as barrier material made impossible a detailed theoretical study with which to confront experiment [5, 6].

The situation changed quite drastically with the recent observation of large values of TMR at room temperature in FeCo|MgO|FeCo MTJs in which the MgO tunnel barrier was mono- [7, 8] or poly-crystalline [9]. This work was motivated in part by the prediction [10, 11] by materials-specific transport calculations of huge TMR values for ideal Fe|MgO|Fe structures. This new development lends fresh urgency to the need to understand the factors governing the sign and magnitude of TMR because the largest observed value of 353% at low temperature, [8] is still well below the ab-initio predicted values of order 10,000% for the relevant thicknesses of MgO [10]. Some effort has been devoted to explaining the discrepancy in terms of interface relaxation [12] or the formation of a layer of FeO at the interface [13, 14] but the role of interface disorder has only been speculated upon.

In this chapter, which is a follow-up to our earlier study, [15] we use first principles electronic structure calculations to study the effect of roughness and lead disorder on TMR in MTJs with a vacuum barrier and Fe or  $\text{Fe}_{1-x}\text{Co}_x$  alloy electrodes. A vacuum barrier was chosen due to its simplicity and because there are many studies of spin-dependent vacuum tunneling in its own right [16–20].

The chapter is organized as follows: in the next section we discuss theoretical approach used to obtain results presented in remaining sections. In Sec. 3.3 we briefly discuss the electronic structure of the ideal MTJ concentrating on the potential profile of VTB. Sec. 3.4 is devoted to the detailed study of the transport properties of ideal Fe|vacuum|Fe junction. In the next two sections we discuss the results obtained for MTJ with disorder in the form of surface roughness (Sec. 3.5) and substitutional disorder in the leads (Sec. 3.6). We finish with the conclusions in the last section. Technical details concerning the convergence of our calculations are relegated to the two appendices.

## 3.2 Methods, Models and Technical Details

We study transport properties of the MTJs in the linear-response regime within the framework of the local spin-density approximation (LSDA) of the density functional theory (DFT) in a two-step procedure. In the first step self-consistent potentials, charge- and spin-densities are determined for a system (Fig. 3.1) consisting of two semi-infinite ideal leads and the scattering region (SR). The scattering is restricted to the latter part of the system which encompasses vacuum tunneling barrier (VTB)

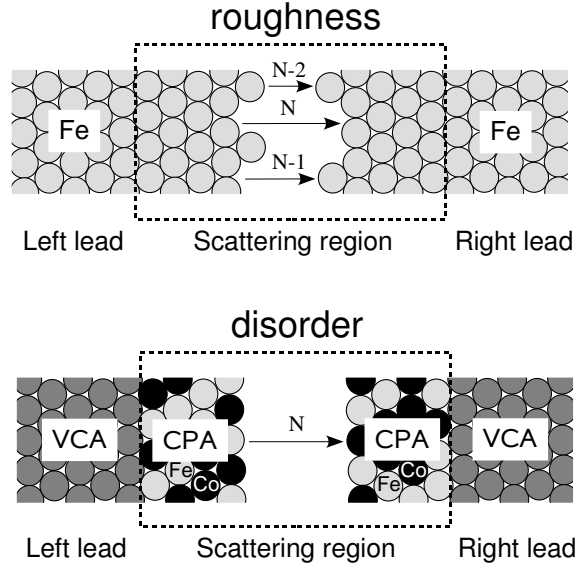


**Figure 3.1:** Top figure represents Fe|vacuum|Fe MTJ with interface roughness (surface coverage). Grey circles stand for Fe atoms. SR in this figure is given by vacuum barrier and 4MLs of Fe on each side of it. Interface roughness is modelled as an incomplete Fe layers. Bottom figure represents alloy lead disorder in FeCo|vacuum|FeCo MTJ. Grey and black circles in the SR stand for Fe and Co atoms respectively. In this case FeCo atoms in the leads are treated in the virtual crystal approximation (VCA). These atoms are represented with brown circles.

and several monolayers (MLs) of metal immediately next to it. The assumed in-plane translational invariance preserves  $k_{\parallel}$  as good quantum number. The self consistent calculations are performed using surface Green's function [21] implementation of the tight-binding linear muffin-tin orbitals (TB-LMTO) method [22]. Throughout the paper we use *spd* basis set and exchange-correlation potential is parameterized according to von Barth and Hedin [23]. During the calculations the potentials in the scattering region are allowed to relax. The potentials of the leads are kept at their previously calculated bulk values. Atomic spheres approximation (ASA) is used with the sites of the fixed *bcc* lattice occupied with either atomic or empty spheres (ES), the latter used to model VTB. In the case of Fe only MTJs (Fig. 3.1, top panel) an experimental lattice constant  $a_{\text{Fe}} = 2.866\text{\AA}$  is used. (001) is the transport direction.

In the second step, the self-consistent potentials are used to calculate the elements of the scattering matrix (transmission and reflection coefficients) using a TB-MTO implementation [24] of wave-function matching (WFM) scheme due to Ando [25]. With these the conductance can be calculated using Landauer-Büttiker formula [26]. This involves integration over two-dimensional Brillouin zone (2D BZ). Convergence

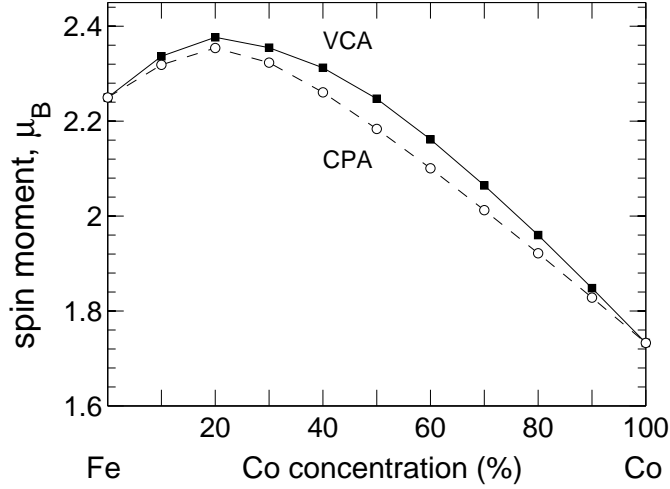


**Figure 3.2:** Bulk magnetic moments of FeCo *bcc* alloy as the function of alloy concentration calculated in the VCA (solid line) and CPA (dashed line) approximations.

of the results with respect to sampling density is discussed in Appendix 3.8.

The disorder is modelled using lateral supercells with typical size of 100 atoms (10x10). The convergence with respect to supercell size is discussed in Appendix 3.9. Two different kinds of disorder, shown in panels of Fig. 3.1, are considered.

The first one is the roughness at Fe|vacuum interface (Fig. 3.1, top panel). In this case the topmost layers of either electrode is covered with additional Fe atoms, occupying the sites of underlying *bcc* lattice. The potentials inside atomic and empty spheres are calculated using the layered version [21] of a coherent potential approximation (CPA) [27] with the surface layer treated formally as substitutional  $\text{Fe}_x\text{ES}_{1-x}$  alloy. The spheres are then randomly distributed in the lateral supercell with the concentration of Fe corresponding to the assumed surface coverage  $x$ .

The second case studied is the junction with electrodes composed of the random  $\text{Fe}_{1-x}\text{Co}_x$  alloy (Fig. 3.1, bottom panel). It is known from the experiments that Co forms a substitutional random alloy with Fe ( $\text{Fe}_{1-x}\text{Co}_x$ ) which assumes *bcc* structure in the concentration range from  $x = 0.0$  to  $x \simeq 0.7$  [28]. For higher Co concentrations a phase transition to the *hcp* structure occurs. For the sake of simplicity we assume here a *bcc* crystal structure for all concentrations. The  $\text{Fe}_x\text{Co}_{1-x}$  alloy lattice constant is calculated from Vegard's law whereby

$$a_{\text{Fe}_x\text{Co}_{1-x}} = xa_{\text{Fe}} + (1-x)a_{\text{Co}} \quad (3.1)$$

Here  $a_{\text{Co}} = 2.817\text{\AA}$  [29] is a lattice constant of *bcc* Co determined assuming that the volumes of *bcc* and *hcp* cells are identical. Like previously the atomic potentials

inside SR are calculated using CPA and the atomic spheres distributed randomly in lateral supercells. Note that we do not introduce additional roughness at the FM|vacuum interface. Using this approach it is possible to model substitutional disorder in the part of the electrodes falling inside the scattering region. However, doing the same for the leads would require the use of supercells also in the transport direction as the WFM scheme is based on the assumption that the leads possess the full translational symmetry. It would considerably increase the computational costs and is in practice not feasible. Instead we describe the leads using virtual crystal approximation (VCA) where the alloy is replaced by homogeneous material consisting of "atoms" with fractional atomic numbers calculated using equation akin to Eq. (3.1). Given their closeness in the periodic table and similarity of their *bcc* lattice constants one expects VCA to work reasonably for the alloy consisting of Fe and Co. We test it explicitly by comparing the magnetic moments of the bulk  $\text{Fe}_x\text{Co}_{1-x}$  alloy calculated using VCA and CPA. An excellent agreement is found between VCA and CPA values for the whole range of concentrations as shown in Fig. 3.2. Furthermore the values agree well with other experimental and theoretical results [30]. Note that only spin magnetic moment is calculated with the orbital contribution being neglected. Treating the scattering region and leads differently means that the fictitious interface is introduced at the boundaries between these parts of the system (Fig. 3.1, bottom panel). However its presence is of no practical consequence as the resistance of the whole structure is strongly dominated by the tunneling barrier. This point is further discussed in Appendix 3.9.

All conductances in the paper are given in  $e^2/h$  units and normalized to the area of the in-plane 2D unit cell, equal to  $a_{\text{Fe}_x\text{Co}_{1-x}}^2$ .

### 3.3 Barrier profile

The usual point of reference when discussing TMR is the textbook problem of free electron tunneling through a rectangular potential barrier. Before proceeding it is useful to establish to what extent our VTB conforms to this simple model.

In order to determine the potential profile of VTB we start with the self consistent calculations for ideal Fe|vacuum|Fe junction. Then for each "layer" of vacuum we use corresponding ES to populate the sites of bulk *bcc* structure and perform band-structure calculations. The position of the bottom of resulting parabolic band with respect to the Fermi energy of the system is taken to be the barrier height for a given layer. The results of this procedure are shown in Fig. 3.3 for two different thicknesses of VTB. It can be seen that for a sufficiently thick barrier (20 MLs equals  $28\text{\AA}$ ) the shape is indeed approximately rectangular. The work function extracted from the 20 MLs plot equals to 4.75 eV which agrees reasonably with the experimental value of 4.5 eV [31]. We note that for MTJs with barrier thickness exceeding 10 MLs the calculated conductances are smaller than the numerical accuracy [32]. Because of that in the following we shall restrict our calculations to barriers of 10 MLs or less. An example of the potential profile for thinner (8 MLs) VTB is shown in the inset of Fig. 3.3

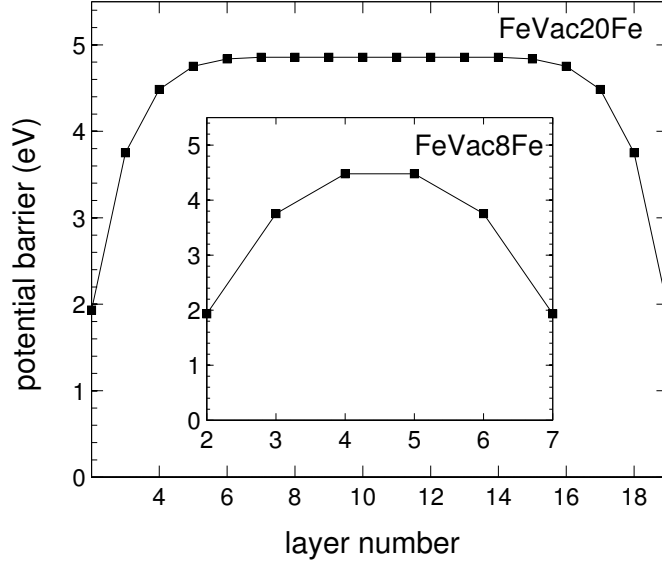


**Figure 3.3:** Potential profile of vacuum barrier for Fe|vacuum|Fe MTJs with barrier width of 20 MLs with respect to Fermi energy. Inset: profile of the potential profile for the barrier of 8 MLs.

### 3.4 Ideal Fe|vacuum|Fe MTJ. Transport calculations

Before embarking on a study of roughness and disorder effects on the TMR it is important to understand what factors determine the transport properties of an ideal MTJ. We start by calculating conductance of ideal Fe|vacuum|Fe system with VTB of increasing thickness. The results for majority and minority spin channels in parallel configuration of the magnetic moments,  $G_P^{maj}$  and  $G_P^{min}$ , are shown in Fig. 3.4 together with a single spin conductance for antiparallel configuration,  $G_{AP}^\sigma$ . It is instructive to compare these results with the predictions of a simple model of free electrons tunneling through a rectangular barrier. In this model the decay of the conductance is asymptotically described by a simple exponential factor  $exp(-2d\kappa)$  where  $d$  is the thickness of the barrier and  $\kappa = \sqrt{(2m/\hbar^2)V_b}$  with  $V_b$  being the height of the barrier.

All three curves in Fig. 3.4 reach exponential limit for VTB thicker than 8 MLs with the same decay rate (*i.e.* the slope of the curve). Extracting the barrier height from the slopes of the curves yields  $V_b \approx 4.7$  eV in good agreement with the value extracted from the potential profile of Fig. 3.3.



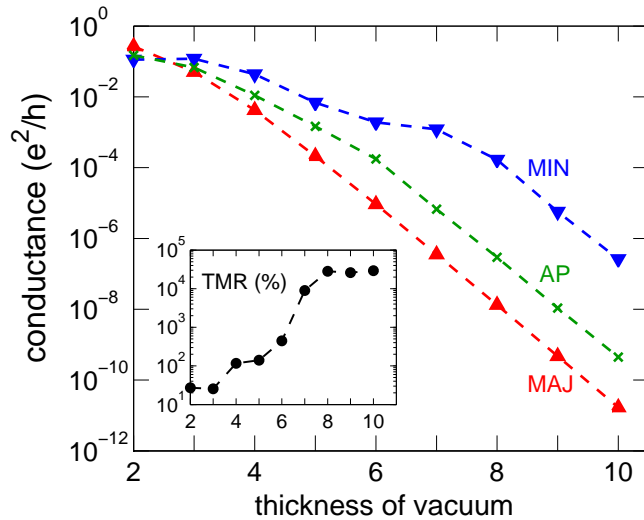


**Figure 3.4:** Conductances  $G_P^{min}$  ( $\blacktriangledown$ ),  $G_P^{maj}$  ( $\blacktriangle$ ), and  $G_{AP}^\sigma$  ( $\times$ ) of an ideal Fe|vacuum|Fe MTJ as a function of the barrier thickness (measured in units of layers of a bcc lattice). The corresponding values of TMR are shown in the inset.

The TMR, shown in the inset of Fig. 3.4, increases with the thickness of VTB and eventually saturates at about 20,000%. This number is comparable to the TMR those calculated from the first-principles for ideal Fe|MgO|Fe MTJ [10, 11].

Even though all three curves reach the same asymptotic limit of exponential attenuation, their behavior is very different for thinner barriers. This is the consequence of different underlying mechanisms of transmission. We will discuss these in the following subsections concentrating on majority and minority channel in parallel configuration.

### 3.4.1 Parallel configuration: Majority channel

Majority conductance for parallel configuration exhibit the simplest behavior of the three shown in Fig. 3.4. For all but the thinnest barriers the curve follows a simple exponential decay. Accordingly we expect the tunneling to qualitatively follow the predictions of the free electron model. This is confirmed by examination of the  $\mathbf{k}_\parallel$ -resolved transmission shown in the right hand panel of Fig. 3.5. The transmission has a maximum in the center of 2D BZ ( $\bar{\Gamma}$  point) and decays rapidly once we move away from the center. As the thickness of VTB increases the maximum value decreases exponentially and the transmission becomes increasingly more concentrated around  $\bar{\Gamma}$  in accordance with free electron model.

Nearly spherical symmetry of the transmission plot might seem surprising when compared with the projection of the majority Fermi surface (FSP) shown in the left

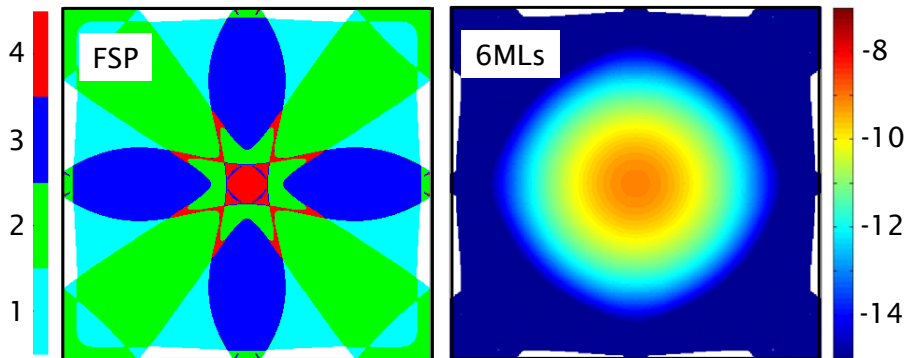


**Figure 3.5:** Fe majority Fermi surface projection (FSP) on plane perpendicular to [001] direction (on the left) and  $k_{\parallel}$  resolved majority transmission for VTB of 6 MLs shown on a logarithmic scale (right panel). The results are shown in full first 2D BZ.

hand panel of Fig. 3.5. The latter is multiply sheeted and far from free electron sphere. This apparent contradiction can be resolved by noting that the transmission is dominated by the contribution from a single sheet of the Fe's FS which possesses relatively simple geometry and is visible as a rectangular cyan shape in the background of the FSP plot. Thanks to their high symmetry,  $\Delta_1$  at  $\bar{\Gamma}$ , and mostly  $sp$  orbital character these states are able to couple most effectively to the simple decaying modes in the vacuum layer.

### 3.4.2 Parallel configuration: Minority channel

The dependence of minority conductance on VTB thickness (Fig. 3.4) is quite different from that seen for majority spins. For thicknesses greater than 3 MLs the minority channel dominates the conductance giving rise to large and negative polarization [33] of the current in the parallel configuration. The differences are even more apparent for  $k_{\parallel}$ -resolved transmission shown in Fig. 3.6 for varying thickness of VTB. The symmetry of the plots clearly deviates from spherical symmetry of tunneling in the majority channel. The most important feature however is that for all but thinnest barriers the transmission comes predominantly from the small areas of very high (comparable or equal to unity) transmission. One set of such "hot spots" or resonances is located immediately next to the  $\bar{\Gamma}$  point. In the following we will be referring to these as A type resonances. Another set of very narrowly defined resonances is located further away from the center of the 2D BZ. The position of these B type resonances is marked with arrows in Fig. 3.6. The dominance of "hot spots" is more apparent when a linear scale is used. An example is shown in Fig. 3.7

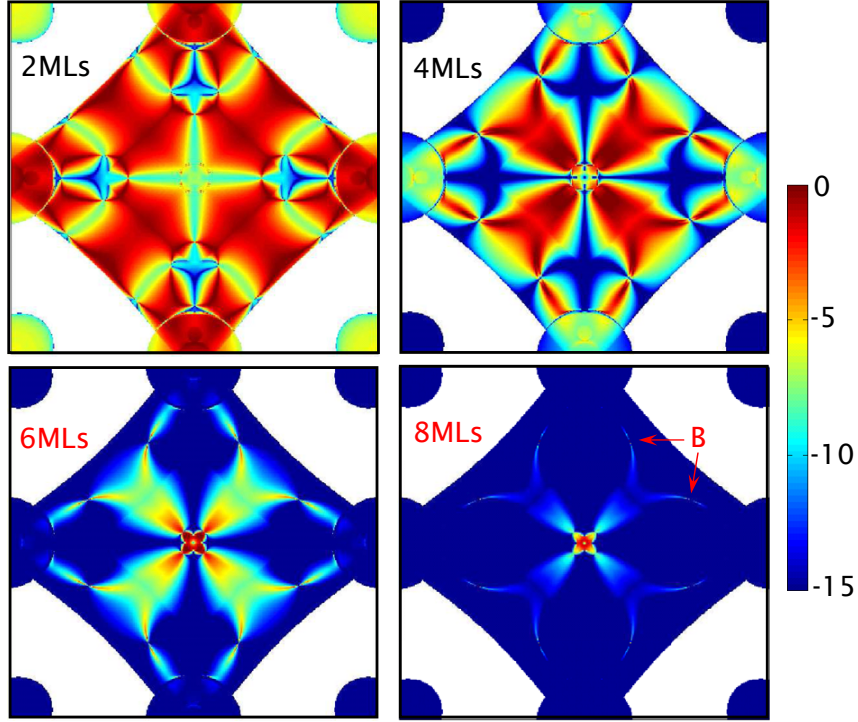


**Figure 3.6:** The  $k_{\parallel}$  resolved minority transmission for VTB of 2, 4, 6 and 8 MLs shown on a logarithmic scale. For the latter the positions of B resonance are shown with arrows. The results are shown in full first 2D BZ.

for VTB of 8 MLs.

Resonant peaks in  $k_{\parallel}$  transmission has been found in first principles calculations of tunneling through both vacuum [34–36] and other barriers [10–12]. The resonances arise when there exists a surface state on the surfaces of metallic electrodes. Such state can indeed be found for Fe(001) surface [16]. Its existence is made possible by the so called “symmetry gap” present in Fe’s band structure. Along  $\Gamma - H$  direction in 3D BZ, corresponding to  $\bar{\Gamma}$  point in 2D BZ, the two  $\Delta_1$  bands are separated by a gap of about 3 to 4 eV depending on the spin orientation. The other bands present in this range of energies possess distinctly different symmetries. Consequently a surface state of  $\Delta_1$  symmetry can exist at  $\bar{\Gamma}$  point provided that its energy falls within the gap. The surface states exist for both majority and minority spins. They are however positioned very differently with respect to the Fermi level which reflects the differences in the positions of  $\Delta_1$  symmetry gaps in the bulk band structures. The majority channel surface state is located about 2 eV beneath the Fermi level and

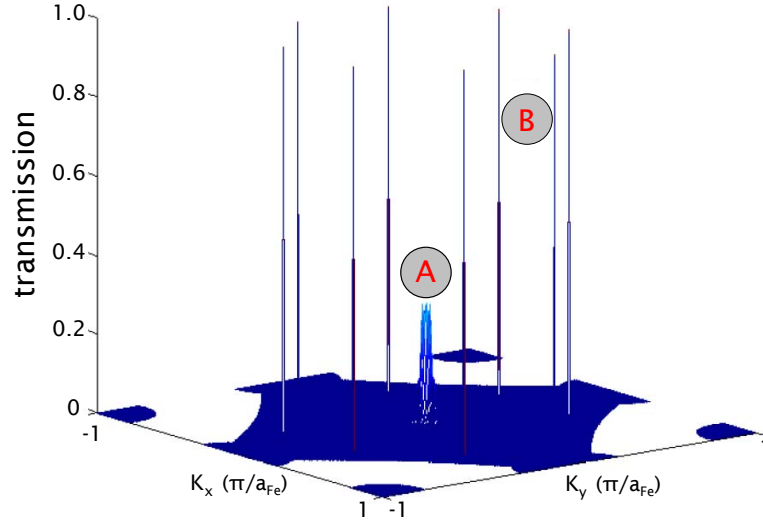


**Figure 3.7:** The  $\mathbf{k}_{\parallel}$  resolved transmission for Fe|vacuum|Fe MTJ with barrier width of 8 MLs shown using linear scale. A and B labels stand for two resonances close to  $\bar{\Gamma}$  and far from the center of the 2D BZ correspondingly.

consequently does not influence transmission. The minority surface state on the other hand is located close to the Fermi level and it is closely associated with the “hot spots” visible in Figs. 3.6 and 3.7.

The existence of surface state can be demonstrated by explicit calculation of density of states (DOS). However it is difficult to distinguish its features in the plots of the full or even layer-resolved DOS (LDOS). Instead we calculate for minority channel  $\mathbf{k}_{\parallel}$ , layer- and orbital-resolved DOS. Setting  $\mathbf{k}_{\parallel} = (0, 0)$  and summing over the orbitals compatible with  $\Delta_1$  symmetry ( $s, p_z$  and  $d_{3z^2-r^2}$ ) we then obtain, for the surface layer, the results shown in Fig. 3.8 [37]. There are no  $\Delta_1$  states in the minority band structure of the bulk Fe for the energy range shown in the figure. Indeed the same procedure repeated for the layers away from the interface shows that the peaks visible in Fig. 3.8 vanish over the distance of few monolayers from the Fe|vacuum interface (see Ref. [38] for details). The surface state consists predominantly of  $d_{3z^2-r^2}$  orbitals extending into the vacuum. For VTB of limited thickness the states at both Fe surfaces can interact through the vacuum forming bonding-antibonding pairs. This leads to the splitting of the peak visible clearly in Fig. 3.8 for 5 MLs curve. As the thickness of VTB increases the splitting becomes weaker and the two peaks merge into one as seen for 8 MLs curve in the plot.

The surface state located exactly at  $\bar{\Gamma}$  is orthogonal to states in the bulk and thus does not contribute to the coherent tunneling studied in this paper. However, as we move away from the center of 2D BZ the surface state evolves into resonant states of

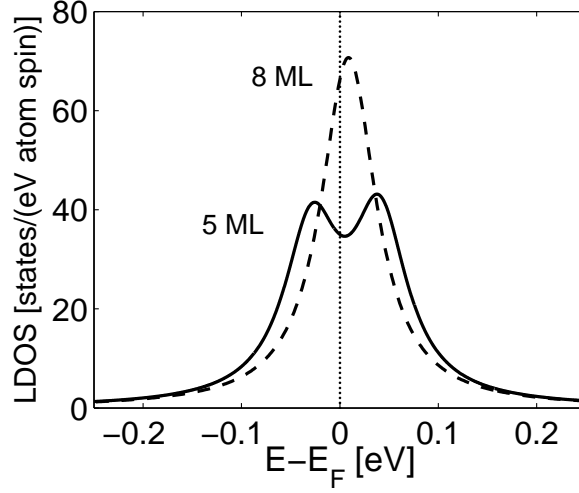


**Figure 3.8:**  $\Delta_1$  contribution to the minority LDOS of the interfacial Fe atom for  $\mathbf{k}_{\parallel} = \bar{\Gamma}$  in the Fe|vacuum|Fe MTJ for 5 MLs (solid line) and 8 MLs (dashed line) vacuum.

lower symmetry capable of coupling to the states in the bulk. These states possess weak but non-negligible in-plane dispersion (*i.e.*  $\mathbf{k}_{\parallel}$  dependence). Just as the surface state the resonant states can interact through the barrier forming bonding-antibonding pairs. Whenever either of the pair aligns with the Fermi level a resonant tunneling can take place. There are two parameters that characterize the resonant tunneling: the surface resonance half-width  $\Gamma_R$  and bonding-antibonding splitting  $\Delta$  or equivalently the resonance life time  $t_R = \hbar/\Gamma_R$  and hopping time  $t_H = \hbar\pi/\Delta$ . The resonant transmission without attenuation ( $T = 1$ ) is observed if  $\Delta \geq \Gamma_R$  [34].

In order to map out the positions of resonant states in 2D BZ we have plotted the minority  $\mathbf{k}_{\parallel}$ -resolved LDOS for atomic layer at the interface and in the bulk of Fe. These are shown in Fig. 3.9 for VTB of 8 MLs together with the projected Fermi surface. The energy has been fixed at the Fermi level. The interfacial LDOS is vividly different from that of the bulk layer with characteristic sharply peaked structures. The amplitudes of the peaks drop rapidly as we move away from Fe|vacuum interface. What is more the presence of the peaks coincide with the “hot spots” of tunneling transmission shown in Fig. 3.6.

With the increasing thickness of the barrier the bonding-antibonding splitting decreases and as a result the position of the resonances in the 2D BZ changes as well. However, as long as the splitting is large enough for the resonance condition to be

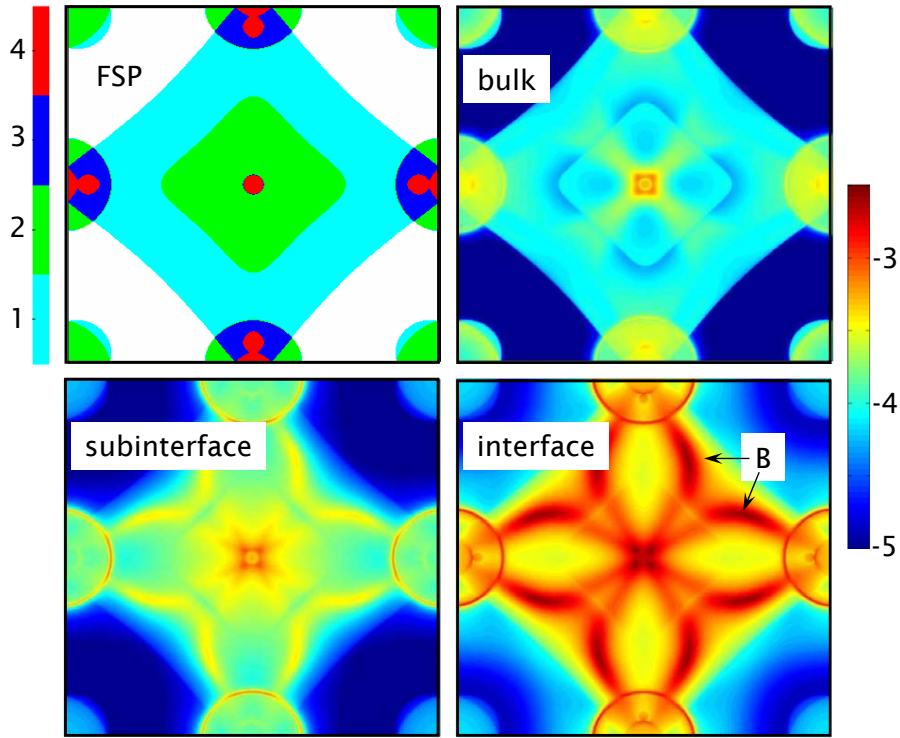


**Figure 3.9:** Minority spin FSP on the plane perpendicular to  $[001]$  direction (top left). The LDOS (logarithmic scale) as a function of the  $k_{\parallel}$  for Fe atom in bulk (top right) at the subinterface (bottom left) and interface (bottom right). The LDOS calculations were performed for energy equal to the Fermi level. The positions of B resonance are shown with arrows in the right-bottom panel.

fulfilled, the maximum transmission remains equal to one. This is illustrated in Fig. 3.10 where the maxima of  $k_{\parallel}$ -resolved transmission for A and B resonances are shown separately. The maximum transmission for majority channel and for a single spin transmission in AP configuration are shown as well for comparison. We see that the maximum for A type resonances start decreasing only for VTBs thicker than 7 MLs. This coincides with the onset of the exponential decay for the total minority channel conductance shown in Fig. 3.4. The correlation might seem surprising given that the maximum for B type resonances remains equal to one for even thicker barriers. However, in practice the contribution to the total conductance comes entirely from A type resonances. The reason for this is that B type peaks are extremely localized in the momentum space. This is illustrated in Fig. 3.11 where we plot a cross-section through the A and B type peaks in transmission. We see that the widths of the peaks differ by as much as three orders of magnitude. Thus the regions of high

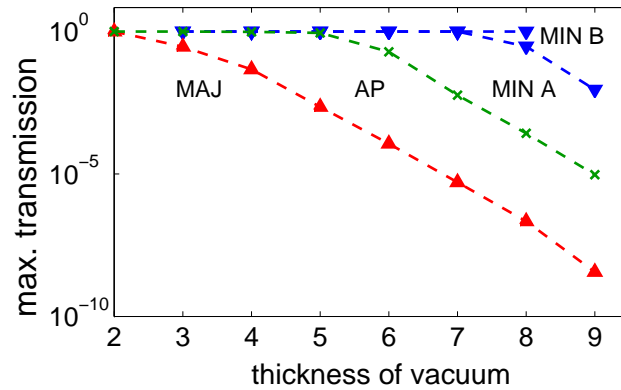


**Figure 3.10:** Maximum transmissions for majority ( $\blacktriangle$ ) and minority ( $\blacktriangledown$ ) spin channels and one spin channel in antiparallel configuration ( $\times$ ) are shown as a function of barrier width.

transmission associated with B type resonances form effectively a set of measure zero and do not contribute to the integral over 2D BZ.

In the AP configuration surface state appears in minority spin channel on only one of Fe|vacuum interfaces. However, as seen in Fig. 3.10, for sufficiently thin barrier even a single resonant state can give rise to significant transmission. Just as for parallel configuration there exists a rough correspondence between the features of the curves in Figs. 3.10 and 3.4.

### 3.5 Effect of interfacial roughness on the TMR

An ideal tunnel junction considered in the previous section is impossible to realize in practice; there will always be some finite amount of disorder in the form of surface roughness, islands, dislocations etc. In this section we will consider Fe|vacuum|Fe junction with disorder introduced in the form of incomplete (rough) surface layers, modeled by occupying, at random, a fraction of the lattice sites of the topmost layer with Fe atoms. A sketch of the system is shown in the top panel of Fig. 3.1. Three different mechanisms can influence the transmission through the MTJ with rough Fe surfaces. Firstly, introduction of the disorder breaks the point group symmetry of the system and is bound to destroy the surface state together with the associated resonant states. This in turn should result in the huge decrease of minority conductance as the resonant tunneling is mostly responsible for the high values seen for ideal structures. Secondly, in case of the weak disorder the surface state might possibly survive but it can be shifted with respect to the Fermi level and the associated resonances broadened. That latter effect might in some cases lead to an increase of the

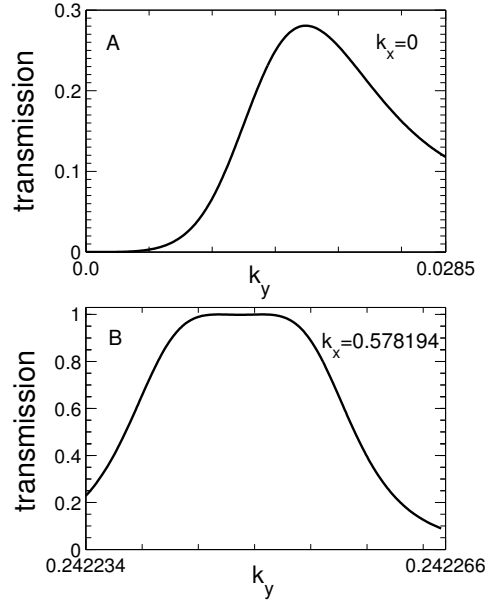


**Figure 3.11:** Profiles of peaks in minority transmission probability of A (top) and B (bottom) resonances for VTB of 8 MLs.

conductance depending on the details like the original energy of the resonant state and the amplitude of bonding-antibonding splitting. Thirdly, introducing random coverage implies that in some areas the local thickness of VTB will be smaller than for original ideal junction. In view of steep exponential dependence of tunneling on thickness (Fig. 3.4) this can lead to increase of conductances. This effect is likely to influence the majority channel with its simple free-electron like tunneling. These broad predictions are supported by results of calculations for 50% surface coverage shown in Fig. 3.12.  $10 \times 10$  lateral supercells were used and the results were averaged over 20 configurations of disorder. The disorder was generated by randomly extracting half of Fe atoms from one of Fe surfaces and depositing them (also randomly) on the other surface thus keeping the average VTB thickness unchanged. As expected the minority channel exhibits the most spectacular changes in comparison to the conductances of ideal system also shown in Fig. 3.12 for comparison. The values of the minority conductances decrease by up to four orders in magnitude and are now actually smaller than the majority ones. The conductance of majority channel is moderately increased and the antiparallel case falls in between the two parallel conductances. The values of TMR (see the inset in Fig. 3.12) are greatly reduced and are now in the range of 10 to 100% in qualitative agreement with experiments [7–9].

All three conductances for disordered system shown in Fig. 3.12 decay exponen-



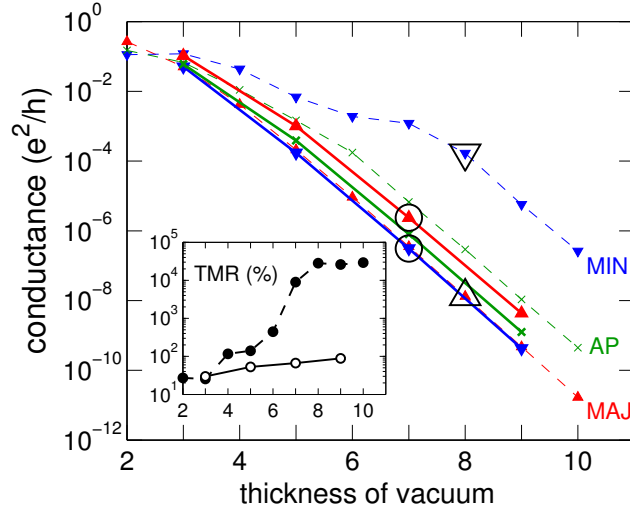


**Figure 3.12:** Conductances  $G_P^{min}$  ( $\blacktriangledown$ ),  $G_P^{maj}$  ( $\blacktriangle$ ), and  $G_{AP}^\sigma$  ( $\times$ ) of an Fe|vacuum|Fe MTJ as a function of the barrier thickness (measured in units of layers of a *bcc* lattice). The dashed lines are for ideal junctions. The solid lines are configuration-averaged conductances for rough junctions prepared by removing, at random, half of the Fe atoms from one surface and depositing them, at random, on the other surface. The results are normalized to the  $1 \times 1$  surface unit cell used for the ideal case. The large symbols refer to data points which also appear in Fig. 3.4.

tially with the thickness of the barrier already for very thin barriers. This, together with the huge drop of minority conductance, suggests that disorder in the form of 50% coverage is sufficient to kill the surface resonant effects in the transmission.

In order to better understand the effect of the disorder it is useful to follow the evolution of the conductance with the increasing surface coverage. This is shown in Fig. 3.13 together with the TMR in the inset. The VTB thickness has been fixed to 8 MLs and the roughness is created by depositing additional Fe atoms on surfaces of both electrodes. This means that 50% point in Fig. 3.13 corresponds to 7MLs in Fig. 3.12. Equivalent points in both figures have been marked with large symbols. As we can see there are qualitative differences in the dependence of the conductances on surface coverage. In the following subsections we will discuss these in more details.

### 3.5.1 Majority transmission

Majority channel for parallel configuration exhibits the most trivial behavior of the three conductances shown in Fig. 3.13. Conductance increases as the function of

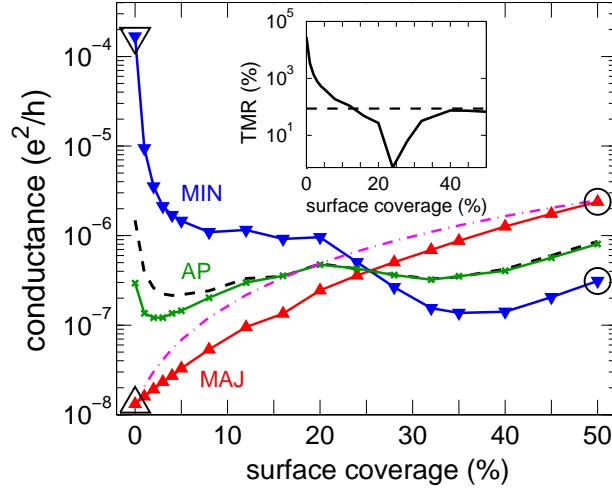


**Figure 3.13:** Configuration-averaged conductances  $G_P^{min}$  ( $\blacktriangledown$ ),  $G_P^{maj}$  ( $\blacktriangle$ ), and  $G_{AP}^\sigma$  ( $\times$ ) of an Fe|vacuum|Fe MTJ with 8 MLs barrier width as a function of the surface coverage, normalized to a  $1 \times 1$  surface unit cell. The dashed line denotes  $G_{AP}^\sigma$  predicted from (3.2) and the dash-dotted line gives the majority conductance calculated using Eq. (3.2). Inset: TMR as a function of the surface coverage. The dashed line is the value predicted using Julliere's expression and a calculated DOS polarization of 55%. Large symbols refer to the similarly marked data points in the previous figure.

surface coverage due to reduction of an effective barrier thickness. A simple 'weak-link' model can be used to approximate these results. According to this model a transmission depends locally only on the thickness of the barrier. Conductance of the rough MTJ with 8 MLs barrier is then described as weighted average over the conductances of ideal systems with VTB of 6,7 and 8 MLs:

$$G_P^{maj}(x) = P_6(x)G_6^{maj} + P_7(x)G_7^{maj} + P_8(x)G_8^{maj} \quad (3.2)$$

where  $G_P^{maj}(n)$  is the majority conductance of ideal junction with VTB of  $n$  MLs and the weights are defined as:  $P_6(x) = x^2$ ,  $P_7(x) = 2x(1-x)$  and  $P_8(x) = (1-x)^2$ . The results calculated using Eq. (3.2) are shown as dash-dot line in Fig. 3.13. The values predicted for intermediate coverages differ from the results of first principles calculations. However the overall trend and the values at extreme points of the plot are well reproduced.

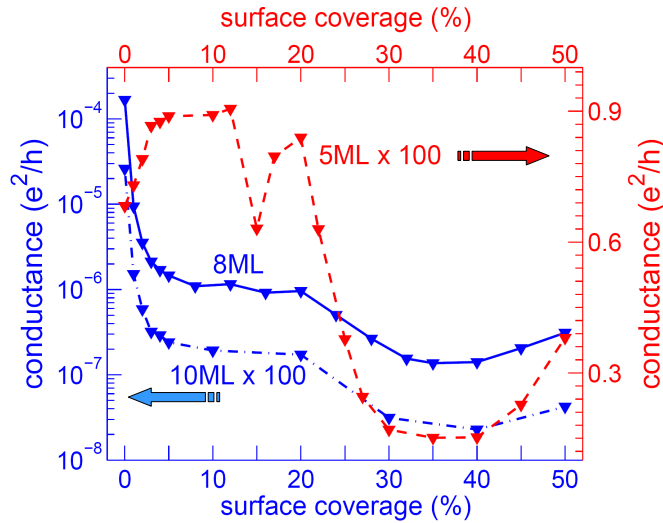


**Figure 3.14:** Minority conductance as a function of surface coverage in case of 5, 8 and 10 MLs VTBs. Note that results for 5 and 10 MLs are multiplied by 100. Results for 5 MLs are shown using the linear scale on the right hand side of the plot.

### 3.5.2 Minority transmission

The minority conductance exhibits fairly complex dependence on the amount of surface coverage. For coverages of up to 5% we see a rapid decrease followed by a plateau of approximately constant (on logarithmic scale) values extending to about 20% of coverage. For even larger coverages the conductance value decreases again, reaches a minimum around 35% and afterwards start to increase. In the last part the minority and majority curves are practically parallel. This suggests that the same mechanism, namely the decrease of the average thickness of the barrier, is responsible for the observed growth. Similarity to the majority channel indicates also that the resonant effects, dominating transmission through an ideal system, have been entirely destroyed at this point.

A huge decrease of conductance is visible already for coverages as small as 1%. It is unlikely that surface state and associated resonances are destroyed by disorder so weak. Instead, a second mechanism discussed in the beginning of this section might be a culprit. Changes to a local electronic structure, in particular broadening of the resonances, can either decrease or increase the transmission depending on the details like the position of the peak with respect to the Fermi energy and the strength of bonding-antibonding splitting. Both possibilities are demonstrated in Fig. 3.14 where we have plotted the minority conductance calculated for VTB of 5, 8, and 10 MLs. The behavior of 8 and 10 MLs curves is qualitatively very similar, although the values

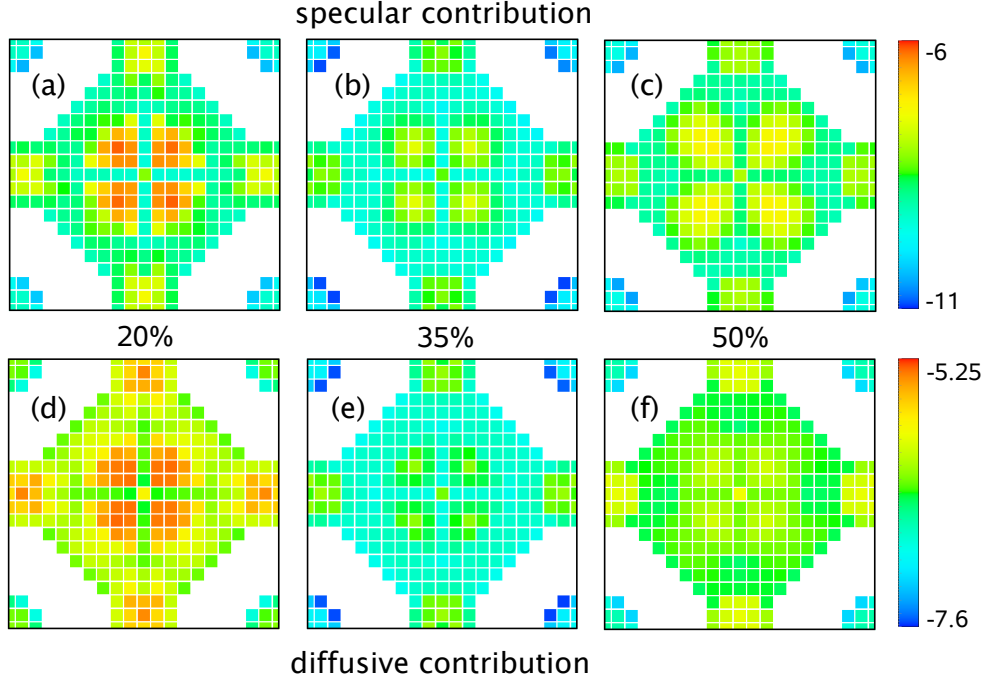


**Figure 3.15:** Specular (top panels) and diffusive (bottom panels) contributions of transmission calculated for 20% (a,d), 35% (b,e) and 50% (c,f) of surface coverage (logarithmic scales). Calculations are performed in 20x20 SC. The single  $\mathbf{k}_{\parallel}$ -point in supercell 2D BZ was chosen to be close to the  $\bar{\Gamma}$  point. The results are averaged over 40 disordered configurations.

of course differ very substantially. For 5 MLs however the introduction of weak disorder results in a modest increase of the conductance. Note that 5 MLs results are shown using linear scale given on the right hand side of the plot.

The fact that minority conductance, while substantially reduced, remains far larger than the majority one for coverages of up to 20% suggests that transmission in this region of the curve is still assisted by the resonant states on Fe surface. A possible scenario is that the random disorder removes the mirror symmetry of the junction and effectively “detunes” resonant states. In this situation the perfect resonant tunneling without attenuation is no longer possible. However even the single resonant state can contribute significantly to the transmission as we have seen in Sec. 3.4 for AP configuration.

The conductance of MTJ in the presence of the disorder can be factorized into

the specular and diffusive contribution:

$$G = G^{spec} + G^{diff} = \frac{e^2}{h} \sum_{\mathbf{k}_{\parallel}} T(\mathbf{k}_{\parallel}, \mathbf{k}_{\parallel}) + \frac{e^2}{h} \sum_{\mathbf{k}_{\parallel} \neq \mathbf{k}'_{\parallel}} T(\mathbf{k}_{\parallel}, \mathbf{k}'_{\parallel}) \quad (3.3)$$

where each of the transmissions is summed over the incoming and outgoing states  $T(\mathbf{k}_{\parallel}, \mathbf{k}'_{\parallel}) = \sum_{\mu\nu} |t_{\mu\nu}(\mathbf{k}_{\parallel}, \mathbf{k}'_{\parallel})|^2$ . As the disorder present in the system increases the diffusive term in Eq. (3.3) start playing increasingly more important role. Using a channel decomposition technique (see Ref. [24] for details) we can separate the two terms. In Fig. 3.15 we show the  $\mathbf{k}_{\parallel}$ -resolved specular [ $T^{spec}(\mathbf{k}_{\parallel}) = T(\mathbf{k}_{\parallel}, \mathbf{k}_{\parallel})$ ] and diffusive [ $T^{diff}(\mathbf{k}_{\parallel}) = \sum_{\mathbf{k}'_{\parallel} (\neq \mathbf{k}_{\parallel})} T(\mathbf{k}_{\parallel}, \mathbf{k}'_{\parallel})$ ] transmissions for varying coverages. The calculations were performed using 20x20 supercells with a single  $\mathbf{k}_{\parallel}$ -point in the downfolded BZ. This is equivalent to 400  $\mathbf{k}_{\parallel}$ -point sampling of the original BZ. In all three cases the diffusive contribution outweighs the specular one with most of the contribution coming from the area around the center of 2D BZ. It is only for the highest concentration that the transmission becomes more evenly spread over the 2D BZ.

### 3.5.3 Antiparallel spin alignment

The AP conductance assumes values intermediate between  $G_P^{maj}$  and  $G_P^{min}$ . Interestingly it can be approximated by a simple formula

$$G_{AP}^{\sigma} = \sqrt{G_P^{maj} G_P^{min}}. \quad (3.4)$$

As we see in Fig. 3.13, where the results of Eq. (3.4) are shown using dashed line, perfect agreement sets in as soon as the surface resonance contribution is killed by roughness [39]. Somewhat similar relation has been demonstrated before for the ideal MTJs [40]. It is easy to show that as long as Eq. (3.4) holds the TMR is positive.

## 3.6 Substitutional disorder: $Fe_xCo_{1-x}$ electrodes

In this section we study the transport properties of the MTJ with the electrodes composed of random  $Fe_{1-x}Co_x$  alloy. As discussed in Sec. 3.2 the calculations are performed for the structure shown schematically in the bottom panel of Fig. 3.1. The uniform potential in the leads is calculated using VCA. The substitutional disorder is introduced within the scattering region with Fe and Co atoms distributed over the lateral supercell. The potentials for these are calculated using CPA. We denote such structure as VCA|CPA|vacuum|CPA|VCA. Four MLs of disordered alloy are used on both sides of VTB with the thickness of the latter fixed to 8 MLs. See Appendix 3.9 for the discussion of the associated convergence issues.

The results of transport calculations for VCA|CPA|vacuum|CPA|VCA structure are shown in Fig. 3.16 using dashed lines. The overall trend seen in the figure is the decrease of the conductance with the increasing concentration of Co. The only

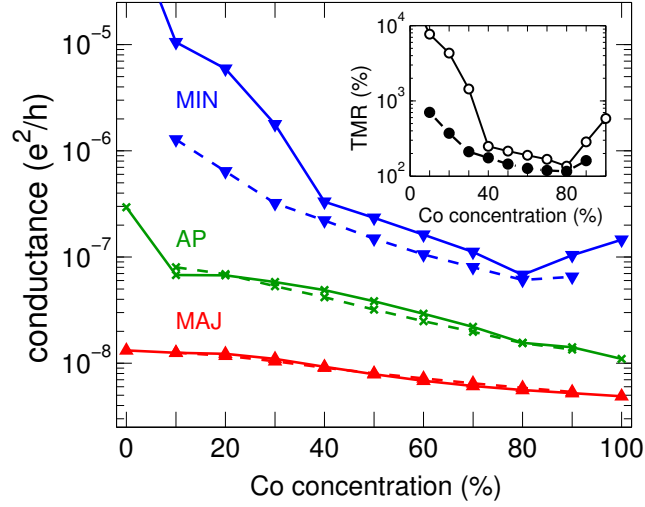


**Figure 3.16:**  $G_P^{min}$  ( $\blacktriangledown$ ),  $G_P^{maj}$  ( $\blacktriangle$ ), and  $G_{AP}^\sigma$  ( $\times$ ) for an  $\text{Fe}_{1-x}\text{Co}_x|\text{vacuum}|\text{Fe}_{1-x}\text{Co}_x$  MTJ with 8 MLs barrier width as a function of  $x$ , the concentration of Co atoms, calculated in the virtual crystal (VCA: solid lines) and CPA/supercell (SC: dashed lines) approximations. Conductances are configuration averaged and normalized to a  $1 \times 1$  surface unit cell. Inset: TMR in VCA ( $\circ$ ) and CPA/SC ( $\bullet$ ) approximations.

exception is the minority channel exhibiting an increase in a limit of Co concentrations over 80% that is when a limit of pure Co electrode is approached. Similarly TMR decreases with the increasing concentration of Co down to the 100% range and picks up again only for the largest concentrations. Overall the effect of substitutional disorder is similar to that of surface roughness discussed in the preceding section. The most spectacular changes take place in the minority channel and lead to the reduction of TMR ratio. However, no change of the polarization sign is observed.

The interpretation of numerical results is difficult in this case as the effects of substitutional disorder and the changes to the electronic structure are intertwined. In order to shed some light on the importance of the latter we have performed transport calculations also for ideal MTJ with the whole electrodes described using VCA. The results are shown as solid lines in Fig. 3.16 and empty symbols in the inset. The agreement between both sets of results is nearly perfect for majority and AP curves. For minority channel we see substantial differences for concentrations up to 10%. Above that both conductances assume comparable values up until 80% Co concentration where they start to diverge again. The two TMR curves reflect this behavior. As there is no symmetry breaking for VCA|vacuum|VCA structure the evolution of the conductance in this case must be related to the changes in underlying electronic structure. The transport for VCA|vacuum|VCA junction is initially

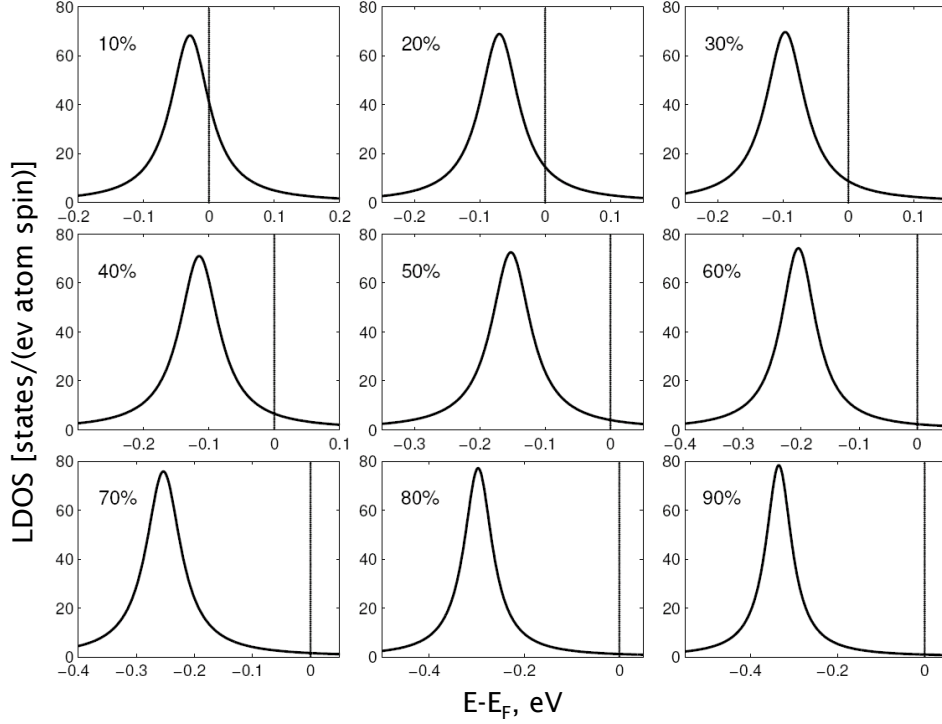


**Figure 3.17:** The LDOS with  $\Delta_1$  symmetry for different concentrations  $x$  of  $Fe_xCo_{1-x}$  alloy shown as a function of energy.

dominated by the resonant tunneling in the minority channel. However as the Co concentration increases the surface state is gradually removed from the vicinity of Fermi level. This is illustrated in Fig. 3.17 where we have shown the  $\Delta_1$  contribution to the LDOS at  $\bar{\Gamma}$  and the surface layer of the electrode. Once the contribution of the resonant states is switched off, the conductances for both structures become very similar. For VCA|CPA|vacuum|CPA|VCA MTJ the process is decrease of the minority conductance is sped up by the symmetry breaking and the presence of diffuse scattering

The antiparallel conductance is once again well described by Eq. (3.4).

### 3.7 Discussion and Conclusions

In this chapter the transport properties of  $Fe_xCo_{1-x}$ |vacuum| $Fe_xCo_{1-x}$  tunnel junctions using the first principles WFM method have been studied. Starting with ideal Fe|vacuum|Fe system it has been found that the minority channel in parallel configuration is dominated by resonant tunneling also found in other first-principles

calculations [10, 11, 41]. This effect is responsible for the predicted TMR ratio of 20,000%. The resonances take the form of “hot spots” that is the regions of 2D BZ where the tunneling takes place with little or no attenuation. Two kind of such resonances have been found. Type A spots are located close to the center of 2D BZ and are closely related to the surface state of  $\Delta_1$  symmetry which form on Fe(001) surface. The other set, type B, consists of points further removed from the center of the zone. This latter type resonances do not contribute meaningfully to the integrated conductance because of their extreme localization in the momentum space.

However, ideal junction will never be fabricated. In fact there are experimental evidences for presence of interfacial roughness and lead disorder etc in the real MTJs [7]. Disorder (surface roughness or substitutional disorder in the leads) has been found to decrease the huge TMR predicted for ideal system to order of magnitude of the experimental values [7, 9]. The interface roughness has two main competing effects: *i*) it increases the transmission due to decrease of effective barrier width and *ii*) by breaking the point group symmetry of the system it destroys the resonant and surface states thus decreasing the minority conductance and consequently TMR. The latter effect is most important for MTJs studied in the present paper where the resonant effects dominate the tunneling for ideal system. Even the small amount of disorder (roughness) is sufficient to substantially degrade the transmission in the minority channel even though the resonant states are likely not removed at this point. In the limit of strong disorder the minority conductance exhibits the same thickness dependence as the majority one which indicates that the resonance effects are entirely removed in this limit.

The effect of  $\text{Fe}_x\text{Co}_{1-x}$  alloy leads was studied using both VCA (ideal system) and CPA/supercell (substitutional disorder) approach. It has been found that the effect of disorder in this case is generally similar, although less spectacular, to that of surface roughness. Interestingly, the changes of the electronic structure caused by alloying Fe with Co are in themselves enough to effectively remove the surface and associated resonant states from the vicinity of the Fermi level. In this regime there is little difference between the results of VCA and CPA/supercell calculations.

Extremely high TMR ratios predicted by other groups for ideal Fe|MgO|Fe [10–12, 41] overestimate by far the values found in the experiment [7, 9]. The results for clean and disordered MTJs suggest that these experiments are still in the disorder limited regime. It should be noted however that direct application of our results to MgO based junctions can be disputed. Unlike for our systems, the tunneling through ideal MgO is not dominated by minority channel. Instead, the conduction is largest in the majority channel thanks to good matching of  $\Delta_1$  band states in Fe to the evanescent solutions within MgO energy gap. Therefore, even though the resonances has been predicted for the minority conductance their destruction by disorder might not have equally potent effect as for our Fe|vacuum|Fe.

Another interesting aspect of these results is that for the disordered junctions the conductance of antiparallel configuration can be successfully approximated using simple formula of Eq. (3.4). This suggests that the tunneling through a general non-



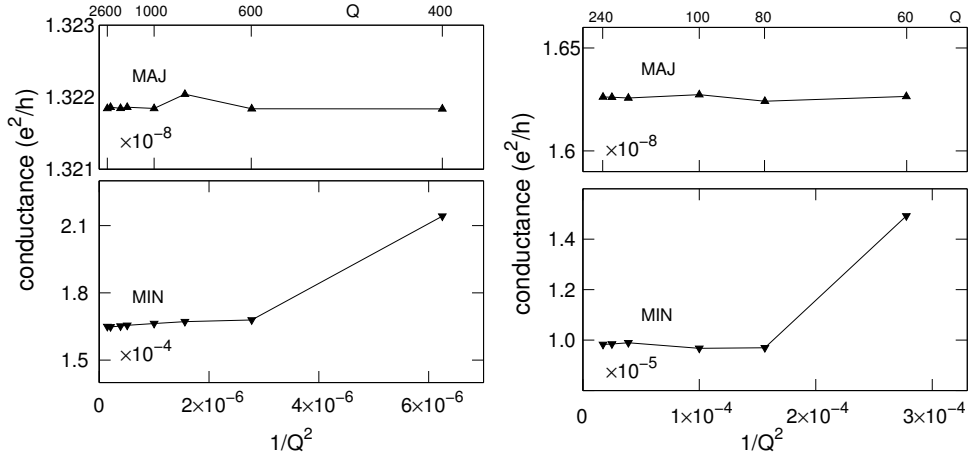


**Figure 3.18:** Conductance of ideal Fe|vacuum|Fe MTJ (left hand panel) and Fe|vacuum|Fe MTJ with 50% roughness in  $10 \times 10$  lateral supercell (right hand panel) for majority and minority spins for 8 MLs barrier width plotted as a function of the normalized area element in the Brillouin zone summation  $1/Q^2$ , where  $Q$  is the number of intervals along the reciprocal lattice vector.

symmetric junction can be expressed in a factorized form reminiscent of the Julliere formula [3].

### 3.8 Appendix 1: The k-point sampling

Calculation of the conductance involves the summation over a set of  $\mathbf{k}_{\parallel}$  points that is integration over the 2D BZ. Naturally, a question arises about the number of points necessary to achieve sufficient accuracy. In view of the qualitative differences in the nature of transmission through ideal and disordered system we will address these to cases separately.

The majority and minority parallel conductances in case of ideal Fe|vacuum|Fe MTJ (left hand panel) and Fe|vacuum|Fe MTJ with 50% roughness in  $10 \times 10$  lateral supercell (right hand panel) with 8 MLs of vacuum barrier are shown in Fig. 3.18 as the function of the normalized area element in the Brillouin zone summation  $1/Q^2$ , where  $Q$  is the number of divisions of the reciprocal lattice vectors. As it can be seen both conductances in case of ideal MTJ are essentially converged for  $Q$  over 600. Note that resolving of the B type resonances would require  $Q > 10^7$ . However thanks to their extreme localization these resonances can be safely ignored as they do not contribute to the total integrated conductance. The same procedure has been applied to a system with surface roughness at 50% coverage modelled using  $10 \times 10$  supercells. We see that both conductances, especially minority, converge much faster

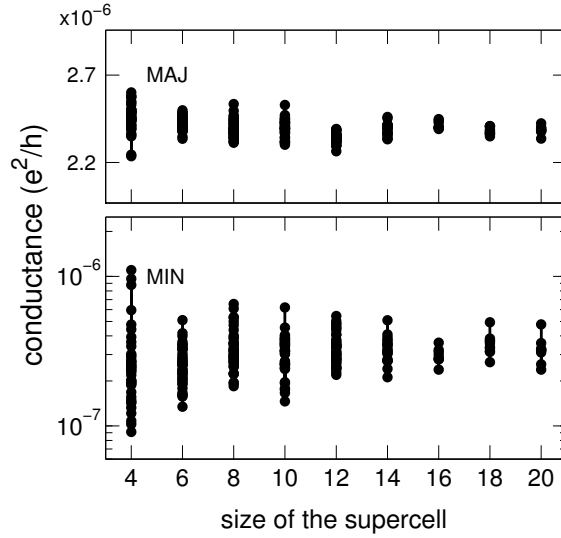


**Figure 3.19:** Conductance of Fe|vacuum|Fe MTJ with 50% roughness in a  $\sqrt{H} \times \sqrt{H}$  lateral SC for majority and minority spins for 8 MLs barrier width plotted as a function of  $\sqrt{H}$ . The results are given for different randomly generated configurations of disorder.

and the values are stabilized already for  $Q > 80$ . Better convergence is caused by the destruction of the localized resonances in the minority channel. The other factor involved is that in downfolded BZ of the supercell the sampling for a given value of  $Q$  corresponds to 100 times (for 10x10 supercell) as many points in the original BZ.

### 3.9 Appendix 2: Configurational averaging and the size of the scattering region

Modeling of the disorder by means of lateral supercells becomes exact for infinitely large supercells. Of course all practical calculations have to be performed using the cells of the finite size. It is therefore important to estimate the inaccuracies introduced by the finite size of the cells. In order to estimate these, the conductance calculations for disordered (surface roughness) Fe|vacuum|Fe junction using 20 (40 for smaller systems) different configurations of disorder for superlattices of increasing size ( $\sqrt{H}$ ) have been performed. The results, shown in Fig. 3.19, demonstrate relatively slow convergence in minority channel in comparison to the metallic interfaces [24]. This reflects the fact that the tunneling transmission probabilities are hugely sensitive (exponential dependence) to the local variation in the thickness of VTB. The averaged values on the other hand are well converged already for  $\sqrt{H} = 10$  case. Increasing

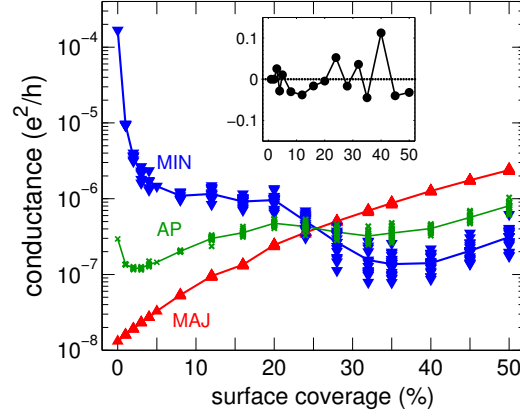


**Figure 3.20:** Conductances  $G_P^{min}(\blacktriangledown)$ ,  $G_P^{maj}(\blacktriangle)$ , and  $G_{AP}^\sigma(\times)$  of an Fe|vacuum|Fe MTJ with 8 MLs barrier width as a function of the surface coverage, normalized to a  $1 \times 1$  surface unit cell are shown for all calculated configurations of disorder at the interface layers. Inset: The difference in conductance between two antiparallel spin channels normalized to the full AP conductance shown as a function of surface coverage.

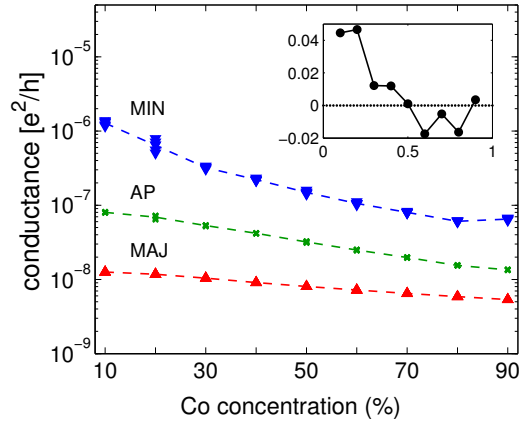


**Figure 3.21:** Conductances  $G_P^{min}(\blacktriangledown)$ ,  $G_P^{maj}(\blacktriangle)$ , and  $G_{AP}^\sigma(\times)$  of an  $\text{Fe}_{1-x}\text{Co}_x$ |vacuum| $\text{Fe}_{1-x}\text{Co}_x$  MTJ with 8 ML barrier width as a function of  $x$ , the concentration of Co atoms, calculated in the CPA/supercell approximation. Results are shown for all calculated configurations of disorder. Inset: The difference in conductance between two antiparallel spin channels normalized to the full AP conductance.

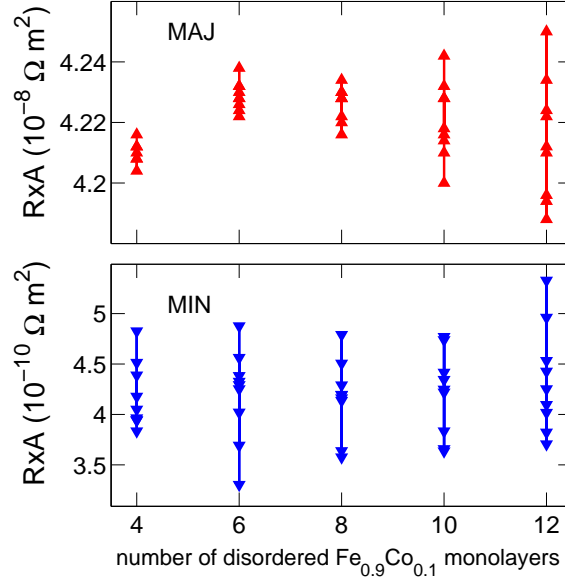


**Figure 3.22:** Resistance of  $\text{Fe}_{0.9}\text{Co}_{0.1}|\text{vacuum}|\text{Fe}_{0.9}\text{Co}_{0.1}$  MTJ as a function of number of disordered FeCo monolayers on each side of the vacuum tunneling barrier in the scattering region.

the size of the supercell makes the calculations considerably more expensive. As there is little to be gained from using supercells larger than  $10 \times 10$ , this size for all the calculations performed in the main body of the text has been chosen.

In order to verify that above mentioned convergence is not significantly different also for coverages smaller than 50% we show in Fig. 3.20 the non-averaged results corresponding to Fig. 3.13. The lines connect the averaged values, same as in Fig. 3.13. As we can see the spread of values can be considerable but the spin channels remain well separated and the general trends are well reproduced by averaged values. The disorder described using the supercells of finite size and a single configuration of scatterers breaks the mirror symmetry of the ideal junction and allows the conductances of the two spin channels in AP configuration to diverge. However a truly random disorder is expected to restore the symmetry and brings the two spin channels into agreement. Therefore the agreement between configuration-averaged AP conductances serves as a useful metrics for the validity of our approach to disorder modeling. In the inset of Fig. 3.20 we show the normalized difference of averaged antiparallel conductances  $\varepsilon$  defined as:

$$\varepsilon = 2 \frac{G_{AP}^1 - G_{AP}^2}{G_{AP}^1 + G_{AP}^2} \quad (3.5)$$

where the  $G_{AP}^\sigma$  is configurationally averaged AP conductance. As we can see the

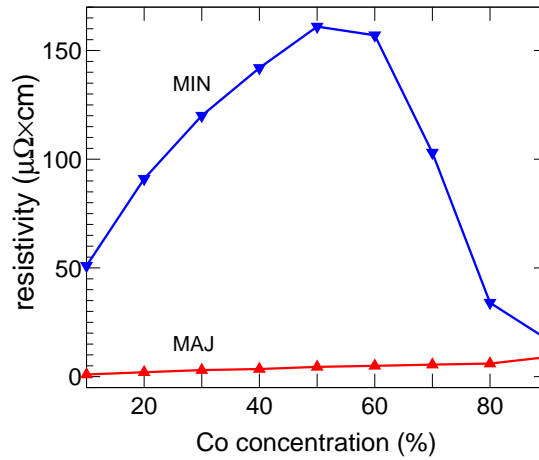


**Figure 3.23:** Resistivity of disordered  $\text{Fe}_{1-x}\text{Co}_x$  alloy as a function of Co concentration  $x$  for both majority and minority spin channels.

values of  $\varepsilon$  remain modest all throughout the range of coverages. Similar conclusions can be drawn for alloy disorder case as it is demonstrated by Fig. 3.21.

Another problem arises in calculations for the junctions with  $\text{Fe}_x\text{Co}_{1-x}$  electrodes where the substitutional disorder is restricted only to the part of the electrodes contained within the scattering region (Fig. 3.1, bottom panel). Simple VCA approximation is used for the remaining parts of electrodes. This approach makes the calculations feasible but can potentially also be a source of inaccuracies. In Fig. 3.22 we show resistances calculated for different configurations of substitutional disorder in  $\text{Fe}_{0.9}\text{Co}_{0.1}$  alloy and MTJs with 4 to 12 MLs included in the scattering region on both sides of the barrier. The spread of values is relatively large and convergence slow, especially in the minority channel. The average values, on the other hand, remain essentially the same even though we are increasing the size of the scattering region. The reason for this is that the resistance of MTJ is dominated by the tunneling through the barrier. Indeed using the values of resistivity for  $\text{Fe}_x\text{Co}_{1-x}$ , plotted in Fig 3.23, we conclude that the resistance of several layers of an alloy is insignificant compared to the resistances given in Fig. 3.22 for the whole MTJ by many orders of magnitude. The numbers in Fig. 3.23 were determined by the calculation of the inverse of the conductance for the  $\text{Fe}_x\text{Co}_{1-x}$  slab of varying thickness and extracting the resistivities from the slope of the curve (Ohm's law). All the calculations in the main body of the text were performed with just 4 MLs of disordered alloy on both sides of VTB. As we have seen in Sec. 3.6 it is enough to break the symmetry and destroy the resonant states in the minority channel. This is further confirmed in Fig. 3.21 which corresponds to the Fig. 3.16 in the main text. As we can see the spread of non-averaged values is insignificant on the scale of the plot. The normalized differences of the AP conductances, shown in the inset, are also in good agreement.

## Bibliography

- [1] J. S. Moodera, L. R. Kinder, T. M. Wong, and R. Meservey, *Phys. Rev. Lett.* **74**, 3273 (1995).
- [2] J. M. De Teresa *et al.*, *Science* **286**, 507 (1999).
- [3] M. Julliere, *Phys. Lett. A* **54**, 225 (1975).
- [4]  $P_i$  was not defined strictly in Ref. [3] and it has frequently been interpreted in terms of the density-of-states polarization  $P = [D_{\uparrow}(\varepsilon_f) - D_{\downarrow}(\varepsilon_f)]/[D_{\uparrow}(\varepsilon_f) + D_{\downarrow}(\varepsilon_f)]$  where  $D_{\sigma}(\varepsilon)$  is a bulk density of states. It has been pointed out [42] that other measures of the spin polarization may be more appropriate when studying transport.
- [5] E. Y. Tsymbal, O. N. Mryasov, and P. R. LeClair, *J. Phys.: Condens. Matter.* **15**, R109 (2003).
- [6] X.-G. Zhang and W. H. Butler, *J. Phys.: Condens. Matter.* **15**, R1603 (2003).
- [7] S. Yuasa, T. Nagahama, A. Fukushima, Y. Suzuki, and K. Ando, *Nature Materials* **3**, 868 (2004).
- [8] S. Yuasa *et al.*, *Appl. Phys. Lett.* **87**, 222508 (2005).
- [9] S. S. P. Parkin *et al.*, *Nature Materials* **3**, 862 (2004).
- [10] W. H. Butler, X.-G. Zhang, T. C. Schulthess, and J. M. MacLaren, *Phys. Rev. B* **63**, 054416 (2001).
- [11] J. Mathon and A. Umerski, *Phys. Rev. B* **63**, 220403(R) (2001).
- [12] D. Wortmann, G. Bihlmayer, and S. Blügel, *J. Phys.: Condens. Matter.* **16**, s5819 (2004).
- [13] X.-G. Zhang, W. H. Butler, and A. Bandyopadhyay, *Phys. Rev. B* **68**, 092402 (2003).
- [14] C. Tusche *et al.*, *Phys. Rev. Lett.* **95**, 176101 (2005).
- [15] P. X. Xu *et al.*, *Phys. Rev. B* **73**, 180402(R) (2006).
- [16] J. A. Stroscio, D. T. Pierce, A. Davies, R. J. Celotta, and M. Weinert, *Phys. Rev. Lett.* **75**, 2960 (1995).
- [17] S. F. Alvarado, *Phys. Rev. Lett.* **75**, 513 (1995).
- [18] S. N. Okuno, T. Kishi, and K. Tanaka, *Phys. Rev. Lett.* **88**, 066803 (2002).
- [19] H. F. Ding, W. Wulfhekel, J. Henk, P. Bruno, and J. Kirschner, *Phys. Rev. Lett.* **90**, 116603 (2003).

- 
- [20] M. M. J. Bischoff, T. K. Yamada, C. M. Fang, R. A. de Groot, and H. van Kempen, *Phys. Rev. B* **68**, 045422 (2003).
- [21] I. Turek, V. Drchal, J. Kudrnovský, M. Šob, and P. Weinberger, *Electronic Structure of Disordered Alloys, Surfaces and Interfaces* (Kluwer, Boston-London-Dordrecht, 1997).
- [22] O. K. Andersen, Z. Pawłowska, and O. Jepsen, *Phys. Rev. B* **34**, 5253 (1986).
- [23] U. von Barth and L. Hedin, *J. Phys. C: Sol. State Phys.* **5**, 1629 (1972).
- [24] K. Xia, M. Zwierzycki, M. Talanana, P. J. Kelly, and G. E. W. Bauer, *Phys. Rev. B* **73**, 064420 (2006).
- [25] T. Ando, *Phys. Rev. B* **44**, 8017 (1991).
- [26] S. Datta, *Electronic Transport in Mesoscopic Systems* (Cambridge University Press, Cambridge, 1995).
- [27] P. Soven, *Phys. Rev.* **156**, 809 (1967).
- [28] K. Schwarz, P. Mohn, P. Blaha, and J. Kübler, *J. Phys. F: Met. Phys.* **14**, 2659 (1984).
- [29] The Fe and Co lattice constants correspond to Wigner-Seitz atomic sphere radii of 2.667 and 2.621 Bohr atomic units, respectively.
- [30] J. M. MacLaren, T. C. Schulthess, W. H. Butler, R. Sutton, and M. McHenry, *J. Appl. Phys.* **85**, 4833 (1999).
- [31] H. L. Skriver and N. M. Rosengaard, *Phys. Rev. B* **46**, 7157 (1992).
- [32] Current conservation test is performed for all transport calculations. Transmission and reflection coefficients are calculated and their sum is compared with the number of electronic states for every  $\mathbf{k}_{\parallel}$  point. Difference between these two appears due to the computational errors. In calculations presented here it has been not higher than  $10^{-12}$ . This number sets a limit on the smallest calculated conductances which can be trusted. For this reason MTJ with with VTB thickness larger than 10 MLs are not considered here.
- [33] The conductance polarization changes sign from positive to negative as the vacuum separation is increased. The positive polarization found by MacLaren *et al.* [43] can be reproduced by using non selfconsistent potentials and small number of  $\mathbf{k}$  points.
- [34] O. Wunnicke *et al.*, *Phys. Rev. B* **65**, 064425 (2002).
- [35] C. Uiberacker and P. M. Levy, *Phys. Rev. B* **64**, 193404 (2001).
- [36] C. Uiberacker and P. M. Levy, *Phys. Rev. B* **65**, 169904(E) (2002).

- [37] The WFM method does not require the introduction of complex energies when calculating the Green function matrix. However it is convenient to add imaginary part when calculating DOS in order to smooth out the plots. All the DOS calculations in the current manuscript were performed with imaginary part  $\eta = 0.034eV$ .
- [38] P. A. Khomyakov, G. Brocks, V. Karpan, M. Zwierzycki, and P. J. Kelly, Phys. Rev. B **72**, 035450 (2005).
- [39] For ideal MTJs, the resonant tunneling contribution will be quenched for sufficiently thick barriers so Eq. (3.2) can also be expected to hold in that situation.
- [40] K. D. Belashchenko *et al.*, Phys. Rev. B **69**, 174408 (2004).
- [41] K. D. Belashchenko, J. Velez, and E. Y. Tsymbal, Phys. Rev. B **72**, 140404 (2005).
- [42] I. I. Mazin, Phys. Rev. Lett. **83**, 1427 (1999).
- [43] J. M. MacLaren, X.-G. Zhang, and W. H. Butler, Phys. Rev. B **56**, 11827 (1997).



## Chapter 4

# Recovering the Jullière model by including interface disorder

*A model proposed by Jullière relates the tunneling magnetoresistance (TMR) to conduction-electron or tunneling spin-polarizations which are properties of individual electrodes that can be measured separately. Despite much experimental evidence supporting this model, the factors governing the tunneling spin-polarizations and the related tunneling densities-of-states are poorly understood and our microscopic understanding of the Jullière model far from complete.*

*We use a first-principles scattering formalism to study transport through the simplest possible magnetic tunnel junction with non-trivial transition metal (TM) electrodes, a TM|vacuum|TM junction. Including only interface roughness is enough to recover a Jullière-like factorization of the TMR and to allow us to study the factors entering the tunneling spin-polarization. We then show how the procedure can be generalized to the finite bias case leading to a substantial reduction in the computational cost. We illustrate the approach by showing how the sign of the TMR can change as a function of the bias potential for an Fe|vacuum|Fe MTJ if the interface roughness is sufficiently different on the two interfaces.*

### 4.1 Introduction

Magnetoresistive (MR) effects attract a lot of interest because of the considerable scope they offer to increase the density of data stored on hard disk drives by reducing the size of read heads and as the basis for both reading and writing mechanisms in magnetic random-access memories. In this chapter, we focus on the tunneling magnetoresistance (TMR) observed in magnetic tunnel junctions (MTJ) that consist of two ferromagnetic leads (FM) separated by a thin insulating (I) layer. The electrical resistance of an FM|I|FM junction depends on the relative orientation of the

magnetizations in the leads which can be changed from antiparallel (AP) to parallel (P) by applying an external magnetic field along one of the magnetization directions. In the so-called “optimistic” definition, the tunneling magnetoresistance is defined as  $\text{TMR} \equiv (G_P - G_{AP})/G_{AP} \equiv (R_P - R_{AP})/R_P$ , where  $G_P$  ( $R_P$ ) and  $G_{AP}$  ( $R_{AP}$ ) are the total conductances (resistances) of a junction in the P and AP orientations, respectively.

Despite significant progress in realizing MTJs with high values of TMR at room-temperature [1], our understanding of the factors governing the TMR is still very unsatisfactory. One of the earliest models, and certainly the one most frequently used, was proposed by Jullière [2]. It is based upon two approximations. First, it is assumed that the spin of electrons is conserved during tunneling. This assumption is known as Mott’s two-current approximation [3, 4]. Second, it is assumed that the conductance in each spin channel ( $\sigma = \text{maj, min}$  or  $\sigma = 1, 2$ ; in an AP configuration, majority and minority are only well-defined in individual leads) is proportional to the product of spin-dependent tunneling densities of states (TDOS)  $\rho_i^\sigma$  in the left (L) and right (R) FM leads,  $i = L, R$ :

$$\begin{aligned} G_P &= G_P^{\text{maj}} + G_P^{\text{min}} \propto \rho_L^{\text{maj}} \rho_R^{\text{maj}} + \rho_L^{\text{min}} \rho_R^{\text{min}}, \\ G_{AP} &= G_{AP}^1 + G_{AP}^2 \propto \rho_L^{\text{maj}} \rho_R^{\text{min}} + \rho_L^{\text{min}} \rho_R^{\text{maj}}. \end{aligned} \quad (4.1)$$

If the FM leads are identical  $\rho_L^\sigma = \rho_R^\sigma = \rho^\sigma$  and  $G_{AP}$  is given by

$$G_{AP} = 2\sqrt{G_P^{\text{maj}} G_P^{\text{min}}} \propto 2\rho^{\text{maj}} \rho^{\text{min}}. \quad (4.2)$$

In terms of this model, the TMR can be expressed as  $2\mathcal{P}_L\mathcal{P}_R/(1 - \mathcal{P}_L\mathcal{P}_R)$ , where  $\mathcal{P}_L$  and  $\mathcal{P}_R$  are the conduction-electron or tunneling spin-polarizations (TSP) of left and right leads given by  $\mathcal{P}_i = (\rho_i^{\text{maj}} - \rho_i^{\text{min}})/(\rho_i^{\text{maj}} + \rho_i^{\text{min}})$ . The TSP can be measured in an electrical transport measurement for an FM|I|S junction where S is a superconductor [5, 6]. Values of the TSP measured in this way predict the TMR correctly if the FM|I interface is the same in the FM|I|FM and FM|I|S experiments [7–9]. This indicates that the TSP is a property of an FM|I interface and not a property of a bulk ferromagnetic material. Factorization of the TMR in this way is an important simplification and it needs to be shown how it might follow from a more fundamental theory.

The success of Jullière’s model in describing the TMR in terms of TSPs conceals how poorly we understand the  $\rho_i^\sigma$  in terms of which the TSP is defined. Originally specified [5] in an operational fashion, the *tunneling* density-of-states is frequently assumed to be just equal to  $D_i^\sigma(E_F)$ , the spin-projected bulk density-of-states at the Fermi energy  $E_F$ . However, the experimental demonstration that the TMR depends on the barrier material used [10–13] or the theoretical demonstration that it depends sensitively on interface roughness [14] show that this simple interpretation is not tenable.

The structure of this chapter is as follows. In the next section, we briefly review a number of studies [15–21] which have contributed to our theoretical understanding

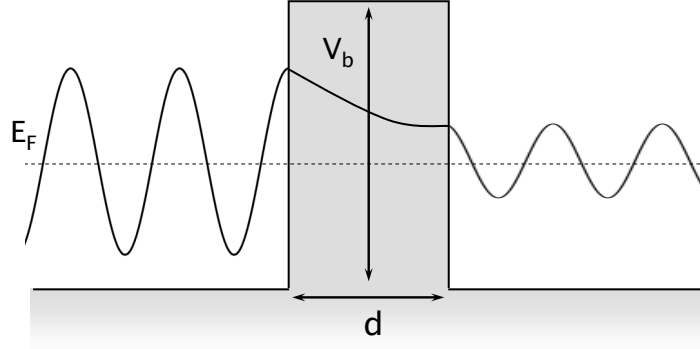


**Figure 4.1:** Schematic representation of free-electron tunneling through an ideal rectangular barrier.

of TMR and form the background to our own *ab-initio* work which is presented in Section 4.3. We introduce a new expression for the TMR which has the same form as (4.1) as well as a factorization procedure which allows us study both zero and finite bias cases. We summarize our results and draw some conclusions in Section 4.4.

## 4.2 Early models

In the more than thirty years since Jullière proposed his model, a number of theoretical approaches have been proposed to study spin-dependent transport in MTJs. One of the first was an adaptation by Slonczewski [15] of the textbook tunnel barrier to include exchange-split free electron gases on either side of the ideal rectangular tunnel barrier of height  $V_b$  and width  $d$  shown in Fig. 4.1. The exchange-splitting is included by introducing different constant potentials,  $V_{maj}$  and  $V_{min}$ , for the two spin channels. Assuming translational periodicity in the plane of the barrier, the tunneling conductance is given by

$$G^\sigma = \frac{e^2}{h} \sum_{\mathbf{k}_\parallel} T^\sigma(\mathbf{k}_\parallel), \quad (4.3)$$

where  $\mathbf{k}_\parallel$  is the conserved transverse momentum and  $T^\sigma(\mathbf{k}_\parallel)$  is the spin-dependent transmission probability. By matching the wave functions and their derivatives at the left and right interfaces between the FM leads and non-magnetic barrier, the  $T^\sigma(\mathbf{k}_\parallel)$  can be found. For  $V_{maj} < E_F$ ,  $V_{min} < E_F$  and  $E_F < V_b$ , the expression for  $T^\sigma(\mathbf{k}_\parallel)$  simplifies in the limit of thick tunnel barriers (large  $d$ ) to

$$T^\sigma(\mathbf{k}_\parallel) = \frac{16k_L^\sigma k_R^\sigma \kappa^2}{(k_L^{\sigma^2} + \kappa^2)(k_R^{\sigma^2} + \kappa^2) \exp(-2\kappa d)}, \quad (4.4)$$

where  $k_i^\sigma = \sqrt{(2m/\hbar^2)(E_F - V_\sigma) - k_{\parallel}^2}$  is the component of the wavevector normal to the interface of electrons propagating at the Fermi level in the left and right leads and  $\kappa = \sqrt{(2m/\hbar^2)(V_b - E_F) + k_{\parallel}^2}$  describes the evanescent states inside the tunnel barrier. Taking into account that the magnetizations of the left and right electrodes can be oriented parallel or antiparallel, this equation can be rewritten as

$$T^{\sigma\sigma'}(\mathbf{k}_{\parallel}) = T_L^\sigma(\mathbf{k}_{\parallel}) \exp(-2\kappa d) T_R^{\sigma'}(\mathbf{k}_{\parallel}), \quad (4.5)$$

where  $T_L^\sigma(\mathbf{k}_{\parallel})$  and  $T_R^{\sigma'}(\mathbf{k}_{\parallel})$  are the spin-dependent transmission coefficients calculated at the left and right FM|I interfaces, respectively,

$$T_i^\sigma(\mathbf{k}_{\parallel}) = \frac{4k_i^\sigma \kappa}{(k_i^{\sigma^2} + \kappa^2)}. \quad (4.6)$$

In Eq. (4.5)  $\sigma = \sigma'$  for P and  $\sigma \neq \sigma'$  for AP aligned magnetizations. To calculate the total conductance, one should sum over all  $\mathbf{k}_{\parallel}$  contributions in the two-dimensional Brillouin zone (2D BZ) according to (4.3). In the limit of thick barriers, however, this is not necessary because the exponential dependence on  $\kappa$  means that, with the exception of the  $\mathbf{k}_{\parallel} = 0$  term, all other contributions can be neglected. The total P and AP conductances are then

$$G_P \approx \frac{e^2}{h} \exp(-2\kappa d) \left[ T_L^{maj}(0) T_R^{maj}(0) + T_L^{min}(0) T_R^{min}(0) \right], \quad (4.7)$$

$$G_{AP} \approx \frac{e^2}{h} \exp(-2\kappa d) \left[ T_L^{maj}(0) T_R^{min}(0) + T_L^{min}(0) T_R^{maj}(0) \right].$$

Comparing Eqs. (4.7) and (4.1) we see that the role of the TDOS,  $\rho_i^\sigma$  in the Jullière model, is played by the transmission coefficient  $T_i^\sigma(0)$  and  $(e^2/h)\exp(-2\kappa d)$  is the proportionality coefficient missing in (4.1). Slonczewski's TSP can be written as

$$\mathcal{P}_i^S = \frac{T_i^{maj}(0) - T_i^{min}(0)}{T_i^{maj}(0) + T_i^{min}(0)} = \mathcal{P}_i \frac{\kappa^2 - k_i^{maj} k_i^{min}}{\kappa^2 + k_i^{maj} k_i^{min}}, \quad (4.8)$$

where

$$\mathcal{P}_i = \frac{k_i^{maj} - k_i^{min}}{k_i^{maj} + k_i^{min}} \quad (4.9)$$

is the TSP which would result from assuming  $\rho_i^\sigma \equiv D_i^\sigma(E_F)$  in the free electron limit. The TSP given in (4.8) depends not only on the electronic properties of the FM leads as described by  $\mathcal{P}_i$ , but also on those of the tunnel barrier.  $\mathcal{P}_i^S$  is also known as a generalized TSP. For the spin-polarized free electron model, the TMR can be evaluated numerically essentially exactly. In the limit of large  $d$  and small  $V_b$ , the functional dependence of the TMR on  $\mathcal{P}$  ( $\equiv \mathcal{P}_{L,R}$  for symmetrical junctions with identical leads) is reasonably well described by (4.8) [15, 19]. Eqs. (4.5) and (4.6) are important because the ( $\mathbf{k}_{\parallel}$ -dependent) transmission factorizes into terms

corresponding to transmission from the left lead into the barrier, attenuation in the barrier, followed by transmission from the barrier into the right lead. The multiple reflections which would make this factorization impossible can be neglected because of the assumed strong attenuation by the tunnel barrier. If the tunnel junction is sufficiently symmetrical that resonant tunneling can occur, strong attenuation is not a sufficient condition to neglect multiple reflections [22]. Unlike the empirical Jullière model which quite successfully relates TMRs and TSPs determined for the same FM|I interfaces, the realm of validity of the free electron approach is much more limited because of the difficulty of unambiguously mapping the complex open  $d$ -shell electronic structure of real itinerant electron magnetic materials onto free electron models.

The factorization discussed in relation to (4.5) is a general property of waves and is not restricted to the free-electron model [20, 23]. Assuming lattice periodicity in the plane of the barrier and sufficient barrier attenuation to suppress multiple reflections, (4.5) can be generalized as

$$T^{\sigma\sigma'}(\mathbf{k}_{\parallel}) \approx T_L^{\sigma}(\mathbf{k}_{\parallel})T_m(\mathbf{k}_{\parallel})T_R^{\sigma'}(\mathbf{k}_{\parallel}) \quad (4.10)$$

where  $T_L^{\sigma}(\mathbf{k}_{\parallel})$  and  $T_R^{\sigma'}(\mathbf{k}_{\parallel})$  describe incoming and outgoing states in the left and right FM leads, respectively, and  $T_m(\mathbf{k}_{\parallel})$  describes the spin-independent attenuation inside a tunnel barrier. Unlike the free-electron case, analytical expressions for the spin-dependent transmission probabilities  $T_i^{\sigma}$  and for the spin-independent barrier attenuation  $T_m$  cannot be derived for realistic MTJs. For sufficiently thick tunnel barriers, the summation over  $\mathbf{k}_{\parallel}$  reduces to one or more discrete values of  $\mathbf{k}_{\parallel}$  corresponding to minimal attenuation at the valence band maxima and conduction band minima of the tunnel barrier.

The above factorization concerns MTJs which have translational periodicity parallel to the interface and the factorization occurs for each individual value of  $\mathbf{k}_{\parallel}$ . If we multiply (4.10) by  $e^2/h$ , we can use it to write

$$G_{AP}^{\sigma}(\mathbf{k}_{\parallel}) = \sqrt{G_P^{maj}(\mathbf{k}_{\parallel}) G_P^{min}(\mathbf{k}_{\parallel})}. \quad (4.11)$$

This  $\mathbf{k}_{\parallel}$ -dependent factorization was studied by Belashchenko *et al.* using a first-principles transmission matrix formulation. It was found to hold quite well for clean (111) and (001) Co|vacuum|Co MTJs as long as the vacuum barrier was sufficiently thick [20] but not for a Co|Al<sub>2</sub>O<sub>3</sub>|Co MTJ [21]. A key question is to determine how to proceed from such a factorization to a Jullière-like model. It is reasonably clear that transverse momentum-destroying disorder must play a role [16–18]. Because TMR had been mainly studied in MTJs based upon amorphous Al<sub>2</sub>O<sub>3</sub> tunnel barriers, it was often assumed that barrier disorder was responsible for this symmetry breaking. However, recently, large values of TMR were observed in FM|MgO|FM MTJs where the MgO tunnel barriers were (poly)crystalline [9, 24] and the TMR values were consistent with TSPs determined for FM|MgO|Al junctions [9]. This adds extra urgency to the need to better understand the factors governing the TMR, TSP and the validity of the Jullière model.

If, as the MgO results seem to indicate, disorder in the tunnel barrier and in the leads is not responsible for a Jullière like factorization, the question arises whether interface disorder on its own is sufficient [18]. We address this issue in the present chapter by studying the effect of interface disorder on TMR in a “semi-realistic” Fe|vacuum|Fe MTJ. This is the most complex model of a MTJ for which disorder can currently be studied without sacrificing the realistic treatment of the electronic band structure responsible for transition metal itinerant magnetism and, ultimately, for giant magnetoresistance.

### 4.3 *Ab-initio* results

We begin by briefly summarizing how the calculations were performed. In the absence of experimental information on interface disorder (which in the present model is equivalent to surface roughness) we calculate the transmission from first-principles within the framework of density functional theory (DFT). For an Fe|vacuum|Fe MTJ, the calculation proceeds as follows [14, 25, 26]. Self-consistent DFT calculations are first performed by solving the Kohn-Sham equations for bulk Fe. These calculations yield charge- and spin- densities and potentials, and the corresponding Fermi energy. A self-consistent calculation is then performed for the MTJ subject to the potentials (and densities) far from the junction being equal to their bulk values [27]. The junction breaks the lattice periodicity perpendicular to the surface leaving only two-dimensional periodicity in the plane of the junction that is characterized by the Bloch vector  $\mathbf{k}_{\parallel}$ . The electronic structure of the localized perturbation formed by the tunnel junction is handled using a Green’s function method, a so-called “Surface Green’s Function” (SGF). The rank of the matrix of the perturbation is made finite by making use of translational symmetry parallel to the interface and minimized by using a maximally-localized basis of tight-binding (TB) muffin-tin orbitals (MTOs) [28, 29]. To calculate the transmission matrix element  $t_{nm}(E)$  at real energies (at or close to the Fermi energy in the context of transport), we use a wave-function-matching scheme due to Ando [30] which involves the calculation of individual scattering states  $n$  and  $m$ . The rank of the transmission matrix is determined by the number of Bloch states at a given energy  $E$  and transverse wave-vector  $\mathbf{k}_{\parallel}$ . The transmission coefficient  $T(E, \mathbf{k}_{\parallel})$  is obtained by summing over all incoming and outgoing channels,  $T(E, \mathbf{k}_{\parallel}) = \text{Tr}\{\mathbf{t}(E, \mathbf{k}_{\parallel})\mathbf{t}^{\dagger}(E, \mathbf{k}_{\parallel})\}$ . The minimal TB-MTO basis is very efficient making it possible to model disorder using large lateral supercells [25, 26, 31] containing  $10 \times 10$  sites per atomic layer in the present case. Surface roughness where one or more layers of atoms is incomplete is conveniently treated by calculating the potentials self-consistently using a layer version [27] of the coherent potential approximation [32] and then distributing at random the site potentials in the lateral supercells subject to maintenance of the appropriate layer concentrations [25]. This method allows us to calculate “exact” values of the conductances  $G_P$  and  $G_{AP}$  and from them, the TMR. We can also calculate atom-resolved local densities of states (LDOS) in order to evaluate approximating the TSP by a LDOS [6]. We focus on surface roughness because, as shown in the previous chapter, it has a larger effect on

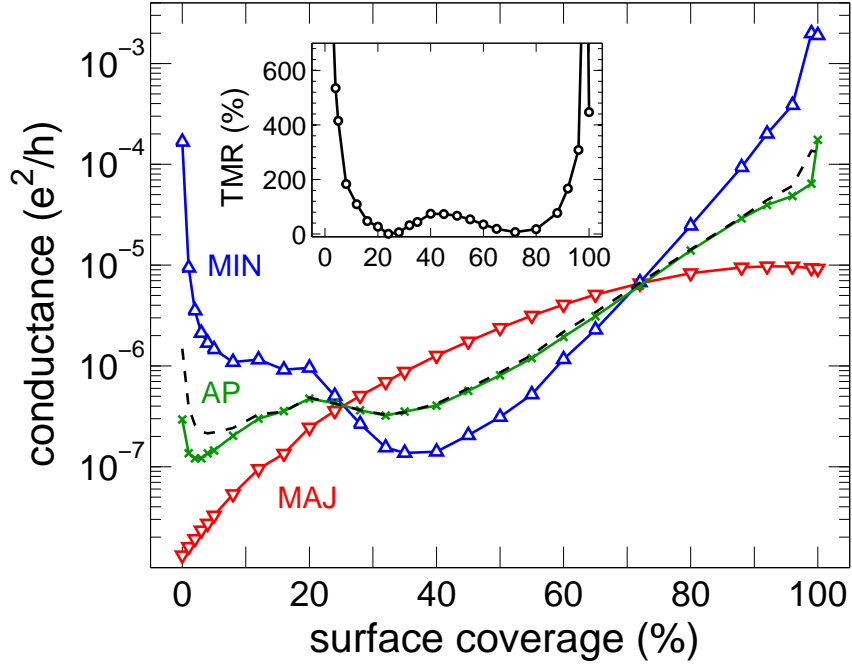


**Figure 4.2:** Configuration-averaged conductances  $G_P^{min}$  ( $\blacktriangledown$ ),  $G_P^{maj}$  ( $\blacktriangle$ ), and  $G_{AP}^\sigma$  ( $\times$ ) of an Fe|vacuum|Fe MTJ as a function of the surface coverage, normalized to a  $1 \times 1$  surface unit cell. The barrier width for the MTJ with clean surface for  $x = 0\%$  ( $x = 100\%$ ) is 8 MLs (6 MLs). The dashed line denotes  $G_{AP}^\sigma$  predicted from (4.12). Inset: TMR as a function of the surface coverage.

the TMR than alloy lead disorder [14] and is unambiguously localized at the FM|I interface: the Fe leads are perfectly ordered and the vacuum barrier is structureless. There are also many experimental studies of spin-dependent vacuum tunneling in its own right [33–37].

The effect of “interface disorder” on the TMR is illustrated in Fig. 4.2. In this figure,  $G_P^\sigma$  and  $G_{AP}^\sigma$  are shown as a function of the surface roughness for each spin channel. The surface coverage  $x$  characterizes the disorder and corresponds to a concentration of Fe impurity atoms on each surface. Because  $x$  is here the same for the left and right surfaces,  $x_L = x_R \equiv x$ , we call this MTJ symmetric. The microscopic configuration of adatoms on each surface is, however, different. The left-hand ( $x = 0\%$ ) and right-hand ( $x = 100\%$ ) sides of the figure correspond to ideal Fe|vacuum|Fe MTJs with the equivalent of 8 and 6 monolayers (MLs) respectively of vacuum<sup>1</sup>.

The monotonic increase of  $G_P^{maj}$  in Fig. 4.2 is attributed to the continuous de-

<sup>1</sup>thickness of a vacuum ML is equal to a half lattice constant of Fe  $a_{Fe}/2 = 1.433 \text{ \AA}$

crease of the average vacuum barrier width as the surface coverage increases. The more-complicated behaviour exhibited by  $G_P^{min}$  is due to the effect of roughness on a well-documented surface state on the Fe(001) surface [33]. When the surface is ideal, this state is strictly localized at the centre of the 2D BZ,  $\mathbf{k}_{\parallel} = \bar{\Gamma}$ , but on moving away from  $\bar{\Gamma}$ , it becomes a surface resonance whose lifetime decreases continuously as the separation increases. In a symmetric MTJ, the surface resonances on the two opposing surfaces couple and form bonding-antibonding pairs. As discussed by Wunnicke *et al.* [22], depending on the ratio of the bonding-antibonding splitting to the resonance linewidth, this coupling can give rise to resonant tunneling where the transmission is unity, independent of the barrier width (up to a critical barrier width). Surface roughness quenches this contribution and therefore reduces  $G_P^{min}$  in spite of a decreasing average barrier width. Even when the contribution from the resonant tunneling has become negligible,  $G_P^{min}$  continues to decrease as the surface state, and its contribution to the conductance, is destroyed by disorder<sup>2</sup>. At around 40% coverage, the decreasing barrier width asserts itself and the conductance begins to increase. Increasing  $x$  past 50% corresponds to decreasing roughness and a recovery of the surface states. Their *relative* influence, however, is less dominant for the substantially reduced barrier width. The corresponding TMR is shown in the inset. It is seen to vary over a huge range from in excess of 10<sup>4</sup>% for clean surfaces ( $x = 0\%$ ) to values comparable to experimentally observed ones. Hence, surface roughness alone can close the gap between the experimentally measured and much larger theoretically predicted TMR values [38, 39]. More technical details together with the deeper analysis of spin-dependent transport in Fe|vacuum|Fe MTJ can be found in the previous chapter.

We already noted that the (theoretically ill-defined) tunneling spin polarization in the Jullière model is frequently modelled by or interpreted in terms of bulk or local DOS [6]. The calculations shown in Fig. 4.2 were all carried out with the same Fe leads; a bulk Fe DOS in the Julliere model would predict a fixed TMR which is clearly not the case. We have used the local DOS in various combinations to calculate the TMR (not shown here) but none reproduces the “exact” results shown here nor its bias-dependence (see below).

### 4.3.1 Factorizing the conductance

In the previous chapter, we made the empirical observation that the total AP conductance was very well approximated by

$$G_{AP}^{\sigma} \approx \sqrt{G_P^{maj}} \sqrt{G_P^{min}} \equiv \frac{e^2}{h} \sqrt{\sum_{\mathbf{k}_{\parallel}} T_P^{maj}(\mathbf{k}_{\parallel})} \sqrt{\sum_{\mathbf{k}'_{\parallel}} T_P^{min}(\mathbf{k}'_{\parallel})}. \quad (4.12)$$

for  $10\% \lesssim x < 50\%$ . Note that the summation over  $\mathbf{k}_{\parallel}$  in (4.12) refers to Bloch vectors in the small 2D BZ corresponding to the  $10 \times 10$  lateral supercell used to model disorder and, even for a small amount of disorder, the  $\mathbf{k}_{\parallel}$ -dependence of  $T(\mathbf{k}_{\parallel})$

<sup>2</sup> $x=50\%$  corresponds to the most disordered surface



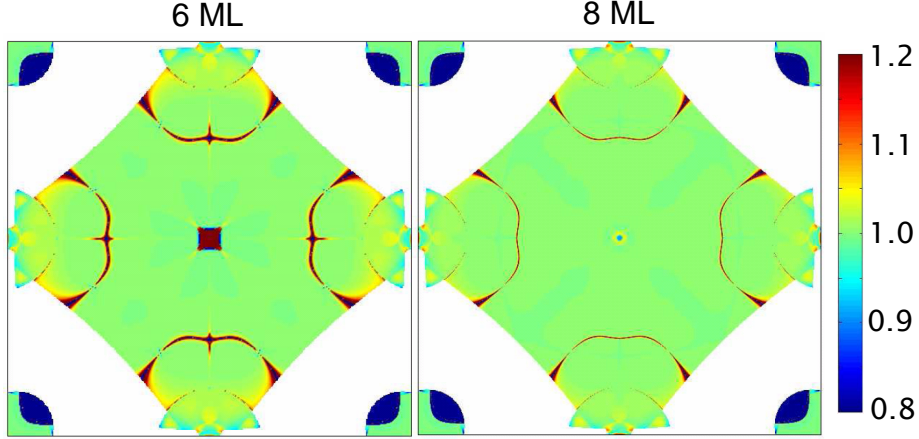


**Figure 4.3:** Test of the  $\mathbf{k}_{\parallel}$ -dependent factorization of the transmission. The ratio  $T_{AP}(\mathbf{k}_{\parallel})/\sqrt{T_P^{maj}(\mathbf{k}_{\parallel}) T_P^{min}(\mathbf{k}_{\parallel})}$  is plotted as a function of  $\mathbf{k}_{\parallel}$  in the 2D BZ for ideal Fe|vacuum|Fe MTJs with 6 MLs (left) and 8 MLs (right) of vacuum.

is small. This approximation for  $G_{AP}$  is plotted in Fig. 4.2 as a dashed line for the extended range of surface coverage shown there. It can be seen that the approximation also fails for  $90\% \lesssim x < 100\%$ . It would appear that, for a given barrier width, a minimum amount of roughness is required to destroy the transmission resonance.

By plotting the ratio of  $T_{AP}^{\sigma}(\mathbf{k}_{\parallel})$  and  $\sqrt{T_P^{maj}(\mathbf{k}_{\parallel}) T_P^{min}(\mathbf{k}_{\parallel})}$  as a function of  $\mathbf{k}_{\parallel}$  in the large 2D BZ corresponding to a  $1 \times 1$  unit cell in Fig. 4.3, we can visualize the resonant tunneling responsible for the breakdown of (4.12) for ideal interfaces,  $x = 0\%$  (right-hand panel) and  $x = 100\%$  (left-hand panel). The figure makes it clear that a  $\mathbf{k}_{\parallel}$ -dependent factorization works well in large areas of the 2D BZ but not for values of  $\mathbf{k}_{\parallel}$  where there are surface states and where transmission resonances occur. The linear scale used in the figure is somewhat misleading because in the relatively small areas of the 2D BZ where resonant tunneling occurs, the ratio deviates from unity by orders of magnitude making it difficult to gauge its quantitative impact from this representation.

Resonant tunneling (RT) appeared as anomalously large values of  $T_P^{min}(\mathbf{k}_{\parallel})$  in Fig. 3.6 and shows up as values less than unity in Fig. 4.3 which are colour-coded blue. However, not all points which appear blue in the figure correspond to resonant tunneling. In the previous chapter, points where RT occurred were identified in terms of their characteristic behaviour of having an amplitude which does not change as the barrier thickness is increased. For 8 MLs of vacuum, RT occurs close to the  $\bar{\Gamma}$  point at the centre of the 2D BZ (A) and at another point which we labelled (B) which is so sharp that it is not visible in Fig. 4.3. The other blue areas are interpreted as points where surface resonances give rise to enhanced but not resonant

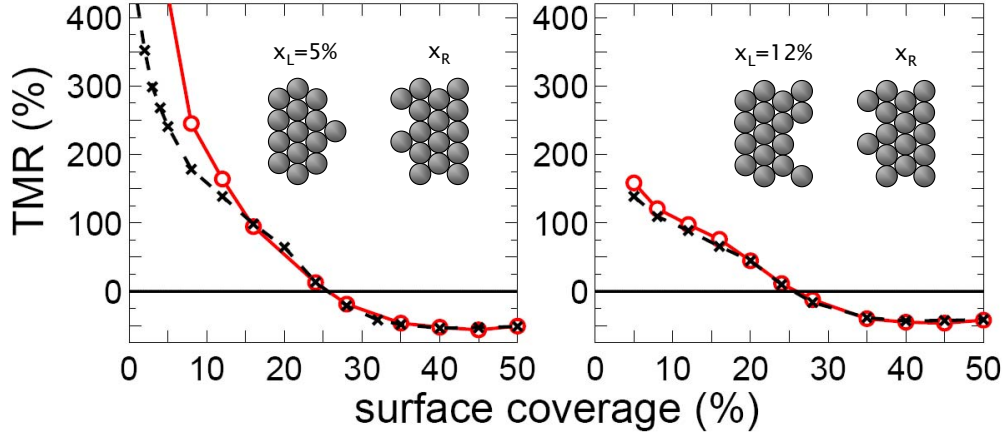


**Figure 4.4:** Configuration-averaged TMR of asymmetric Fe|vacuum|Fe MTJs with 8 MLs barrier width as a function of the surface coverage  $x_R$  for fixed coverages of the left surface,  $x_L = 5\%$  (left panel) and  $x_L = 12\%$  (right panel). The solid red lines are the results of explicit transport calculations while the dashed black lines are the values predicted using (4.14).

conduction. The features in the figure which are most conspicuous are the red-brown areas corresponding to antiresonant behaviour which become broader as the vacuum thickness is decreased.

Comparison of (4.12) with (4.2) shows that  $\sqrt{G_P^\sigma}$ , which can be measured for a symmetric MTJ, plays the role of  $\rho^\sigma$  in the TSP that can now be defined as

$$\mathcal{P} = \frac{\sqrt{G_P^{maj}} - \sqrt{G_P^{min}}}{\sqrt{G_P^{maj}} + \sqrt{G_P^{min}}}. \quad (4.13)$$

Using (4.12) it can be seen that the TMR of a symmetrical MTJ takes only nonnegative values, as illustrated in the inset in Fig. 4.2.

The factorization described by (4.12) can be generalized to asymmetric MTJs with interface roughness  $x_L$  on the left, and  $x_R$  on the right interfaces using the expression

$$G^{\sigma\sigma'}(x_L, x_R) = \sqrt{G_P^\sigma(x_L) G_P^{\sigma'}(x_R)} \quad (4.14)$$

where  $G_P^\sigma(x_i)$  is the  $\sigma$  component of the total conductance in the P configuration of a symmetric MTJ with surface roughness  $x_i$ . We already have  $G_P^\sigma(x)$  as a function of  $x$  for symmetric MTJs (Fig. 4.2). To test (4.14) we need to calculate  $G^{\sigma\sigma'}(x, y)$  for asymmetric Fe|vacuum|Fe MTJs and compare these “exact” results with those predicted by (4.14).

For two values of  $x_L$ , the TMR calculated explicitly and using (4.14) are shown as a function of  $x_R$  in Fig. 4.4. All results shown are configuration averaged. There

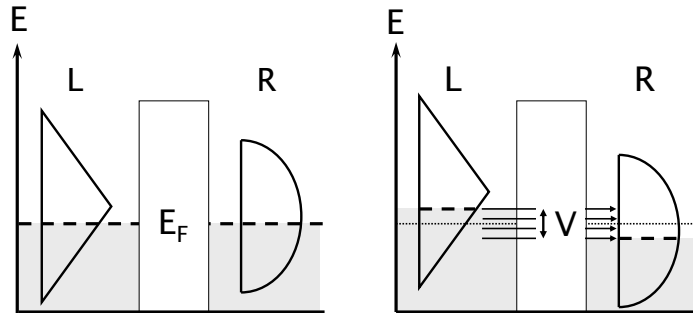


**Figure 4.5:** Schematic figure of an asymmetric tunnel junction in which the asymmetry is expressed in terms of triangular (left lead) and semi-oval (right lead) tunneling densities of states. In the left-hand panel, the junction is in equilibrium. In the right-hand panel, the potential of the left-hand lead is raised by  $V/2$ , that of the right-hand lead is lowered by the same amount. Current-carrying channels from occupied states in the left-hand lead into unoccupied states in the right-hand lead are indicated by right-pointing arrows.

is almost perfect agreement between the “predicted” and exact TMR values if the interface roughness is sufficient to destroy resonant tunneling in the calculations for the symmetric MTJ. The only serious discrepancy occurs when  $x_R \lesssim 10\%$  for  $x_L = 5\%$ . Unlike the symmetric case, the TMR can become negative for asymmetric junctions if the asymmetry is large enough for the TSP for left and right sides of the junction to have opposite signs, which is precisely what we see in Fig. 4.4. From Fig. 4.3 we see that the TSP is negative for  $x \lesssim 25\%$ . For the values of  $x_L = 5\%$  and  $12\%$  shown in Fig. 4.4, once  $x_R$  exceeds  $\sim 25\%$ , the TSP becomes positive and the TMR becomes negative. These conclusions are in qualitative agreement with experimental findings where negative TMR has been observed in asymmetric MTJs [10, 11, 40].

### 4.3.2 Factorization of conductance for finite bias

The sign of the TMR can also be changed by applying a finite bias [10–12, 40], posing the question of how to generalize Jullière’s model to this case. We first consider how to calculate conductances with an applied voltage and calculate the bias dependent TMR for an asymmetric MTJ before developing a factorization scheme analogous to that discussed in the previous section.

To calculate the bias dependence of the TMR, we apply a rigid shift of  $\pm V/2$  to the atomic sphere potentials in the left and right leads, respectively; see Fig. 4.5. The conductance as a function of applied bias  $V$  is obtained by integrating over the energy interval from  $\mu_R = E_F - V/2$  to  $\mu_L = E_F + V/2$ , where  $\mu_L$  and  $\mu_R$  are the

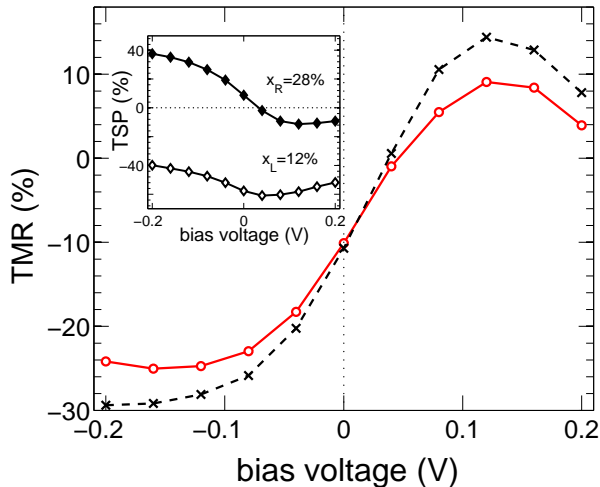


**Figure 4.6:** Configuration averaged (over 7 configurations) TMR as a function of bias voltage for an asymmetric MTJ with 8 MLs of vacuum and with  $x_L = 12\%$  and  $x_R = 28\%$ . Results of “exact” calculations are shown by the solid red line, those obtained with the factorization procedure discussed in the text are shown as a dashed black line.

chemical potentials of the left and right leads, respectively,

$$G^{\sigma\sigma'}(x_L, x_R, V) = \frac{1}{\mu_L - \mu_R} \int_{\mu_R}^{\mu_L} G^{\sigma\sigma'}(x_L, x_R, E) dE \quad (4.15)$$

and  $G^{\sigma\sigma'}(x_L, x_R, E)$  are the energy-dependent  $P$  or  $AP$  conductances for the asymmetric MTJ. Defining an average conductance in this way is common practice in phenomenological studies of tunneling transport [41, 42]. Neglecting any charge rearrangement on applying a bias might be expected to be a small effect when the tunnel currents are small. Explicit calculations for ideal MTJs showed good agreement between the results of a similar non-self-consistent procedure and self-consistent results for small bias voltages [43].

In our numerical scheme, the integration over energy is replaced by a finite sum, with an energy step  $\Delta E = 0.01$  eV for biases lower than 0.04 V, and  $\Delta E = 0.02$  eV for larger biases. Even for a modest bias of 0.2 V, this increases the computational cost by an order of magnitude. The results of calculations for an asymmetric junction with  $x_L = 12\%$  and  $x_R = 28\%$  and fixed vacuum thickness of 8 MLs are shown in Fig. 4.6 as a solid red line. The results are averaged over seven configurations of disorder. The TMR is negative at zero bias and changes sign to become positive when the positive bias exceeds about 0.05 V. A positive bias corresponds to  $\mu_L > \mu_R$  with electrons flowing from left to right (electrical current flowing in the opposite direction) and vice versa. This result is qualitatively similar to the experimental

findings in asymmetric Fe|GaAs|Fe(001) MTJs [40].

From the point of view of computational costs, finite-bias calculations for disordered systems are rather expensive. For a bias voltage of  $\pm 0.2 V$ , 11 calculations to perform the integral in (4.15) are required for each spin channel, for P and AP configurations: 44 calculations in total. Configuration-averaging over seven configurations increases this by a factor of seven. This yields a single data point in Fig. 4.6. Making the full curve required almost seven times as many calculations, 2100 in total, all of them with  $10 \times 10$  lateral supercells corresponding to a scattering region containing 2000 atoms (atomic spheres).

To reduce this cost, we extended the factorization discussed in the previous section to the finite bias case. The key element is to use energy-dependent conductances,  $G_P^\sigma(x, E)$ , calculated for *symmetric* MTJs to approximate the energy-dependent conductance  $G^{\sigma\sigma'}(x, y, E)$  for an *asymmetric* MTJ:

$$G^{\sigma\sigma'}(x_L, x_R, E) \approx \sqrt{G_P^\sigma(x_L, E - V/2) G_P^{\sigma'}(x_R, E + V/2)} \quad (4.16)$$

We first calculate  $G_P^\sigma(x, E)$  for two symmetric junctions with surface roughnesses  $x = x_L$  and  $x = x_R$  in the energy ranges  $[E_F - V, E_F]$  and  $[E_F, E_F + V]$ , respectively, with an energy step  $\Delta E$ . Then we use (4.16) to calculate the energy-dependent conductance for the asymmetric junction for both spin channels and P and AP configurations. Note that for an asymmetric MTJ, both spin channels need to be calculated for the AP configuration; both are obtained using the two spin components of the symmetric MTJs' P conductances. We then sum over the energies to calculate the bias dependent P and AP conductances. This procedure is repeated for as many different configurations of disorder as are needed, typically of order  $\sim 10$ . Finally, we calculate the TMR.

The results of this energy dependent factorization are shown as a dashed line in Fig. 4.6 and are seen to be in good agreement with the "exact" results. The remaining discrepancy can be attributed to the finite energy grid used and to the limited number of configurations (seven) used in the configuration averaging. The factorization can be used to explain the behavior of the TMR as a function of finite bias. In the inset in Fig. 4.6 we show the TSPs for left and right sides of the MTJ as a function of the bias voltage. From these results it can be seen that the sign change of the TMR corresponds to the change of sign with energy of the TSP of the right interface. These conclusions are in broad agreement with those reached for Fe|GaAs|Fe(001) MTJs on the basis of calculations which did not include disorder [44].

In view of the above, it is important to discuss the computational gain from the factorization procedure. Assume that we are interested in calculating the bias-dependent TMR for asymmetric MTJs with  $n$  different values of surface roughness. The total number of combinations (and therefore of exact calculations) would be  $n(n-1)/2$  per spin per P or AP orientation and per configuration. At the same time with the factorization procedure one needs to perform only  $n$  such calculations per spin per configuration. Moreover, the AP conductance is factorized into the components of P alone. Therefore, in the limit of large  $n$ , the number of calculations needed to be performed for calculating bias dependence of the TMR in the MTJs

with  $n$  different surface roughness is a factor  $n$  smaller. A similar consideration holds for the maximum value of bias,  $V$ . Summation on a discrete energy grid with energy step  $\Delta E$  requires  $N = V/\Delta E$  calculations for each value of  $V$ . If we require the conductances and TMR for  $N$  values of bias up to a maximum value  $V$ , of order  $N^2/2$  calculations must be performed. The factorization makes a linear scaling with  $N$  possible because energy points required for the integration over energy can be reused for different values of the bias.

## 4.4 Summary and Conclusions

The Jullière model assumes that a MTJ can be separated into left and right independent parts that are characterized by some TDOS. The total conductance in each spin channel through the junction is then factorized in terms of TDOS for left and right parts. Polarization of the TDOS (TSP) can be measured experimentally and the validity of the Jullière model has been demonstrated from numerous experiments [7–9]. Despite plenty of experimental results, the physical basis of the TDOS is unclear.

Spin-dependent transport of electrons in a MTJ has been investigated in a number of theoretical studies. From *ab initio* calculations for ideal material-specific MTJs, it has been demonstrated that tunnel transmission does not factorize when resonant tunneling occurs [21]. The transmission could be factorized in a single-band tight binding model if the complete tunnel barrier was sufficiently disordered [16, 17]. A formalism for handling disorder based upon Bardeen’s transfer-Hamiltonian method was recently developed [18] but has not been used to treat MTJs containing transition metals or realistic atomic structures.

In the present work, we have used an *ab initio* approach to study transport in Fe|vacuum|Fe MTJs taking interface roughness into account. Interface disorder is important because it quenches resonant tunneling [14] and by including it in this chapter, we could recover the form of the Jullière model. Our factorization makes it possible to predict the TMR for asymmetric MTJs with different disorder  $x_L$  and  $x_R$  on the left and right interfaces using only results for symmetrical junctions  $x_L \equiv x_R$ . Negative TMR has been shown to occur if the difference between  $x_L$  and  $x_R$  increases. Similarly to the Jullière model, the negative sign has been attributed to opposite signs of TSP for left and right parts of junction. The factorization procedure could be confirmed experimentally by performing a study of symmetric and asymmetric MTJs but would require some means of characterizing the disorder quantitatively. The factorization approach was extended to the energy dependent case and shown to correctly reproduce bias-dependent TMR. Change of the sign of TMR as a function of bias has been shown to correlate again with the change of sign of the TSP.

## Bibliography

- [1] S. Yuasa and D. D. Djayaprawira, J. Phys. D: Appl. Phys. **40**, R337 (2007).
- [2] M. Julliere, Phys. Lett. A **54**, 225 (1975).

- [3] N. F. Mott, Proc. R. Soc. London, Ser. A **153**, 699 (1936).
- [4] N. F. Mott, Proc. R. Soc. London, Ser. A **156**, 368 (1936).
- [5] P. M. Tedrow and R. Meservey, Phys. Rev. B **7**, 318 (1973).
- [6] R. Meservey and P. M. Tedrow, Phys. Rep. **238**, 173 (1994).
- [7] J. S. Moodera, L. R. Kinder, T. M. Wong, and R. Meservey, Phys. Rev. Lett. **74**, 3273 (1995).
- [8] P. LeClair, H. J. M. Swagten, J. T. Kohlhepp, R. J. M. van de Veerdonk, and W. J. M. de Jonge, Phys. Rev. Lett. **84**, 2933 (2000).
- [9] S. S. P. Parkin *et al.*, Nature Materials **3**, 862 (2004).
- [10] J. M. De Teresa *et al.*, Science **286**, 507 (1999).
- [11] I. J. V. Marún, F. M. Postma, J. C. Lodder, and R. Jansen, Phys. Rev. B **76**, 064426 (2007).
- [12] M. Sharma, S. X. Wang, and J. H. Nickel, Phys. Rev. Lett. **82**, 616 (1999).
- [13] J. M. De Teresa *et al.*, Phys. Rev. Lett. **99**, 4288 (2002).
- [14] P. X. Xu *et al.*, Phys. Rev. B **73**, 180402(R) (2006).
- [15] J. C. Slonczewski, Phys. Rev. B **39**, 6995 (1989).
- [16] E. Y. Tsymbal and D. G. Pettifor, Phys. Rev. B **58**, 432 (1998).
- [17] J. Mathon and A. Umerski, Phys. Rev. B **60**, 1117 (1999).
- [18] J. C. Slonczewski, Phys. Rev. B **71**, 024411 (2005).
- [19] J. M. MacLaren, X.-G. Zhang, and W. H. Butler, Phys. Rev. B **56**, 11827 (1997).
- [20] K. D. Belashchenko *et al.*, Phys. Rev. B **69**, 174408 (2004).
- [21] K. D. Belashchenko, E. Y. Tsymbal, I. I. Oleynik, and M. van Schilfgaarde, Phys. Rev. B **71**, 224422 (2005).
- [22] O. Wunnicke *et al.*, Phys. Rev. B **65**, 064425 (2002).
- [23] M. Zwierzycki, Y. Tserkovnyak, P. J. Kelly, A. Brataas, and G. E. W. Bauer, Phys. Rev. B **71**, 064420 (2005).
- [24] S. Yuasa, T. Nagahama, A. Fukushima, Y. Suzuki, and K. Ando, Nature Materials **3**, 868 (2004).
- [25] K. Xia, M. Zwierzycki, M. Talanana, P. J. Kelly, and G. E. W. Bauer, Phys. Rev. B **73**, 064420 (2006).

- [26] M. Zwierzycki *et al.*, *phys. stat. sol. B* **245**, 623 (2008).
- [27] I. Turek, V. Drchal, J. Kudrnovský, M. Šob, and P. Weinberger, *Electronic Structure of Disordered Alloys, Surfaces and Interfaces* (Kluwer, Boston-London-Dordrecht, 1997).
- [28] O. K. Andersen, Z. Pawłowska, and O. Jepsen, *Phys. Rev. B* **34**, 5253 (1986).
- [29] O. K. Andersen and O. Jepsen, *Phys. Rev. Lett.* **53**, 2571 (1984).
- [30] T. Ando, *Phys. Rev. B* **44**, 8017 (1991).
- [31] K. Xia *et al.*, *Phys. Rev. B* **63**, 064407 (2001).
- [32] P. Soven, *Phys. Rev.* **156**, 809 (1967).
- [33] J. A. Strosio, D. T. Pierce, A. Davies, R. J. Celotta, and M. Weinert, *Phys. Rev. Lett.* **75**, 2960 (1995).
- [34] S. F. Alvarado, *Phys. Rev. Lett.* **75**, 513 (1995).
- [35] S. N. Okuno, T. Kishi, and K. Tanaka, *Phys. Rev. Lett.* **88**, 066803 (2002).
- [36] H. F. Ding, W. Wulfhekel, J. Henk, P. Bruno, and J. Kirschner, *Phys. Rev. Lett.* **90**, 116603 (2003).
- [37] M. M. J. Bischoff, T. K. Yamada, C. M. Fang, R. A. de Groot, and H. van Kempen, *Phys. Rev. B* **68**, 045422 (2003).
- [38] W. H. Butler, X.-G. Zhang, T. C. Schulthess, and J. M. MacLaren, *Phys. Rev. B* **63**, 054416 (2001).
- [39] J. Mathon and A. Umerski, *Phys. Rev. B* **63**, 220403(R) (2001).
- [40] J. Moser *et al.*, *Appl. Phys. Lett.* **89**, 162106 (2006).
- [41] S. Datta, *Electronic Transport in Mesoscopic Systems* (Cambridge University Press, Cambridge, 1995).
- [42] C. B. Duke, *Tunneling in Solids*, supplement 10 of, in *Solid State Physics*, edited by F. Seitz and D. Turnbull, Academic Press, New York, 1969.
- [43] C. Zhang *et al.*, *Phys. Rev. B* **69**, 134406 (2004).
- [44] A. N. Chantis *et al.*, *Phys. Rev. Lett.* **99**, 196603 (2007).



## Chapter 5

# Graphene and Graphite as Perfect Spin Filters

*Based upon the observations (i) that their in-plane lattice constants match almost perfectly and (ii) that their electronic structures overlap in reciprocal space for one spin direction only, perfect spin filtering for interfaces between graphite and (111) fcc or (0001) hcp Ni or Co is predicted. The spin filtering is quite insensitive to lattice mismatch, roughness and disorder. The formation of a chemical bond between graphite and the open d-shell transition metals that might complicate or even prevent spin injection into a single graphene sheet can be simply prevented by dusting Ni or Co with one or a few monolayers of Cu while still preserving the ideal spin injection property.*

### 5.1 Introduction

We recently predicted a perfect spin filtering effect for ultra-thin films of graphite sandwiched between two ferromagnetic leads [1]. This prediction emerged from the interface between two rapidly developing branches of condensed matter physics: magnetoelectronics and graphene electronics [2, 3]. Magnetoelectronics exploits the additional degree of freedom presented by the intrinsic spin and associated magnetic moment of electrons while graphene electronics is based upon the unique electronic properties of two-dimensional graphene sheets. Based on the giant magnetoresistance effect discovered twenty years ago [4, 5], magnetoelectronics was rapidly applied to making improved read head sensors for hard disk recording and is a promising technology for a new type of magnetic storage device, a magnetic random access memory. The giant magnetoresistance (GMR) effect is based on the spin dependence of the transmission through interfaces between normal and ferromagnetic metals (FM). The effect is largest when the current passes through each interface in a current-perpendicular-to-plane (CPP) measuring configuration but the absolute resistance

of metallic junctions is too small for practical applications and the current-in-plane (CIP) configuration with a much smaller MR is used in practice. Replacing the non-magnetic metal spacer with a semiconductor [6] or insulator (I) [7, 8] results in spin-dependent tunneling and much larger resistances are obtained with FM|I|FM magnetic tunnel junctions (MTJs). Substantial progress has been made in increasing the MR effect by improving experimental techniques, and by replacing the amorphous  $\text{Al}_2\text{O}_3$  insulator with crystalline MgO [9, 10]. Though there is a relatively large lattice mismatch of 3.8% between Fe and MgO, the tunneling magnetoresistance (TMR) in Fe|MgO|Fe junctions has been reported to reach values as high as 180% at room temperature [11]. Low temperature values as high as 1010% have been reported for FeCoB|MgO|FeCoB MTJs [12, 13]. The sensitivity of TMR (and spin injection) to details of interface structure [14, 15] makes it difficult to close the quantitative gap between theory and experiment so it is important for our understanding of TMR to be able to prepare interfaces where disorder does not dominate the spin filtering properties. This remains a challenge due to the high reactivity of the open-shell transition metal (TM) ferromagnets Fe, Co, and Ni with typical semiconductors and insulators.

With this in mind, we wish to draw attention to a quite different material system in which a thin graphite film is sandwiched between two ferromagnetic leads. Graphite is the ground state of carbon and as one of the most important elemental materials, its electronic structure has been studied in considerable detail. It consists of weakly interacting sheets of strongly bonded carbon atoms. Because of the weak interaction between these “graphene” or “monolayer graphite” sheets, the electronic structure of graphite is usually discussed in two steps: first, in terms of the electronic structure of a single  $sp^2$ -bonded sheet, followed by consideration of the interaction between sheets [16–18]. From these early, and many subsequent studies, it is known that graphene is a “zero-gap semiconductor” or a semimetal in which the Fermi surface is a point at the “K” point in two-dimensional reciprocal space. The physical properties associated with this peculiar electronic structure have been studied theoretically in considerable detail, in particular in the context of carbon nanotubes which can be considered as rolled-up graphene sheets [19]. With the very recent discovery

	Graphene	Co	Ni	Cu
$a_{\text{fcc}}^{\text{expt}}$ (Å) [20]		3.544	3.524	3.615
$a_{\text{hex}}^{\text{expt}}$ (Å)	2.46	2.506	2.492	2.556
$a_{\text{hex}}^{\text{LDA}}$ (Å)	2.45	2.42	2.42	2.49
$d_0$ (Å)		2.04	2.03	3.18

**Table 5.1:** Lattice constants of Co, Ni, Cu, and graphene,  $a_{\text{hex}} \equiv a_{\text{fcc}}/\sqrt{2}$ . Equilibrium separation  $d_0$  for a single graphene sheet on top of the graphite(0001), Co, Ni or Cu(111) surfaces as calculated within the framework of the DFT-LSDA using the in-plane lattice constant  $a_{\text{hex}} = 2.46$  Å.

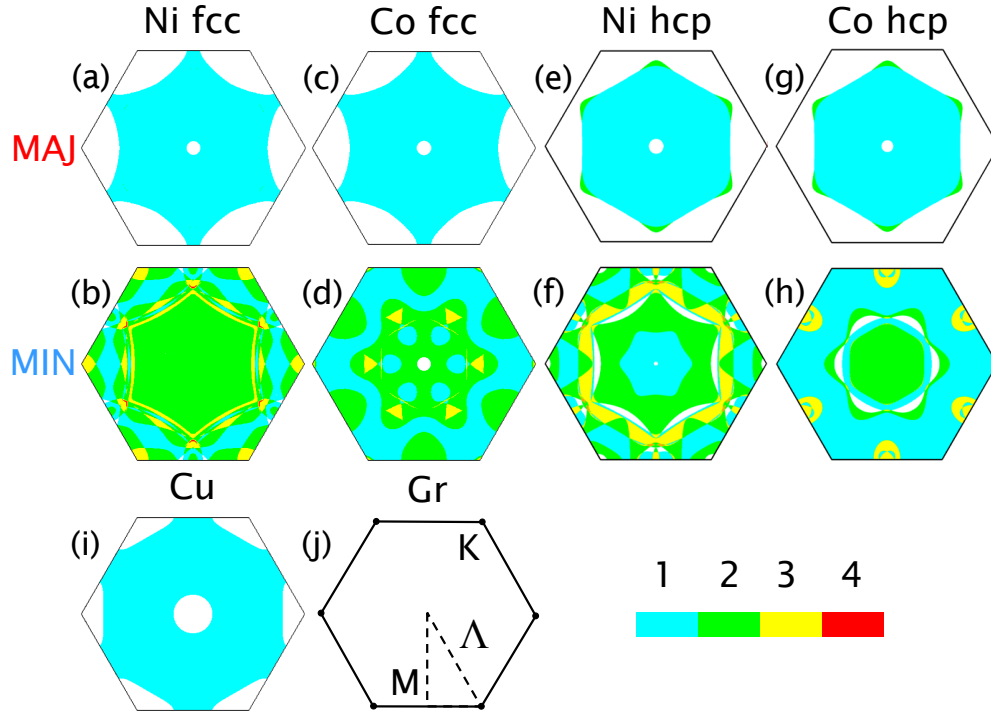


**Figure 5.1:** Fcc Fermi surface (FS) projections onto a plane perpendicular to the (111) direction: Ni fcc majority (a) and minority (b) spins; Co fcc majority (c) and minority (d) spins; Ni hcp majority (e) and minority (f) spins; Co hcp majority (g) and minority (h) spins; Cu fcc (i). For graphene and graphite, surfaces of constant energy are centred on the K point (j). The number of FS sheets is given by the colour bar.

and development of an exceptionally simple procedure for preparing single and multiple graphene sheets, micromechanical cleavage [21], it has become possible to probe these predictions experimentally. Single sheets of graphene turn out to have a very high mobility [22] that manifests itself in a variety of spectacular transport phenomena such as a minimum conductivity, anomalous quantum Hall effect (QHE) [23, 24], bipolar supercurrent [25] and room-temperature QHE [26]. Spin injection into graphene using ferromagnetic electrodes has already been realized [27, 28]. The low atomic number of carbon implying weak spin-orbit interaction should translate into very long intrinsic spin-flip scattering lengths, a very desirable property in the field of spin electronics or “spintronics”, which aims to combine traditional semiconductor-based electronics with control over spin degrees of freedom. However, the room temperature MR effect of  $\sim 10\%$  observed in lateral, current-in-plane (CIP) graphene-based devices with soft permalloy leads is still rather small [27].

Instead of a CIP geometry, we consider a CPP TM|Gr|TM junction, where TM is a close-packed surface of fcc or hcp Ni or Co and Gr is graphite (or  $n$  sheets of graphene, Gr $_n$ ). We argue that such a junction should work as a perfect spin filter. The essence of the argument is given in Table 5.1 and Fig. 5.1. According to Table 5.1, the surface lattice constants of (111) Ni, Co and Cu match the in-plane lattice constants of graphene and graphite almost perfectly. The lattice mismatch of 1.3% at the Ni(111)|Gr interface is, in fact, one of the smallest for the magnetic junctions that have been studied so far. This small lattice mismatch suggests that the TM|Gr|TM junction might be realized experimentally, for example, using the chemical vapor deposition technique [29–31]. Assuming perfect lattice matching at the TM|Gr interface, it is possible to directly compare the Fermi surface (FS) projection of graphite with the FS projections of Cu fcc (111), Ni and Co in both fcc (111) and hcp (0001) directions, see Fig. 5.1.

The Fermi surface of graphene is a point at the high-symmetry K point in reciprocal space. The Fermi surfaces of graphite and doped graphene are centred on this point and close to it. Figure 5.1 shows that there are no majority spin states for Ni and Co around the K point whereas minority spin states exist (almost) everywhere in the surface BZ. Only the minority spin channel should then contribute to transmission from a close-packed TM surface into graphite. In a TM|Gr|TM junction, electrons in other regions of reciprocal space on the left electrode will have to tunnel through graphite to reach the right electrode. If the graphite film is taken thick enough to suppress tunneling, majority spin conductance will be quenched and only minority spin conductance through the graphite will survive *i.e.* perfect spin filtering will occur.

In this chapter, we wish to study quantitatively the effectiveness of this spin filtering: how it depends on the thickness of the graphite film, the geometry of the clean metal-graphite interface, interface roughness and disorder, and lattice mismatch. While we will be mainly concerned with the CPP geometry, we will also comment on the applicability of some of our conclusions to the CIP geometry. The chapter is organized as follows. In Sec. 5.2 a brief description of the computational method together with the most important details of the calculations is given. In Sec. 5.3 the electronic and structural properties of bulk materials like Ni, Co, graphite and graphene, that are used for constructing TM|Gr $_n$ |TM junctions, using the tight-binding linear muffin tin orbitals (TB-MTO) within the atomic-sphere approximation (ASA) are studied. These results are benchmarked against plane-wave pseudopotential calculations. Section 5.4 contains the results of spin-dependent electron transport calculations for specular interfaces (ideal junction) as well as for junctions with interface roughness and alloy disorder. Finally, the conclusions are drawn in Sec. 5.5.

## 5.2 Computational Method

The starting point for our study is an atomic structure calculated by minimizing the total energy within the local spin density approximation (LSDA) of density functional

theory (DFT). This was done using a plane-wave pseudopotential (PWP) method based upon projector augmented wave (PAW) pseudopotentials [32] as implemented in the VASP program [33–35]. The interaction between graphite and the TM surface is modelled using a repeated slab geometry of six metal layers with a graphene sheet on top and a vacuum thickness of  $\sim 12$  Å. A dipole correction is applied to avoid interactions between periodic images of the slab [36]. The surface Brillouin zone (SBZ) was sampled with a  $36 \times 36$   $\mathbf{k}$ -point grid and the SBZ integrals carried out with the tetrahedron integration scheme. A plane wave kinetic energy cutoff of 400 eV was used. The plane-wave pseudopotential method is used to calculate energy band structures, charge transfer, binding energies and work functions for single TM|Gr interfaces [1, 37]. The equilibrium distances  $d_0$  between the graphene sheet and the TM surfaces are summarized in Table 5.1.

The equilibrium geometries are used as input for a self-consistent TB-LMTO [38] calculation for the TM|Gr<sub>*n*</sub>|TM junction. The Kohn-Sham potentials are used to calculate spin-dependent transmission probabilities through the TM|Gr<sub>*n*</sub>|TM junction using the wave-function matching scheme [39–41]. To do this, the junction is divided into three parts: the scattering region sandwiched between semi-infinite left and right leads, all of which are split into layers that are periodic in the lateral direction. The semi-infinite leads are assumed to be ideal periodic crystals in which the electron states (modes) are wave functions with Bloch translational symmetry. According to the Landauer-Büttiker formalism of transport, the conductance for minority and majority spin channels can be calculated by summing up all the probabilities for transmitting an electron from the electron modes in the left lead through the junction into electron modes in the right leads [41–43].

We can study the effect of various types of disorder on the transmission using the same formalism and computer codes by modelling the disorder within large lateral supercells [39, 41] and averaging over many configurations of disorder generated by choosing positions of impurity atoms or imperfections randomly. Three types of disorder are studied: interface roughness, interface alloying and lattice mismatch. In the first two cases, averaging is performed over a minimum of ten configurations of disorder. To model interface roughness, some surface atoms are removed (replaced by empty spheres with nuclear charges that are zero in the ASA) and the ASA potentials are calculated self-consistently using a layer version [44] of the coherent potential approximation (CPA) [45]. The effect of interface alloying which might occur if deposition of a thin layer of copper on Ni or Co (“dusting”) leads to intermixing is modelled in a similar fashion. Thirdly, the small lattice mismatch between graphite and TM is modelled by “cutting and pasting” AS potentials from self-consistent calculations for TM|Gr<sub>*n*</sub>|TM junctions with two different in-plane lattice constants. The two systems are then combined using a supercell of the size determined by the lattice mismatch. The lateral BZ of the supercell is sampled with a  $24 \times 24$   $\mathbf{k}$ -point grid for the self-consistent TB-ASA-LMTO calculations. To converge the conductance, denser grids containing  $800 \times 800$ ,  $20 \times 20$  and  $8 \times 8$   $\mathbf{k}$ -points are used for  $1 \times 1$  (ideal junction),  $5 \times 5$  and  $20 \times 20$  supercells, respectively.

### 5.3 Geometry and electronic structure of TM|Gr<sub>n</sub>|TM

In this section we describe in more detail how the electronic structure of TM|Gr<sub>n</sub>|TM junctions for TM=Cu, Ni or Co is calculated. These close-packed metals can be grown with ABC stacking in the (111) direction (fcc), or with AB stacking in the (0001) direction (hcp). We neglect the small lattice mismatch of 1.3%, 1.9% and 3.9% for the Ni|Gr, Co|Gr, and Cu|Gr interfaces, respectively, and assume the junction in-plane lattice constant to be equal to that of graphite,  $a_{\text{Gr}} = 2.46 \text{ \AA}$ . In the atomic spheres approximation (ASA), the atomic sphere radii of Ni, Co and Cu are then  $r_{\text{TM}} = 2.574 \text{ a.u.}$  The ASA works well for transition metals like Co, Ni or Cu which have close-packed structures. For materials like graphite which has a very open structure with an in-plane lattice constant  $a_{\text{Gr}} = 2.46 \text{ \AA}$ , and an out-of-plane lattice constant  $c_{\text{Gr}} = 6.7 \text{ \AA}$ , the unmodified ASA is not sufficient. Fortunately, a reasonable description of the crystal potential can be obtained by packing the interstitial space with empty spheres [47]. This procedure should satisfy the following criteria: (i) the total volume of all atomic spheres has to be equal to the volume of the entire system (space filling), and the (ii) overlap between the atomic spheres should be as small as possible.

#### 5.3.1 Graphite and graphene

To see how this procedure works in practice, we benchmark the TB-MTO-ASA band structure of graphite against the “exact” band structure calculated with the PWP method. To preserve the space group symmetry which is  $D_{6h}^4$  (P6<sub>3</sub>/mmc) for graphite [46], the positions of the atomic spheres are chosen at Wyckoff positions. There are

Model	Atom	Wyckoff position	position parameters	radius (a.u.)
I	C <sub>1</sub>	2b		1.556
	C <sub>2</sub>	2c		1.556
	E <sub>1</sub>	2a		1.454
	E <sub>2</sub>	2d		1.61
	E <sub>3</sub>	4f	z=0.5	1.454
	E <sub>4</sub>	24l	x=1/3, y=0, z=0.376	1.454
	II	C <sub>1</sub>	2b	
C <sub>2</sub>		2c		1.56
E		4f	z=0.398	2.18

**Table 5.2:** Atomic parameters including five types of empty spheres: E, E<sub>1</sub>, E<sub>2</sub>, E<sub>3</sub>, E<sub>4</sub>, (with nuclear charge Z=0); atomic positions according to Wyckoff notations of space group  $D_{6h}^4$  (P6<sub>3</sub>/mmc) Ref.[46]; position parameters and atomic sphere radii.

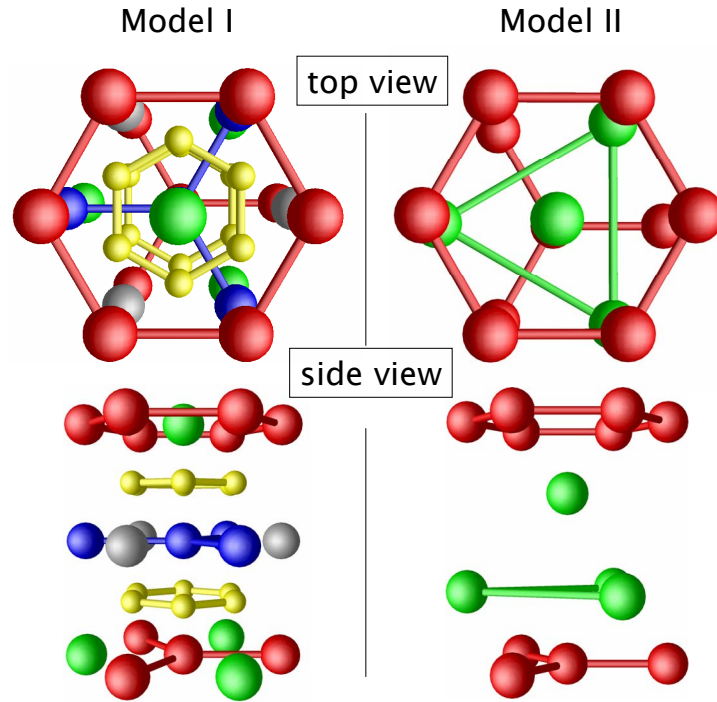


**Figure 5.2:** Top and side perspective views (top and bottom panels) of graphite where the potential is represented in the atomic spheres approximation using additional, empty atomic spheres. Model I (left) contains 32 empty spheres in a unit cell containing 4 carbon atoms (red spheres). Model II (right), contains just 4 empty spheres. For model I, gray, green, blue and yellow spheres display the positions of  $E_1$ ,  $E_2$ ,  $E_3$  and  $E_4$  empty spheres respectively. For model II, there is just one type of empty sphere (green).

twelve different Wyckoff positions consistent with  $D_{6h}^4$  symmetry, so the best choice of empty spheres is not immediately obvious. We construct two models that describe the band structure close to the Fermi energy well compared to the PWP results; this is what is most relevant for studying transport in the linear response regime. Model I with 32 empty spheres per unit cell and model II with only 4 empty spheres per unit cell both preserve the symmetry of graphite within the ASA. The crystal structures of graphite packed with empty spheres according to these two models is shown schematically in Fig. 5.2<sup>1</sup>. The Wyckoff labels, atomic sphere coordinates and radii are given in Table 5.2. Figure 5.3 shows the band structure of graphite obtained with the TB-MTO-ASA for models I and II compared to the “exact” PWP band structure. Both models are seen to describe the graphite  $\pi$  bands around the

<sup>1</sup>note that not all the empty spheres in a unit cell are shown in Fig. 5.2

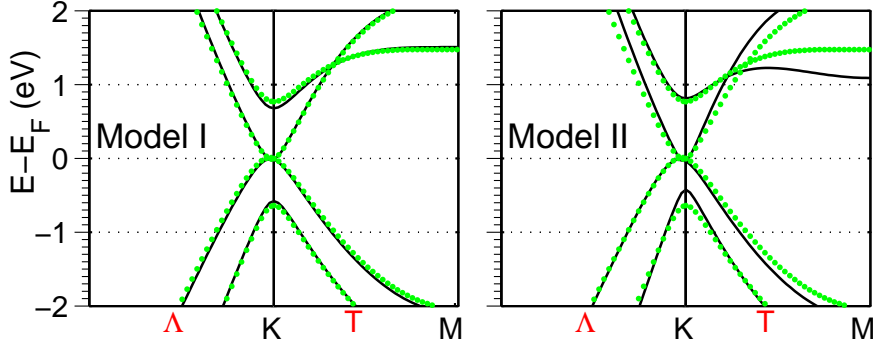


**Figure 5.3:** Band structure of graphite for model I (on the left), and model II (on the right). Green dots and black lines correspond to band structures calculated using the PWP and TB-MTO-ASA methods, respectively.

Fermi energy very well. Model I provides a very good description of the bands within  $\pm 2$  eV of the Fermi energy, while the smaller basis model II is quite good within  $\pm 1$  eV. At the cost of including many more empty spheres, model I provides a better description of the crystal potential between the graphene planes than model II. For this reason we use model I to study the transport properties of ideal junctions, junctions with interface roughness and alloy disorder. To be able to handle the large  $20 \times 20$  lateral supercells needed to model lattice mismatch of 5% at the TM|Gr interface, we use model II.

### 5.3.2 Graphene on Ni(111) substrate

The next step is to put a monolayer of graphene (graphene) on top of the Ni(111) substrate at a distance  $d_0$  from the metal surface. From our studies of the energetics of graphene on TM(111), we found [1, 37] that the lowest energy configuration (with  $3m$  symmetry) for TM=Ni or Co corresponds to an “AC” configuration in which one carbon atom is positioned on top of a surface TM atom (an “A” site) while the second carbon atom is situated above a third layer TM atom (a “C” site), where A and C refer to the ABC stacking of fcc close-packed planes, see Fig. 5.5. This is in agreement with another recent first-principles calculations [48] as well as with experiments [30, 31] for graphene on the Ni(111) surface. The electronic structure of a single graphene sheet will depend on  $d_0$  and the details of such graphene-metallic substrate contacts can be expected to play an important role in current-in-plane (CIP) devices [27, 28]. For the less strongly bound BC configuration of Gr on Ni, the equilibrium separation is rather large  $d_0 \sim 3.3$  Å and the characteristic band structure of an isolated graphene



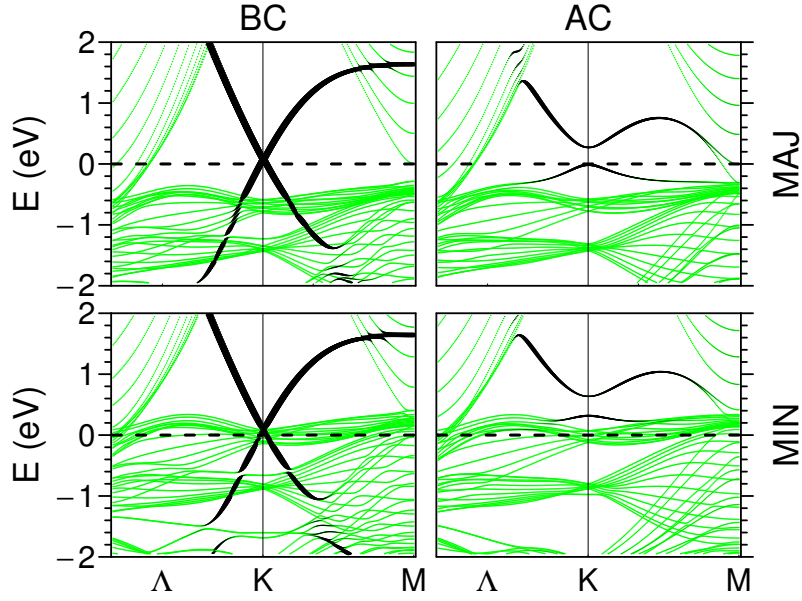


**Figure 5.4:** The results of PWP calculations of majority (top panels) and minority (bottom panels) spin band structures (green) of a single graphene layer adsorbed upon (both sides of) a 13 layer (111) Ni slab for a BC configuration with  $d_0 = 3.3$  Å, and an AC configuration with  $d_0 = 2.0$  Å. The bands replotted in black using the carbon  $p_z$  character as a weighting factor are superimposed. The Fermi energy is indicated by the horizontal dashed line.

sheet is clearly recognizable; see Fig. 5.4. For the lowest energy AC configuration, the interaction between the graphene sheet and Ni surface is much stronger, a gap is opened in the graphene derived  $p_z$  bands and there are no graphene states at the K-point in reciprocal space at the Fermi energy for the minority spin channel. This may prevent efficient spin injection into graphene in lateral, CIP devices [27].

### 5.3.3 Ni|Gr<sub>n</sub>|Ni(111) junction

The transmission of electrons through a TM|Gr<sub>n</sub>|TM junction will obviously depend on the geometry of the metal-graphite contacts. Rather than carrying out a total energy minimization explicitly for every different value of  $n$ , we assume that the weak interaction between graphene sheets will not influence the stronger TM|Gr interaction and construct the junction using the “AC” configuration and the equilibrium separation  $d_0 = 2.03$  Å for each interface, as shown in Fig. 5.5. The interstitial space at the TM|Gr interfaces is filled with empty spheres using a procedure analogous to that described for bulk graphite [49].

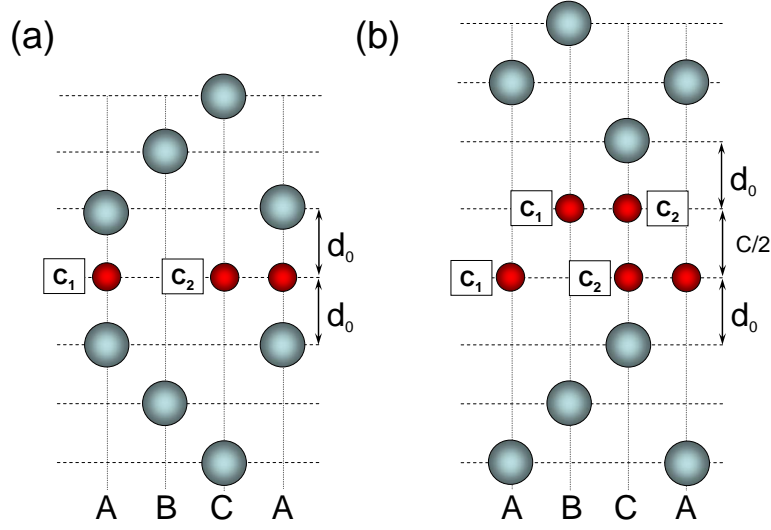


**Figure 5.5:** “AC” model of TM|Gr<sub>n</sub>|TM structure for (a) even and (b) odd number of graphene sheets. Carbon atoms are represented by small red spheres, TM atoms by larger gray spheres. The configuration shown in (a) is a  $c_1c_1$  configuration with the carbon atom labelled  $c_1$  above an “A” site surface layer TM atom of the top and the bottom electrodes. The other carbon atom,  $c_2$ , is above a third layer TM atom on a “C” site. An equivalent  $c_2c_2$  configuration in which the  $c_2$  atoms are on top of TM atoms can be realized by rotating the top and bottom electrodes by  $180^\circ$  about a vertical axis through the second layer “B” sites; this effectively interchanges  $c_1$  and  $c_2$ . Two other equivalent configurations  $c_1c_2$  and  $c_2c_1$  can be realized in an analogous fashion by rotating either the top or the bottom electrode through  $180^\circ$ . For two sheets of graphene stacked as in graphite, a  $c_2c_2$  configuration is sketched in (b). Interlayer distance is indicated as  $d_0$  and  $c/2$  is the distance separating two neighbouring graphene sheets.

Because the two carbon atoms  $c_1$  and  $c_2$  in the graphene unit cell are equivalent, either of them can be positioned above a surface Ni atom on an A site with the other on the C site in an “AC” configuration, without changing the total energy. Since this can be done for each TM|Gr interface separately, four different configurations of the TM|Gr|TM junction can be constructed by rotating one or both electrodes through  $180^\circ$  about a vertical axis through the second layer B sites which interchanges electrode A and C sites in Fig. 5.5. We label these four different configurations  $c_1c_1$ ,  $c_1c_2$ ,  $c_2c_1$  and  $c_2c_2$  in terms of the carbon atoms which are bonded to A site TM atoms. For more than one graphene sheet, the second sheet breaks the symmetry between the  $c_1$  and  $c_2$  atoms. While we have not checked this explicitly, we expect the corresponding energy difference to be small and will neglect it.

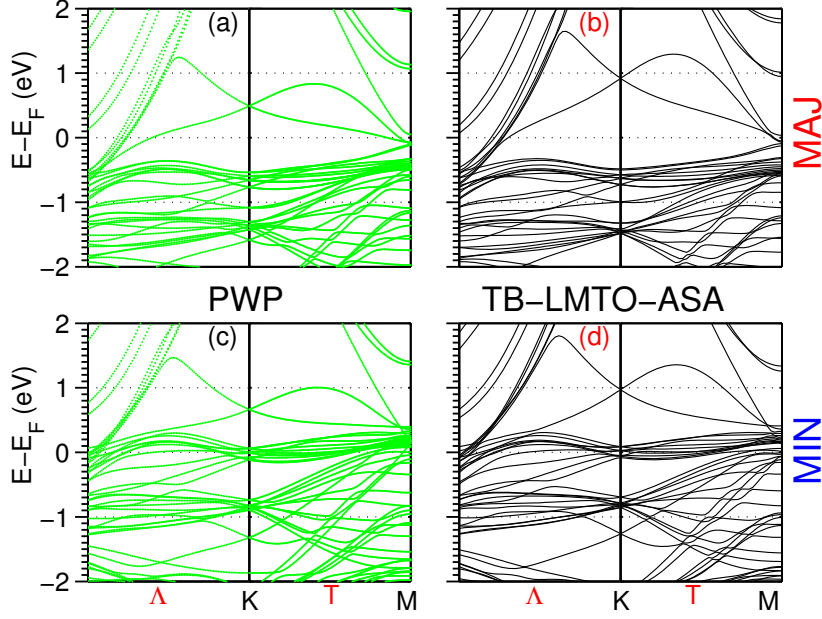


**Figure 5.6:** Lateral band structures of the Ni|Gr|Ni ideal junction with a monolayer of graphite and 6 monolayers of (111) Ni that on both sides in case of “AC” model  $c_1c_2$  configuration for majority (top panels) and minority (bottom panels) spin channels. The PWP calculations are shown on the left (green dotted lines) and the TB-LMTO-ASA results are on the right (black solid lines).

In Figure 5.4 we saw that the graphene  $\pi$  states interacted strongly with the nickel surface in the minimum energy “AC” configuration. The interaction with the metal substrate made the  $c_1$  and  $c_2$  carbon atoms inequivalent and led to the opening of an energy gap in the graphene  $\pi$  bands. Having constructed an interface geometry, we can examine the band structure of the Ni|graphene|Ni (111) junction as a function of  $\mathbf{k}_{\parallel}$ , the two dimensional Bloch vector. This is shown in Fig. 5.6 for a single sheet of graphene sandwiched between two slabs of Ni each of which is 6 monolayers thick. The bands on the left-hand side were calculated using the plane-wave pseudopotential (PWP) method and those on the right with the TB-LMTO-ASA. Assuming the PWP as a benchmark, we see that the Ni-related bands are described well by the TB-LMTO-ASA - as might be expected since the ASA is known to work well for close-packed solids. The second thing we see is that there is no gap in the graphene  $\pi$  bands. This is because the  $c_1c_2$  configuration used in the calculation has inversion symmetry and the symmetry between the two carbon atoms is restored; see Fig. 5.5(a). The third point to be made is that the charge transfer from graphene (work function: 4.5

eV) to Ni (work function: 5.5 eV) and strong chemisorption leads to the formation of a potential step at the interface and a significant shift of the graphene  $\pi$  bands with respect to the Fermi level which is pinned at that of bulk Ni. We find similar results for Co|Gr|Co(111) and Co|Gr|Co(0001) junctions. There is a difference between the position of the graphene  $\pi$ -derived bands, most noticeably at the K point, in the PWP and TB-LMTO-ASA band structures shown in Fig. 5.6 for both spin channels. It appears that the interface dipole is not adequately described by the ASA. Since from the point of view of describing transmission of electrons through this junction, the electronic band structure is the most important measure of the quality of our basis, description of the potential etc, this discrepancy is disturbing and will certainly have quantitative consequences. However, our most important conclusions will be qualitative and will not depend on this aspect of the electronic structure.

## 5.4 Electron transport through a FM|Gr<sub>n</sub>|FM junction

Using the method and geometries outlined above, we proceed to study the spin-dependent transmission through ideal Ni|Gr<sub>n</sub>|Ni junctions in the CPP geometry as a function of the thickness of the graphite spacer layer. We then discuss how interface roughness, alloy disorder and graphite-metal lattice mismatch affect the spin-filtering properties of the junctions using large lateral supercells to model the various types of disorder. Similar results are found for all the TMs shown in Fig. 5.1.

### 5.4.1 Specular interface

The spin-dependent transmission through Ni|Gr<sub>n</sub>|Ni (111) junctions is shown in Fig. 5.7 for parallel (P) and antiparallel (AP) orientations of the magnetization in the nickel leads, in the form of the conductances  $G_P^\sigma$  and  $G_{AP}^\sigma$  with  $\sigma = \text{min, maj}$ . All the conductance values are averaged over the four interface configurations of the Ni|Gr<sub>n</sub>|Ni junction which are consistent with AC configurations of the Ni|Gr (111) interface.  $G_P^{\text{maj}}$  and  $G_{AP}^\sigma$  are strongly attenuated, while  $G_P^{\text{min}}$  saturates to an  $n$ -independent value. The magnetoresistance (MR) defined as

$$\text{MR} = \frac{R_{AP} - R_P}{R_{AP}} \times 100\% \equiv \frac{G_P - G_{AP}}{G_P} \times 100\%, \quad (5.1)$$

rapidly approaches its maximum possible value of 100%, as shown in the right inset in Fig. 5.7. This *pessimistic* definition of MR is more convenient here because  $G_{AP}$  vanishes for large  $n$ . It is usually the optimistic version, that approaches 10<sup>12</sup> % in our calculations but does not saturate, that is quoted [9, 10, 50, 51]. The left inset in Fig. 5.7 shows how the conductance depends on the particular configuration of the junction. The minority spin conductance in the parallel configuration, which dominates the magnetoresistance behaviour, is highest for the  $c_1c_1$  configuration with

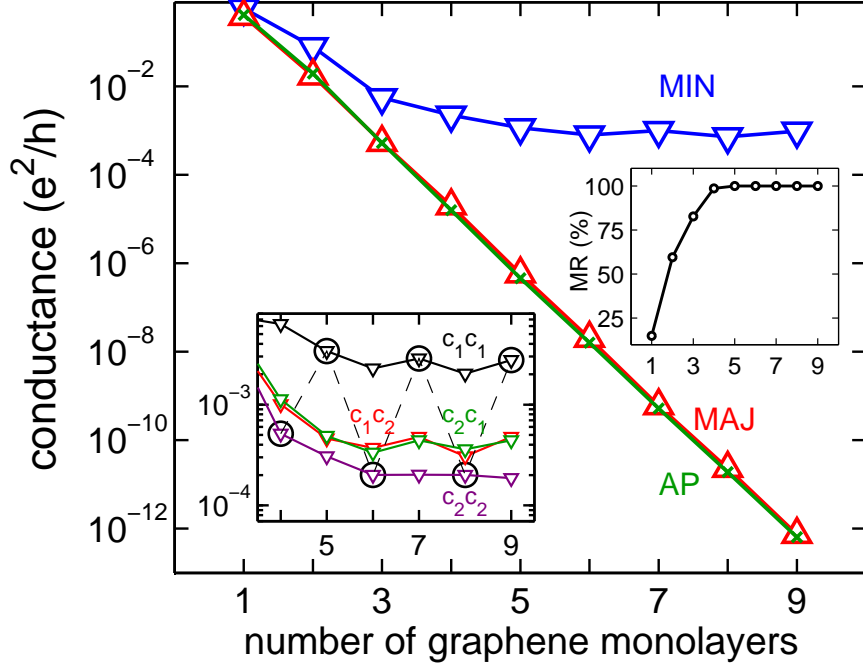


**Figure 5.7:** Conductances  $G_P^{\min}$  ( $\nabla$ ),  $G_P^{\text{maj}}$  ( $\Delta$ ), and  $G_{AP}^\sigma$  ( $\times$ ) averaged over the four configurations  $c_1c_1$ ,  $c_1c_2$ ,  $c_2c_1$  and  $c_2c_2$  of a Ni|Gr<sub>n</sub>|Ni junction as a function of the number of graphene monolayers  $n$  for ideal junctions. Right inset: magnetoresistance MR as a function of  $n$ . Left inset: minority parallel conductance  $G_P^{\min}$  ( $\nabla$ ) given for four different configurations. The points which are circled and connected with a dashed line are the values which were shown in Ref. [1].

a value of  $G_P^{\min} \sim 10^{-2} G_0$ . This is approximately an order of magnitude larger than  $G_P^{\min}$  for the  $c_2c_1$ ,  $c_1c_2$  and  $c_2c_2$  configurations. The  $c_1c_2$  and  $c_2c_1$  configurations are equivalent so the corresponding values of  $G_P^{\min}$  should be identical. The small differences which can be seen in the figure are an indication of the overall accuracy of the numerical calculation. The points which are circled and connected with a dashed line are the values which were shown in Ref. [1].

To demonstrate that spin-filtering occurs due to high transmission of minority spin electrons around the K point, we plot the majority- and minority-spin transmission for the P configuration as a function of  $\mathbf{k}_\parallel$  for two graphite films of different thickness in Figure 5.8. A single sheet of graphene (a monolayer of graphite) is essentially transparent with a conductance of order  $G_0$  in both spin channels. In the minority spin channel, the transmission is very low or vanishes close to  $\bar{\Gamma}$  and along the high symmetry  $\Gamma$ -K line, close to K, in spite of there being one or more sheets of Fermi surface in these regions of reciprocal space. This is a clear indication of the importan-

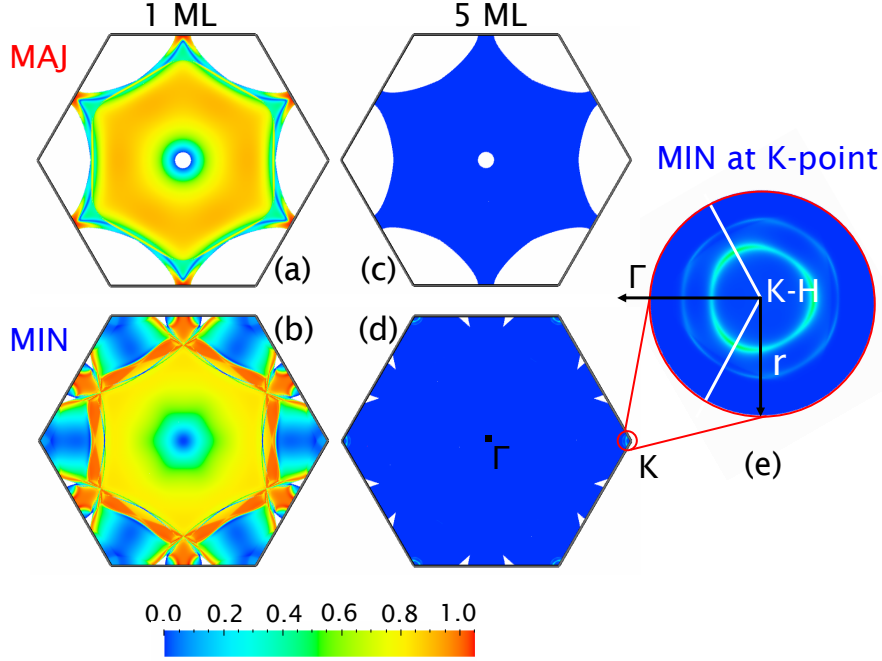


**Figure 5.8:** Transmission as a function of the transverse crystal momentum  $\mathbf{k}_{\parallel}$  in the two dimensional interface BZ for a  $c_1c_2$  configuration of an ideal  $\text{Ni}|\text{Gr}_n|\text{Ni}$  (111) junction in a parallel state. (a) and (b) are for a single graphene sheet,  $n = 1$ ; (c) and (d) are for  $n = 5$ ; (e) shows the minority spin transmission in a small area,  $r = 0.057$  ( $2\pi/a_{\text{Gr}}$ ) around the K point for 5 ML of graphite on an enlarged scale.

ce of matrix element effects: selection rules resulting from the incompatibility of wave functions on either side of the interface [41].

For thicker graphite, the majority transmission must be zero around  $\bar{\Gamma}$  and around the K point because there are no states there in the Ni leads. The only contribution to the conductance comes from tunneling through graphite in regions of the 2D-BZ where there are Ni states and the gap between graphite bonding and antibonding  $\pi$  states is small. This occurs close to the M point; see Fig. 5.3 and Ref. [52]. Because the gap decreases going from M to K, the transmission increases in this direction. At the edge of the Fermi surface projection, the velocity of the Bloch electrons in the leads is zero so that the maximum transmission occurs just on the M side of these edges.

The total minority transmission consist of two contributions. On the one hand there is a tunneling contribution from throughout the 2D-BZ which, depending on the particular  $\mathbf{k}_{\parallel}$  point, is determined by the gap in graphite as well as by the

compatibility of the symmetries, at that point, of the wave functions in Ni and in graphite. On the other hand there is a large transmission from the neighbourhood of the K point coming from the Bloch states there in graphite. Once these have coupled to available states in Ni, this contribution doesn't change as more layers of graphite are added. Perfect spin-filtering (100% magnetoresistance) occurs when the tunneling contributions are essentially quenched compared to the minority spin K point contribution. For four MLs of graphite the polarization is within a percent of 100% and for five MLs it is for all intents and purposes complete. The only discernible transmission in Figs. 5.8(c-e) is found close to the K point. Magnification of this region in Fig. 5.8(e) shows a certain amount of structure in the transmission. This can be explained in terms of the multiple sheets of Ni minority spin Fermi surface in the vicinity of K (Fig. 5.1) and the small but finite dispersion of the graphite bands perpendicular to the basal plane [52]. The transmission is seen to have the threefold symmetry of the junction.

The spin-filtering does not depend on details of how graphite is bonded to the ferromagnetic leads as long as the translational symmetry parallel to the metal-graphite interfaces is preserved. We have verified this by performing explicit calculations (results not shown here) for junctions in the "AB" and "BC" configurations with different metal-graphite separations  $d$ .

#### 5.4.2 Ni|Cu<sub>m</sub>|Gr<sub>n</sub>|Cu<sub>m</sub>|Ni (111)

In Section 5.3, we saw that the electronic structure of a sheet of graphene depends strongly on its separation from the underlying TM substrate. For Co and Ni, equilibrium separations of the order of 2.0 Å were calculated for the lowest energy AC configuration (see Table 5.1), the interaction was strong and the characteristic linear dispersion of the graphene electronic structure was destroyed, Fig. 5.4. For a separation of 3.3 Å, the small residual interaction does not destroy the linear dispersion. Unlike Co and Ni, Cu interacts only weakly with graphene, there is only a small energy difference between the "asymmetric" AC configuration with  $d_0 = 3.3$  Å and the slightly more weakly bound "symmetric" BC configuration with  $d_0 = 3.4$  Å, and bonding to Cu preserves the characteristic graphene electronic structure, opening up only a very small gap of about 10 meV at the Dirac point [53].

Should it be desirable to avoid forming a strong bond between graphite and the TM electrode, then it should be a simple matter of depositing one or a few layers of Cu on e.g. Ni. Such a thin layer of Cu will adopt the in-plane lattice constant of Ni and graphite will bind to it weakly so that the electronic structure of the first layer of graphite will be only weakly perturbed. Because Cu oxidizes less readily than Ni or Co, it may be used as a protective layer. Cu has no states at or around the K point for either spin channel (Fig. 5.1) so it will simply attenuate the conductance of the minority spin channel at the K point. This is demonstrated in Fig 5.9 where the magnetoresistance of a Ni|Cu<sub>m</sub>|Gr<sub>n</sub>|Cu<sub>m</sub>|Ni junction is shown as a function of the number  $m$  of layers of Cu when there are 5 MLs and 7 MLs of graphite. The MR decreases as the thickness of Cu is increased, reducing the transmission of the K point channel. The decrease of MR can be compensated by increasing the thickness

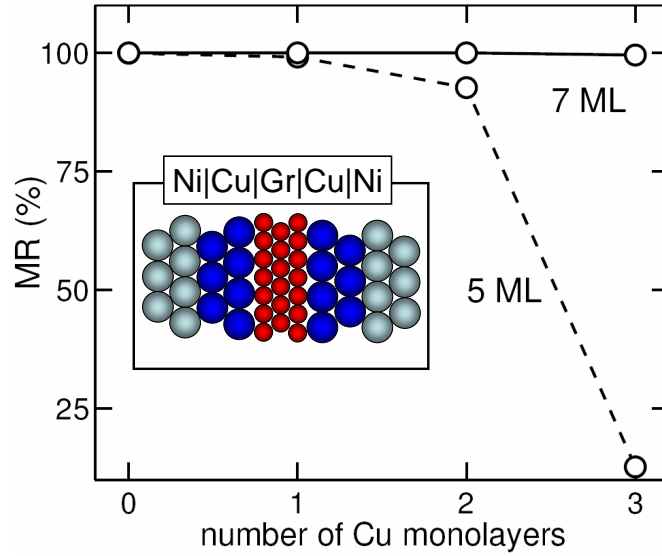


**Figure 5.9:** Magnetoresistance as a function of a number of Cu monolayers on both left and right Ni leads in case of 5 ML (dashed line) and 7 ML (solid line) of graphene.

of graphite. These conclusions are consistent with the qualitative conclusions drawn above in connection with Fig 5.1(i).

Although the linear dispersion of the graphene bands is essentially unchanged by adsorption on Cu, application of an in-plane bias will destroy the translational symmetry parallel to the interface upon which our considerations have been based. The finite lateral size of a Ni|Cu electrode will also break the translational symmetry in a CIP measuring configuration and edge effects may destroy the spin-injection properties. We will return to this issue in the last chapter.

### 5.4.3 Effect of disorder

#### *Lattice Mismatch*

Sofar, we have assumed TM and graphite lattices which are commensurate in-plane. In practice there is a lattice mismatch with graphite of 1.3% for Ni, 1.9% for Co and 3.9% for Cu which immediately poses the question of how this will affect the perfect spin-filtering. While lattice mismatch between lattices with lattice constants  $a_1$  and  $a_2$  can in principle be treated by using  $n_1$  units of lattice 1 and  $n_2$  units of lattice 2 with  $n_1 a_1 = n_2 a_2$ , in practice we cannot perform calculations for systems with  $n$  much larger than 20 which limits us to treating a large lattice mismatch of 5%. To put an upper limit on the effect of a 1.3-1.9% lattice mismatch, we performed calcu-



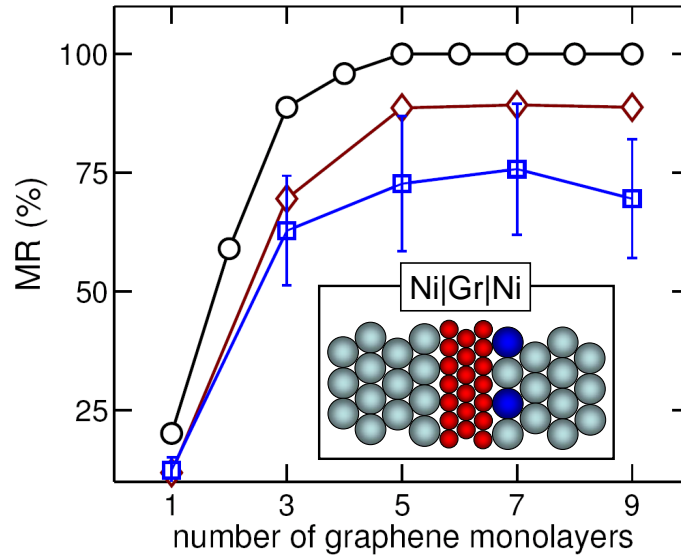


**Figure 5.10:** Magnetoresistance as a function of  $n$  for: (circles) ideal junctions; (diamonds) Ni|Gr <sub>$n$</sub> |Cu<sub>50</sub>Ni<sub>50</sub>|Ni junctions where the surface layer is a disordered alloy; (squares) Ni|Gr <sub>$n$</sub> |Ni junctions where the top layer of one of the electrodes is rough with only half of the top layer sites occupied. The supercell conductances are normalized to the  $1 \times 1$  surface unit cell used for the ideal case. For the rough surface layer, the error bars indicate the spread of MR obtained for different configurations. Inset: schematic representation of Ni|Gr <sub>$n$</sub> |Ni junction with alloy disorder (roughness) at the right Ni|Gr interface. Ni atoms are given by large gray balls while Cu (missing) atoms in the case of alloy disorder (roughness) are given by large black balls. Positions of carbon atoms are represented by small gray balls.

lations for a Ni|Gr<sub>5</sub>|Ni junction matching  $19 \times 19$  unit cells of Ni in-plane to  $20 \times 20$  unit cells of graphite. The effect of this 5% lattice mismatch was to reduce the (pessimistic) magnetoresistance from 100% to 90% (or  $\sim 900\%$  in the optimistic definition). We conclude that the actual Ni|Gr mismatch of 1.3% should not be a serious limiting factor in practice.

Incommensurability is not the only factor that might reduce the magnetoresistance. Preparing atomically perfect interfaces is not possible and raises the question of how sensitive the perfect spin-filtering will be to interface roughness or disorder. Our studies of spin injection in Chapter 2 [15] and TMR in Chapter 3 [14] suggest they may be very important and can even dominate the spin transport properties.

#### *Interface Roughness*

We envisage a procedure for making Ni|Gr <sub>$n$</sub> |Ni junctions in which thin graphite layers are prepared by micromechanical cleavage of bulk graphite onto a SiO<sub>2</sub> covered

Si wafer [54] into which TM (Ni or Co) electrodes have been embedded. We assume that the (111) electrodes can be prepared in ultrahigh vacuum and characterized on an atomic scale and that the surfaces are flat and defect free. Layers of graphene are peeled away until the desired value of  $n$  is reached. Assuming it will be possible to realize one essentially perfect interface, we have studied the effect of roughness at the second interface, assuming it is prepared by evaporation or some similar method. The graphite is assumed to be atomically perfect and all of the roughness occurs in the metal interface layer. We model this roughness as in Ref. [14] by removing a certain percentage of the top layer atoms. The atomic sphere potentials are calculated using the layer version [44] of the coherent potential approximation (CPA) [45]. The CPA-AS potentials are then distributed at random with the appropriate concentration in  $5 \times 5$  lateral supercells and the transmission is calculated in a CPP geometry for a number of such randomly generated configurations. The effect on the magnetoresistance of removing half a monolayer of Ni is shown in Fig. 5.10 as a function of the number of graphite layers. 50% roughness at one interface is seen to reduce the 100% magnetoresistance to about 70% pessimistic (230% optimistic).

#### *Interface Disorder*

The last type of disorder we consider is a layer of interface alloy. We imagine that depositing a layer of Cu on Ni to prevent graphite bonding to the Ni has led to a layer of Ni and Cu mixing. In a worst case scenario, we assume all of the disorder is in the surface layer and assume this to be a  $\text{Ni}_{50}\text{Cu}_{50}$  random alloy. The potentials are once again calculated self-consistently using the layer CPA and the transmission calculated as for roughness. The effect on a monolayer of CuNi alloy is to reduce the MR to 90% (900% in the optimistic definition) for a thick graphite film, as shown in Fig. 5.10.

These results indicate that the momentum transfer induced by the scattering due to imperfections is insufficient to bridge the large gap about the K point in the majority spin FS projections. Alternatively, it may be possible to prepare two separate, near-perfect TM|Gr interfaces and join them using a method analogous to vacuum bonding [55]. Graphite has a large  $c$ -axis resistivity [56]. If one of the TM|Gr interfaces is ideal and the graphite layer is sufficiently thick, then it should be possible to achieve 100% spin accumulation in a high resistivity material making it suitable for injecting spins into semiconductors [57]. Because carbon is so light, spin-flip scattering arising from spin-orbit interaction should be negligible.

## 5.5 Discussion and Conclusions

Motivated by the recent progress in preparing and manipulating discrete, essentially atomically perfect graphene layers, we have used parameter-free, materials specific electronic structure calculations to explore the spin transport properties of a novel TM|Gr $_n$ |TM system. Perfect spin-filtering is predicted for ideal TM|Gr $_n$ |TM junctions with TM = Co or Ni in both fcc and hcp crystal structures. The spin filtering stems from a combination of almost perfect matching of Gr and TM lattices and

unique features of their electronic band structures. Graphite films have occupied states at the Fermi level only around the K-point in the first (interface) BZ. Close-packed surfaces of fcc and hcp Ni and Co have only minority spin states in the vicinity of the K point, at the Fermi energy. For a modest number of layers of graphite, transport from one electrode to the other can only occur via the graphite state at or around the K point. Thus, perfect spin filtering occurs if in-plane translational symmetry is preserved.

The electronic structure calculations presented here have shown that there is a strong hybridization of carbon  $\pi$  orbitals with Ni (Co) surfaces which may suppress spin-injection for both CIP and CPP geometries due to a substrate-induced bandgap in graphene. It has been suggested to use TM|Cu<sub>m</sub>|Gr<sub>n</sub>|Cu<sub>m</sub>|TM junctions where no bandgap opening exists in graphene because the Cu substrate binds graphene weakly. Moreover, using a few monolayers of Cu(111) on the top of Ni(111) electrodes does not degrade the MR for a sufficiently thick graphite film. The TM|Cu<sub>m</sub>|graphene layered structure can be made by intercalation of Cu underneath a graphene sheet on the Ni(111) surface [58]. The use of Cu might also prevent rapid oxidation of the Ni(Co)(111) surfaces, which could be important for making practical devices. Explicit studies of rough or disorder interfaces indicate that the spin-filtering effect will not be critically sensitive to these types of breaking of translational symmetry.

As already discussed in connection with Fig. 5.1, the graphite film in a TM|Gr<sub>n</sub>|TM junction acts as a tunneling barrier (similar to magnetic tunnel junctions) for majority spin electrons whereas it is conducting for minority spin electrons. The minority electron can then transmit via the graphite states similarly to the GMR effect. However, the TM|Gr<sub>n</sub>|TM junction has several important advantages if compared with a conventional TMR junction. Firstly, it has three times smaller lateral lattice mismatch compared to the 3.8% for commonly-used Fe|MgO|Fe(001) junction. This should reduce some of the strain and amount of defects that otherwise limit the thickness and degrade the efficiency of spin injection. Secondly, record breaking values of MR in the TM|Gr<sub>n</sub>|TM junction are predicted. The spin polarization will approach 100% for an ideal junction with  $n > 3$  graphite monolayers, and only reduce to 70-90% for junctions with extremely large disorder and roughness at the TM|Gr<sub>n</sub> interfaces. Thirdly, this spin-filtering effect should be less sensitive to the temperature assuming sufficiently thick graphite interlayer. This conclusion is based upon several observations. The first one is the highest tunneling rate of majority states at M point demonstrated by Fig. 5.8(a). And the second is the large energy gap (almost 1 eV) between the Fermi level and graphite band at this point shown in Fig. 5.3. Typical thermal broadening is, therefore, too small to allow high transmission of the majority electrons in TM|Gr<sub>n</sub>|TM system which could otherwise decrease the spin polarization.

In conclusion, we propose a new class of lattice-matched junctions, TM|Gr<sub>n</sub>|TM, that exhibit exceptionally high magnetoresistance effect which is robust to the interface disorder and roughness, and insensitive to the temperature. All that make these junctions highly attractive for possible applications in spintronic devices.

## Bibliography

- [1] V. M. Karpan *et al.*, Phys. Rev. Lett. **99**, 176602 (2007).
- [2] I. Žutić, J. Fabian, and S. D. Sarma, Rev. Mod. Phys. **76**, 323 (2004).
- [3] A. H. C. Neto, F. Guinea, N. M. R. Peres, K. S. Novoselov, and A. K. Geim, Rev. Mod. Phys. —, (2008), cond-mat/0709.1163.
- [4] M. N. Baibich *et al.*, Phys. Rev. Lett. **61**, 2472 (1988).
- [5] G. Binasch, P. Grünberg, F. Saurenbach, and W. Zinn, Phys. Rev. B **39**, 4828 (1989).
- [6] M. Julliere, Phys. Lett. A **54**, 225 (1975).
- [7] J. S. Moodera, L. R. Kinder, T. M. Wong, and R. Meservey, Phys. Rev. Lett. **74**, 3273 (1995).
- [8] T. Miyazaki and N. Tezuka, J. Magn. & Magn. Mater. **139**, L231 (1995).
- [9] S. Yuasa, T. Nagahama, A. Fukushima, Y. Suzuki, and K. Ando, Nature Materials **3**, 868 (2004).
- [10] S. S. P. Parkin *et al.*, Nature Materials **3**, 862 (2004).
- [11] S. Yuasa *et al.*, Appl. Phys. Lett. **87**, 222508 (2005).
- [12] Y. M. Lee, J. Hayakawa, S. Ikeda, F. Matsukura, and H. Ohno, Appl. Phys. Lett. **90**, 212507 (2007).
- [13] S. Yuasa and D. D. Djayaprawira, J. Phys. D: Appl. Phys. **40**, R337 (2007).
- [14] P. X. Xu *et al.*, Phys. Rev. B **73**, 180402(R) (2006).
- [15] M. Zwierzycki, K. Xia, P. J. Kelly, G. E. W. Bauer, and I. Turek, Phys. Rev. B **67**, 092401 (2003).
- [16] P. R. Wallace, Phys. Rev. **71**, 622 (1947).
- [17] W. M. Lomer, Proc. Royal Soc. (London) A **A227**, 330 (1955).
- [18] J. C. Slonczewski and P. R. Weiss, Phys. Rev. **109**, 272 (1958).
- [19] T. Ando, J. Phys. Soc. Jpn. **74**, 777 (2005).
- [20] H. Ibach and H. Lüth, *Solid-State Physics*, 2nd ed. (Springer-Verlag, Berlin, Heidelberg, 1995).
- [21] K. S. Novoselov *et al.*, Proc. Natl. Acad. Sci. U.S.A. **102**, 10451 (2005).
- [22] K. S. Novoselov *et al.*, Science **306**, 666 (2004).

- 
- [23] K. S. Novoselov *et al.*, Nature **438**, 197 (2005).
- [24] Y. B. Zhang, Y. W. Tan, H. L. Stormer, and P. Kim, Nature **438**, 201 (2005).
- [25] H. B. Heersche, P. Jarillo-Herrero, J. B. Oostinga, L. M. K. Vandersypen, and A. F. Morpurgo, Nature **446**, 56 (2007).
- [26] K. S. Novoselov *et al.*, *sc* **315**, 1379 (2007).
- [27] E. W. Hill, A. K. Geim, K. Novoselov, F. Schedin, and P. Blake, IEEE Trans. Mag. **42**, 2694 (2006).
- [28] N. Tombros, C. Jozsa, M. Popinciuc, H. T. Jonkman, and B. J. van Wees, Nature **448**, 571 (2007).
- [29] Y. S. Dedkov, M. Fonin, and C. Laubschat, Appl. Phys. Lett. **92**, 052506 (2008).
- [30] C. Oshima and A. Nagashima, J. Phys.: Condens. Matter. **9**, 1 (1997).
- [31] Y. Gamo, A. Nagashima, M. Wakabayashi, M. Terai, and C. Oshima, Surface Science **374**, 61 (1997).
- [32] P. E. Blöchl, Phys. Rev. B **50**, 17953 (1994).
- [33] G. Kresse and D. Joubert, Phys. Rev. B **59**, 1758 (1999).
- [34] G. Kresse and J. Hafner, Phys. Rev. B **47**, 558 (1993).
- [35] G. Kresse and J. Furthmüller, Phys. Rev. B **54**, 11169 (1996).
- [36] J. Neugebauer and M. Scheffler, Phys. Rev. B **46**, 16067 (1992).
- [37] G. Giovannetti *et al.*, Phys. Rev. Lett. , accepted (2008), cond-mat/0802.2267.
- [38] O. K. Andersen, O. Jepsen, and D. Glötzl, Canonical description of the band structures of metals in, in *Highlights of Condensed Matter Theory*, edited by F. Bassani, F. Fumi, and M. P. Tosi, International School of Physics ‘Enrico Fermi’, Varenna, Italy, pp. 59–176, North-Holland, Amsterdam, 1985.
- [39] K. Xia *et al.*, Phys. Rev. B **63**, 064407 (2001).
- [40] P. A. Khomyakov, G. Brocks, V. Karpan, M. Zwierzycki, and P. J. Kelly, Phys. Rev. B **72**, 035450 (2005).
- [41] K. Xia, M. Zwierzycki, M. Talanana, P. J. Kelly, and G. E. W. Bauer, Phys. Rev. B **73**, 064420 (2006).
- [42] M. Büttiker, Y. Imry, R. Landauer, and S. Pinhas, Phys. Rev. B **31**, 6207 (1985).
- [43] S. Datta, *Electronic Transport in Mesoscopic Systems* (Cambridge University Press, Cambridge, 1995).

- [44] I. Turek, V. Drchal, J. Kudrnovský, M. Šob, and P. Weinberger, *Electronic Structure of Disordered Alloys, Surfaces and Interfaces* (Kluwer, Boston-London-Dordrecht, 1997).
- [45] P. Soven, Phys. Rev. **156**, 809 (1967).
- [46] T. Hahn, editor *International Tables for Crystallography* Vol. A (Springer, 2005).
- [47] D. Glötzel, B. Segall, and O. K. Andersen, Sol. State Comm. **36**, 403 (1980).
- [48] G. Bertoni, L. Calmels, A. Altibelli, and V. Serin, Phys. Rev. B **71**, 075402 (2005).
- [49] To represent the potential at the Co|Gr and Ni|Gr interfaces, two empty spheres with sphere radii 1.122 a.u. are positioned 0.83 Å above metal B and C sites in model I. In model II, there is one empty sphere with radius 1.7 a.u. positioned 1.28 Å above a metal C site. For Cu|Gr interfaces where the Cu-Gr separation is larger, ("BC" configuration, model I for graphite) three empty spheres with radii 1.612 a.u. are used to fill the interstitial region positioned 1.76 Å above the Cu surface over A, B and C sites.
- [50] W. H. Butler, X.-G. Zhang, T. C. Schulthess, and J. M. MacLaren, Phys. Rev. B **63**, 054416 (2001).
- [51] J. Mathon and A. Umerski, Phys. Rev. B **63**, 220403(R) (2001).
- [52] J.-C. Charlier, X. Gonze, and J.-P. Michenaud, Phys. Rev. B **43**, 4579 (1991).
- [53] G. Giovannetti, P. A. Khomyakov, G. Brocks, P. J. Kelly, and J. van den Brink, Phys. Rev. B **76**, 073103 (2007).
- [54] A. K. Geim and K. S. Novoselov, Nature Materials **6**, 183 (2007).
- [55] D. J. Monsma, R. Vlutters, and J. C. Lodder, Science **281**, 407 (1998).
- [56] K. Matsubara, K. Sugihara, and T. Tsuzuku, Phys. Rev. B **41**, 969 (1990).
- [57] G. Schmidt, D. Ferrand, L. W. Molenkamp, A. T. Filip, and B. J. van Wees, Phys. Rev. B **62**, R4790 (2000).
- [58] Y. S. Dedkov *et al.*, Phys. Rev. B **64**, 035405 (2001).

## Chapter 6

# A new material system for highly planar electronics

*Lattice matched materials have figured prominently in the discovery of new physical effects at interfaces. Because the in-plane lattice constants of graphite, hexagonal boron nitride (h-BN) and of the close-packed surfaces of Co, Ni and Cu match almost perfectly, it should be possible using micromechanical cleavage [1] to prepare ideal interfaces between materials which are respectively, a semimetal, a wide band gap semiconductor, ferromagnetic and nonmagnetic metals. This observation motivated us to investigate theoretically a range of novel layered devices. Using parameter-free energy minimization and electronic transport calculations, we show how h-BN can be combined with the perfect spin filtering property of Ni|graphite and Co|graphite interfaces [2] to make perfect tunnel junctions or ideal spin injectors with any desired resistance-area product. Noting that monolayers of h-BN and the structurally related BC<sub>2</sub>N are direct gap semiconductors, we propose a novel system of planar electronic and light emitting devices.*

Progress in increasing the capacity of magnetic hard disk drives depends on finding materials with large magnetoresistance (MR) ratios and suitable resistance-area (RA) products for use as read-head sensors. Present read-head technology is based upon magnetic tunnel junctions (MTJ) with amorphous Al<sub>2</sub>O<sub>3</sub> barriers and tunneling magnetoresistance (TMR) ratios of 20-70%. The next generation of read heads requiring a larger TMR effect will be based upon “giant TMR” MTJs with MgO tunnel barriers and room temperature TMR ratios of 200-500% [3]. Unless stated otherwise, we use, the so-called *optimistic* definition for magnetoresistance,  $MR = (R_{AP} - R_P)/R_P \equiv (G_P - G_{AP})/G_{AP}$ . Reducing the area A of a junction with a fixed tunnelling resistance per unit area (RA = constant) will increase the resistance R. To reduce RA, the insulating oxide barrier can be made thinner. Currently tunnel junctions are so thin ( $t_{MgO} \sim 1.0$  nm or only 4-5 atomic layers thick)

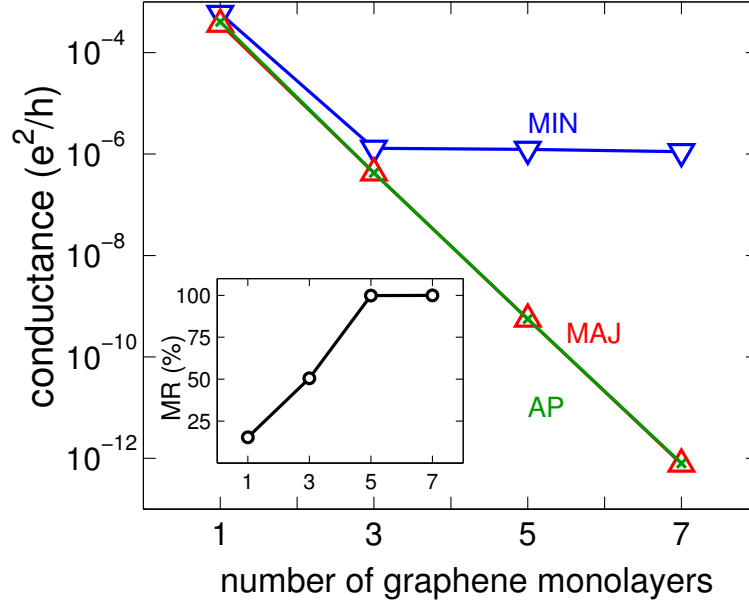


**Figure 6.1:** Conductances  $G_P^{\min}$  ( $\nabla$ ),  $G_P^{\text{maj}}$  ( $\Delta$ ), and  $G_{AP}^\sigma$  ( $\times$ ) of a Ni|BN|Gr<sub>n</sub>|Ni junction as a function of the number of sheets of graphene  $n$ . Results for 2 sheets of BN are shown. Inset: magnetoresistance as a function of  $n$  for ideal junctions. Here, the *pessimistic* definition,  $\text{MR} = (R_{AP} - R_P)/R_{AP} \equiv (G_P - G_{AP})/G_P$  which does not diverge when  $G_{AP}$  is zero, is used.

that further reduction will introduce pinholes. If A is to be reduced even further, it will become necessary to find systems with equally high or higher TMR ratios and lower RA products.

We recently showed [2] that a very few atomic layers of graphite sandwiched between close-packed Ni or Co electrodes should have an infinite magnetoresistance because neither of these transition metal ferromagnets (FM) has majority spin states in the vicinity of the K point of reciprocal space where the graphite Fermi surface is located. As a consequence, the majority spin conductance is attenuated exponentially when the number of graphene sheets (Gr) is increased. There are Ni and Co minority spin states at the K point and once they couple to the Bloch states in graphite, they are not attenuated when its thickness is increased. A FM|Gr<sub>n</sub>|FM magnetic tunnel junctions has a very low RA product ( $\sim 0.5 \Omega \mu\text{m}^2$ ) which depends very weakly on the number  $n$  of graphene sheets. This intriguing behaviour depends upon the happy coincidence that the K points of all three materials coincide which in turn results from a near perfect matching of the in-plane lattice parameters of graphite and close packed surfaces of Ni and Co. Though this prediction of perfect



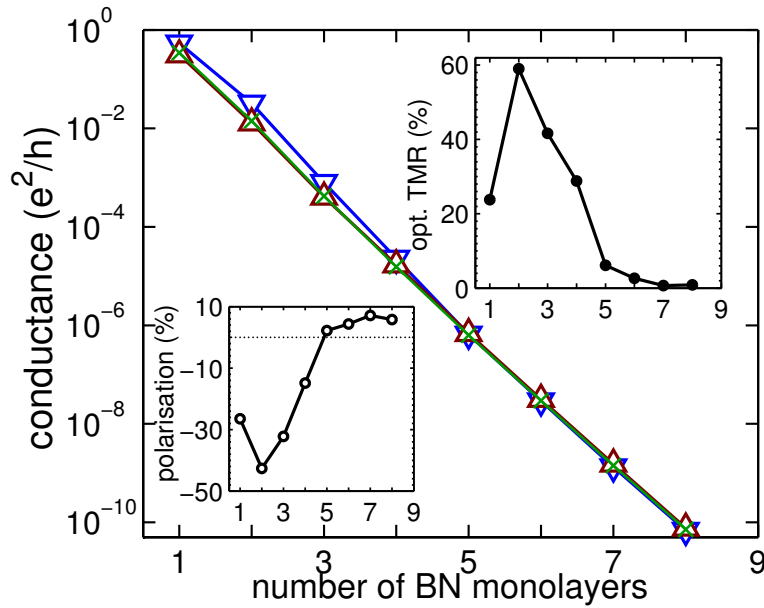


**Figure 6.2:** Conductances  $G_P^{\min}$  ( $\nabla$ ),  $G_P^{\text{maj}}$  ( $\Delta$ ), and  $G_{AP}^{\sigma}$  ( $\times$ ) of a Ni|BN $_n$ |Ni junction as a function of the number of BN layers  $n$  for ideal junctions. Insets: *optimistic* magnetoresistance as a function of  $n$  for ideal junction (on the right) and polarization of the parallel conductance  $P = (G_P^{\text{maj}} - G_P^{\min}) / (G_P^{\text{maj}} + G_P^{\min})$ .

spin filtering has yet to be experimentally confirmed, the physical principles upon which it is based are very well established and robust. Detailed calculations show a remarkable insensitivity to interface roughness, disorder and lattice mismatch.

For other applications it is desirable to have a large RA product. Spin electronics or “spintronics” aims to introduce into conventional semiconductor-based electronics the additional spin degree of freedom used to such good effect in metal-based “magnetoelectronics”. Attempts to inject spins directly into semiconductors encounter a so-called “conductivity mismatch” problem: the difference in spin-up and spin-down resistivity in conventional ferromagnetic metals is negligible compared to the very much larger spin-independent resistivity of semiconductors [4]. This problem can be resolved by injecting spins through a spin-dependent tunnel [5] or Schottky barrier [6] but up till now the spin polarizations achieved at room temperature are far from complete. Here we show how the RA product of a FM|Gr $_n$ |FM junction with FM = Ni or Co, can be made arbitrarily large without reducing the polarization, by inserting  $m$  sheets of h-BN to make an FM|BN $_m$ |Gr $_n$ |FM(111) MTJ. Hexagonal BN is a large band gap semiconductor with an indirect gap of 6 eV[7]. More importantly, it has the same honeycomb structure as graphene, almost the same lattice parameter,

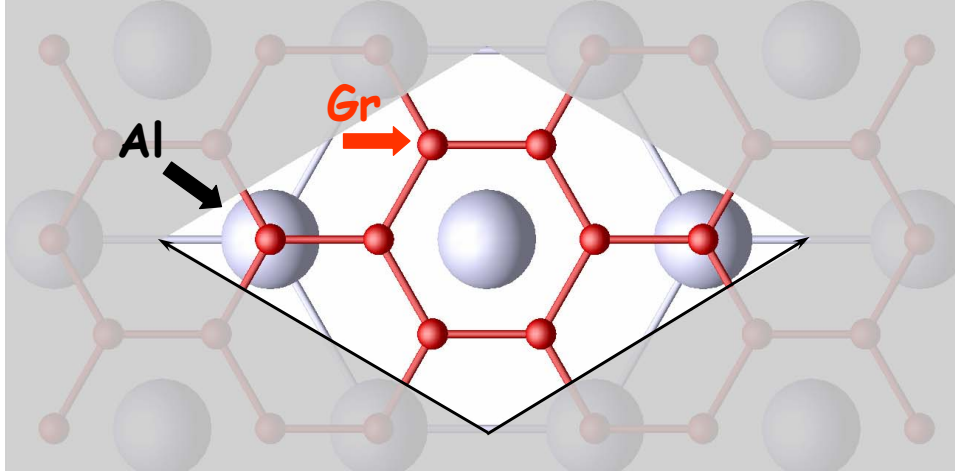


**Figure 6.3:** The most stable configuration of graphene on (111) surfaces of the fcc non-magnetic metals Al, Ag, Au, Pd and Pt with one carbon atom on top of a metal atom (“A” site), and the second carbon on a hollow site (“C” site). The interface unit cell contains 8 carbon and 3 metal atom.

and can be prepared in monolayer form by micromechanical cleavage [1]. Inserting two layers of h-BN increases the RA product by more than three yields of magnitude without any deterioration in the polarization (Fig.6.1). By adjusting the number of layers of h-BN, the RA product can be varied essentially arbitrarily. Relaxed structures were determined *ab-initio* by energy minimization [2, 8] and conductances were also calculated from first-principles [9].

The large magnetoresistance of Fe|MgO|Fe MTJs [10–13] is attributed to the crystallinity of the MgO tunnel barrier. Since h-BN is crystalline and its in-plane lattice constant matches those of (111) Ni and Co to better than a percent, we investigated the magnetoresistance of FM|BN<sub>m</sub>|FM(111) MTJs with *m* sheets of h-BN. The results are shown in Fig. 6.2 for Ni electrodes. It can be seen that in the wide barrier limit the magnetoresistance vanishes. The small MR found for thin barriers can be traced to the existence of a surface state in the minority channel on Ni(111). As the barrier width increases, the contribution from this surface state is quenched. MgO is a cubic material with a conduction band minimum at the  $\Gamma$ -point that is much lower in energy than at other high symmetry points. States at the Fermi energy of the metal electrode which match the *s*-like symmetry of this conduction band minimum are attenuated much more slowly in MgO than states with other symmetries. In the case of Fe, there is a state with this orbital character at the Fermi energy for majority spin but not for minority spin. By contrast, the bottom of the conduction band (top of the valence band) of h-BN at the K,  $\Gamma$ , M, H and

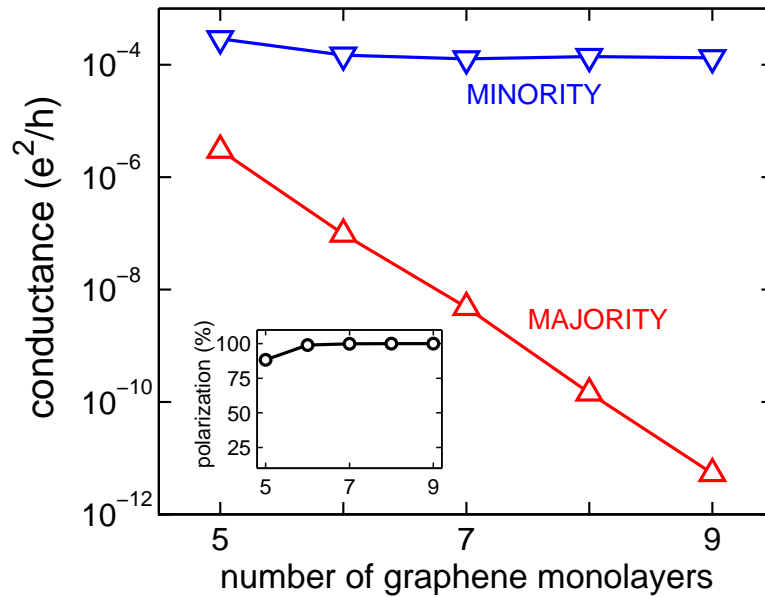


**Figure 6.4:** Conductances  $G_P^{\text{min}}$  ( $\nabla$ ),  $G_P^{\text{maj}}$  ( $\Delta$ ) of a Ni|Gr<sub>n</sub>|Al junction as a function of the number of graphene layers  $n$  for ideal junctions. Inset: spin polarization of injected current as a function of the number of graphene layers  $n$  for ideal junctions.

L (respectively, K,  $\Gamma$ , M, H, A and L) high symmetry points in reciprocal space have very similar energies [7] so that there is no preferential tunnelling of states with a particular orbital character which might translate as in the Fe-MgO case into preference for a particular spin channel. Perfect lattice matching is not sufficient to obtain a large magnetoresistance and h-BN must be used in combination with graphite to obtain a large TMR and large RA product.

The perfect spin filtering properties of graphite on close-packed surfaces of Ni or Co means that this hybrid system, which we denote FM(111)|Gr<sub>n</sub>, behaves as a half-metallic material and can be used to inject a 100% spin-polarized current into nonmagnetic materials. As an example, we consider spin injection into metallic aluminium where till now the most successful means of injecting spin has been by using an aluminium oxide tunnel barrier [14].

The lattice constants of the face-centred cubic non-magnetic metals (NM) Al, Ag, Au, Pd and Pt are such that a  $2 \times 2$  unit cell of graphene containing 8 carbon atoms matches a  $\sqrt{3} \times \sqrt{3}$  surface unit cell of the (111) non-magnetic metal almost perfectly. The most stable configuration of a graphene|NM(111) interface is determined without introducing free parameters by minimizing the density functional theory (DFT) total

energy within the local density approximation. The lowest energy “AC” configuration illustrated in Fig. 6.3 has one carbon atom above a NM atom (the surface “A” sites) while the other is above a third layer Al “C” site. A and C refer to the conventional ABC stacking of the layers in an fcc crystal. The equilibrium interlayer distance at the interface is calculated to be  $d = 3.41$  for aluminium. For the other non-magnetic metals Ag, Au, Pd, and Pt, equilibrium geometries and bonding energies can be found elsewhere [15]. Once an interface geometry has been determined, the conductance can be calculated. The results are shown in Fig. 6.4 for Ni|Gr<sub>n</sub>|Al(111) as a function of  $n$ . This figure demonstrates the saturation of the minority spin injection and rapid exponential attenuation of the majority spin injection resulting in 100% polarization of the injected carriers.

In principle, FM(111)|Gr<sub>n</sub> could be used to inject spins into a doped semiconductor. In practice, it might be necessary to include some layers of h-BN in order to match the impedance of the semiconductor (or to apply a finite bias, though this would go beyond the linear response regime we have implicitly assumed so far). To perform detailed atomistic calculations it is necessary to consider a semiconductor with the same in-plane lattice parameter as graphite - or which can be matched using a reasonably sized supercell. The layered BC<sub>x</sub>N alloy is in this respect a very attractive system because it is intermediate between graphite and h-BN and indeed, h-BN belongs to this system with  $x = 0$ . Because its bandgap is 6 eV, considerable effort has been devoted to the possibility of using h-BN as a source of ultraviolet light [16]. Unfortunately, it would appear that h-BN is an indirect band gap material [7], as is BC<sub>2</sub>N [17].

Our calculations of the electronic structure of BC<sub>x</sub>N indicate however, that monolayers of h-BN or BC<sub>2</sub>N are direct band gap materials. Since calculations for a graphite|BN|graphite sandwich yield a transmission of order 0.1, a monolayer is too transparent to sustain an applied voltage. To inject carriers into a monolayer of h-BN, the electrodes would have to be in the plane of the monolayer of h-BN as sketched in the upper panel of Fig 6.5. A well-known difficulty with this configuration is that electrons and holes injected from either side can pass through the semiconductor without recombining to emit light. This can be solved by constructing a quantum well in which the electrons and holes are trapped until they recombine. In this case the obvious material to use for the quantum well is BC<sub>2</sub>N with a band gap of order 2 eV [17, 18]. A sketch of the quantum well structure is given in the lower panel of Fig 6.5. These configurations are two dimensional analogues of B<sub>x</sub>C<sub>y</sub>N<sub>z</sub> nanotube heterojunctions [19].

## Bibliography

- [1] K. S. Novoselov *et al.*, Proc. Natl. Acad. Sci. U.S.A. **102**, 10451 (2005).
- [2] V. M. Karpan *et al.*, Phys. Rev. Lett. **99**, 176602 (2007).
- [3] S. Yuasa and D. D. Djayaprawira, J. Phys. D: Appl. Phys. **40**, R337 (2007).

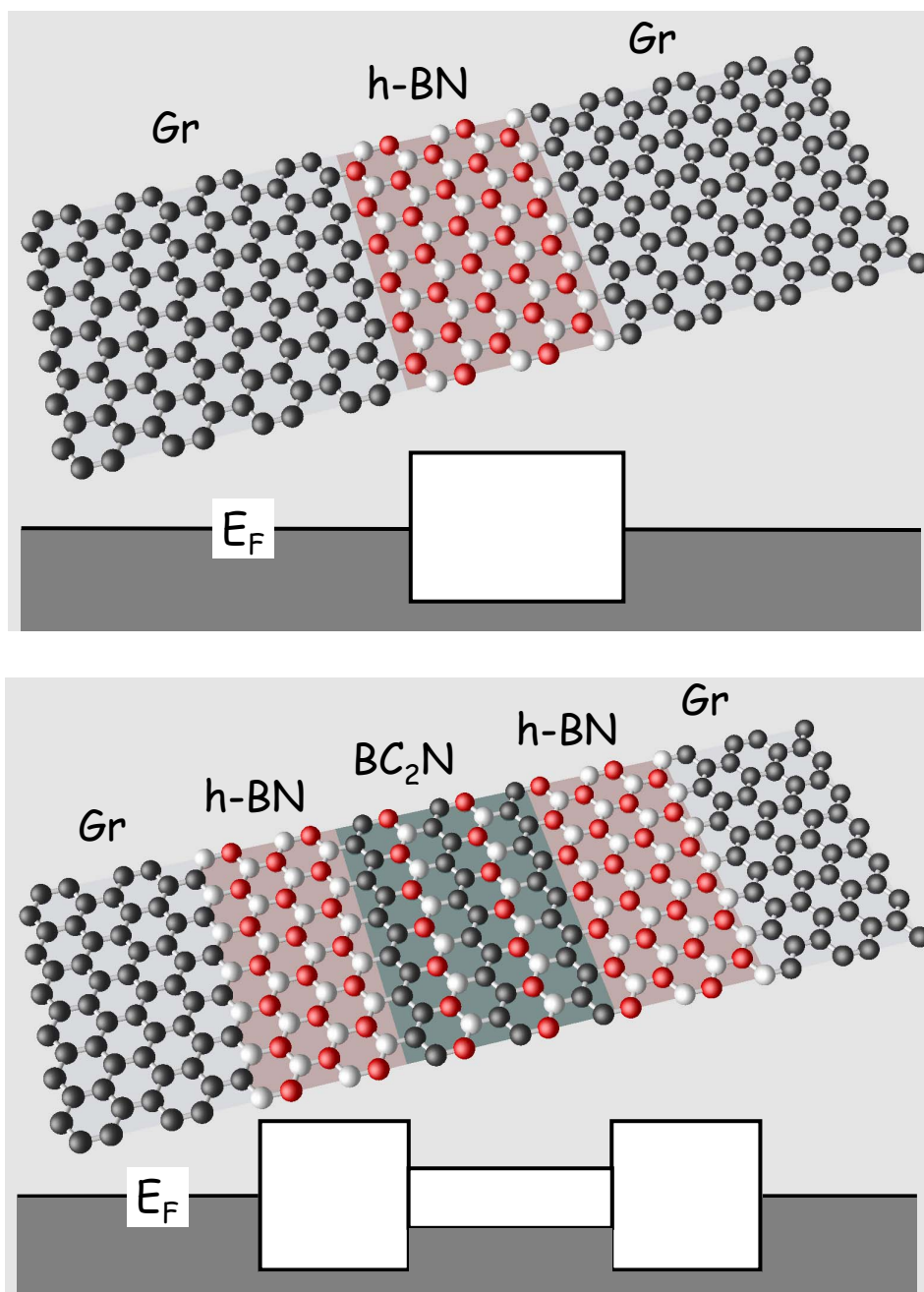


*Figure 6.5:* Top: a two dimensional graphene|BN|graphene tunnel junction. Bottom: a two dimensional graphene|BN|BC<sub>2</sub>N|BN|graphene quantum well.

- 
- [4] G. Schmidt, D. Ferrand, L. W. Molenkamp, A. T. Filip, and B. J. van Wees, *Phys. Rev. B* **62**, R4790 (2000).
  - [5] A. Fert and H. Jaffres, *Phys. Rev. B* **64**, 184420 (2001).
  - [6] A. T. Hanbicki, B. T. Jonker, G. Itskos, G. Kioseoglou, and A. Petrou, *Appl. Phys. Lett.* **80**, 1240 (2002).
  - [7] B. Arnaud, S. Lebegue, P. Rabiller, and M. Alouani, *Phys. Rev. Lett.* **96**, 026402 (2006).
  - [8] G. Giovannetti, P. A. Khomyakov, G. Brocks, P. J. Kelly, and J. van den Brink, *Phys. Rev. B* **76**, 073103 (2007).
  - [9] K. Xia, M. Zwierzycki, M. Talanana, P. J. Kelly, and G. E. W. Bauer, *Phys. Rev. B* **73**, 064420 (2006).
  - [10] W. H. Butler, X.-G. Zhang, T. C. Schulthess, and J. M. MacLaren, *Phys. Rev. B* **63**, 054416 (2001).
  - [11] J. Mathon and A. Umerski, *Phys. Rev. B* **63**, 220403(R) (2001).
  - [12] S. S. P. Parkin *et al.*, *Nature Materials* **3**, 862 (2004).
  - [13] S. Yuasa, T. Nagahama, A. Fukushima, Y. Suzuki, and K. Ando, *Nature Materials* **3**, 868 (2004).
  - [14] F. J. Jedema, H. B. Heersche, A. T. Filip, J. J. A. Baselmans, and B. J. van Wees, *Nature* **406**, 713 (2002).
  - [15] G. Giovannetti *et al.*, *Phys. Rev. Lett.* , accepted (2008), cond-mat/0802.2267.
  - [16] K. Watanabe, T. Taniguchi, and H. Kanda, *Nature Materials* **3**, 404 (2004).
  - [17] Y. Chen, J. C. Barnard, R. E. Palmer, M. O. Watanabe, and T. Sasaki, *Phys. Rev. Lett.* **83**, 2406 (1999).
  - [18] M. O. Watanabe, S. Itoh, T. Sasaki, and K. Mizushima, *Phys. Rev. Lett.* **77**, 187 (1996).
  - [19] X. Blase, J.-C. Charlier, A. D. Vita, and R. Car, *Appl. Phys. Lett.* **70**, 197 (1997).

# Summary

As the technology of semiconductor-based microelectronics approaches fundamental physical limits and there is little prospect of increasing its functionality with currently known materials, more radically different approaches are studied in order to be able to continue making progress in the areas of computing, mobile communication technology etc. One direction being actively pursued is spintronics (spin electronics) that exploits not only the charge of electrons but also their spin. Like compass needles in a magnetic field, electron spins can point up or down which could be very convenient for the binary logic of ones and zeroes. Assuming we can easily define, access and process the electron spin, we can, in principle, make new devices whose architecture relies completely upon quantum mechanical phenomena. This is advantageous, particularly, on small scales and opens the possibility of developing devices that could be much smaller, consume less electricity and be more powerful compared to traditional charge-based devices.

The aim of this thesis was to study theoretically spin-dependent transport in layered structures containing transition metal itinerant ferromagnets, based upon a quantum-mechanical description of electronic transport as the most appropriate for an accurate description on an atomic scale. Our parameter-free material-specific method, which is based upon the density functional theory (DFT), was described in detail in **Chapter 1**. In this chapter the basic concepts of the DFT and local density approximation used for calculating the electronic structure were presented. We reviewed the tight-binding muffin-tin orbital method in the atomic spheres approximation used to solve the Kohn-Sham equations for the one electron potential and the wave-function matching technique for calculating scattering matrices from which the conductance could be determined using the Landauer-Buttiker formalism.

Developing new spintronic devices with enhanced functionality within existing semiconductor technology would be an important advance. Realizing this would require being able to efficiently inject spins into a semiconductor, preferably using direct electrical contacts at room temperature. Ferromagnetic metals are good candidates as spin-injectors because of their high Curie temperatures and because their physical properties and fabrication processes are well studied. However, spin-injection into a semiconductor from a ferromagnetic metal appeared to be very inefficient because of the conductivity mismatch. In **Chapter 2** we studied the influence of interface disorder on spin injection from Fe into InAs. It had previously been suggested that the spin-dependent resistance of an ideal Fe|InAs interface (interface resistance) is

large enough to solve the conductivity mismatch problem. However, interface disorder rapidly quenches the spin-dependence of interface resistance. In our study we revisited this subject. In particular, we found a reduction of the spin polarization of the injected current which was proportional to the interface disorder. We also demonstrated a large sensitivity of polarization to the Fe|InAs interface geometry. To prevent the intermixing of Fe and InAs (interface disorder) and reduce this sensitivity we proposed inserting a buffer layer between the Fe and InAs. A Au buffer layer was found to preserve the injection spin-polarization in the absence of disorder and reduced the disorder quenching. We believe that similar conclusions can be drawn for Fe|GaAs and Fe|MgO|Fe junctions.

The most important application of spintronics, in a broader sense, is as magnetic field sensors in hard disk drive read heads where nowadays magnetic tunnel junctions (MTJ) consisting of two magnetic electrodes separated by a thin insulating layer are displacing metallic spin valves. The operating principle of a MTJ is spin-dependent quantum mechanical tunneling. Tunneling magnetoresistance (TMR) is the change of the electrical resistance of a tunnel junction in an external magnetic field. TMR sensors exhibit large sensitivity and can be made very small, which makes them the key player in the recent progress in magnetic recording. Study of the quantum mechanical magnetoresistance (MR) effects began almost 30 years ago, however, some of the most important issues have remained unresolved. In **Chapter 3** we study the problem of the large discrepancy between theoretically predicted and experimentally measured values of TMR. We shown how taking interface roughness or lead disorder into account can resolve this discrepancy. Observation of a simple relationship between the conductances of MTJs in their parallel and antiparallel configurations has helped us to understand better the Julliere model. This issue was studied in **Chapter 4** using *ab initio* approach. Not only have we demonstrated that Julliere model can be recovered from our results we have also generalized this model to the case of finite biases.

**Chapters 5** and **6** are devoted to the study of a completely new family of spintronic devices. For minority spin electrons there is no overlap between the Fermi surface projections of graphite and Ni or Co (in both fcc and hcp cases) leading us to predict perfect spin-filtering at a graphite|FM(111) interface. From our study we find 100% (maximum) pessimistic MR in FM|graphite|FM (111) junction. We also demonstrate weak sensitivity of the MR to the interface roughness and alloy disorder. In addition, using spin-filtering at graphite|FM interface we demonstrate perfect spin-injection (100% of spin polarization of injected current) into a NM in FM|graphite|NM(111) junctions. We hope that low temperature Andreev reflection experiments would allow proving this effect experimentally. From our first-principles calculations we find that two-dimensional hexagonal-BN and BC<sub>2</sub>N are a direct gap insulator and semiconductor, respectively which allows us to propose a new family of highly planar devices like two-dimensional light emitting diodes.



# Samenvatting

Zoals reeds in de inleiding tot deze thesis werd gesteld, nadert de halfgeleider micro-elektronica de fundamentele fysieke grenzen voor de gebruikte onderdelen. Meer nog, de traditioneel gebruikte materialen en architecturen begrenzen een verdere verhoging van hun functionaliteit. Dit indachtig, is het niet verwonderlijk dat nieuwe alternatieve methoden worden ontwikkeld voor de verdere vooruitgang op gebied van computatie, mobiele communicatie etc. Spintronica (een samentrekking van spin elektronica) zou zo een alternatief kunnen zijn. Hierbij wordt niet enkel gebruik gemaakt van de lading van de elektronen, maar eveneens van hun spin. De spin van een elektron kan net zoals een minuscule kompasnaald "up" of "down" gericht zijn met betrekking tot de richting van een magneetveld, wat uitermate handig is in de binaire logica van enen en nullen. Aannemend dat we de elektronspin gemakkelijk kunnen definiëren, uitlezen en bewerken, dan kunnen we, in principe, nieuwe componenten bouwen waarvan de architectuur volledig is gebaseerd op kwantum mechanische fenomenen. Dit is voordelig enerzijds op zeer kleine schalen, en anderzijds geeft het toegang tot de mogelijkheid componenten te ontwikkelen welke veel kleiner zijn, minder stroom verbruiken en krachtiger zijn dan hun traditionele ladingsgebaseerde evenknie.

Het doel van deze thesis is het theoretisch bestuderen van de spinafhankelijke transporteigenschappen van gelaagde structuren met nanoschaal afmetingen. Om een nauwkeurige beschrijving van het elektronische transport op atomaire schaal te kunnen maken is een kwantummechanische beschouwing het meest geschikt. Onze parametervrije materiaalspecifieke methode, gebaseerd op dichtheidsfunctionaaltheorie(DFT), wordt in detail beschreven in **Hoofdstuk 1**. In dat hoofdstuk worden de basisbegrippen van DFT en de lokale-dichtheids-benadering, gebruikt bij het berekenen van de elektronen structuur, gegeven. Daarna beschrijven we de tight-binding muffin-tin orbitaal methode in de atomaire bol benadering, welke wordt gebruikt bij het oplossen van de Kohn-Sham vergelijkingen voor het berekenen van de één elektron potentiaal. Bij het berekenen van de geleiding uit het Landauer-Buttiker formalisme worden de verstrooiingsmatrices bepaald gebruik makend van de wave-matching techniek.

Een belangrijk voordeel bij de ontwikkeling van nieuwe spintronische componenten is dat ze een verbetering van chipfunctionaliteit binnen de huidige halfgeleider technologie kunnen mogelijk maken. De realisatie hiervan vereist een efficiënte productie van een spingepolariseerd ladingsensemble binnenin de halfgeleider, liefst in direct

elektronisch contact en bij kamertemperatuur. Ferromagnetische metalen zijn goede kandidaten als bronnen van spininjectie enerzijds door hun hoge curietemperatuur en anderzijds omdat hun fysische eigenschappen en fabricatie intensief bestudeerd zijn. De spininjectie in een halfgeleider vanuit een ferromagnetisch metaal blijkt echter niet zo doeltreffend ten gevolge van het geleidings-mismatch-probleem. In **Hoofdstuk 2** hebben we de spininjectie van Fe in InAs bestudeerd. Zoals reeds eerder was voorspeld is de spinafhankelijke weerstand van de ideale Fe|InAs interface (interface weerstand) groot genoeg om het geleidings-mismatch-probleem op te lossen. Spijtig genoeg wordt de spinafhankelijkheid van de interface weerstand snel vernietigd door wanorde aan deze interface. In onze studie hebben we deze resultaten opnieuw bekeken. In het bijzonder vonden we dat de afname in spinpolarisatie van de geïnjecteerde stroom evenredig is met de wanorde aan de interface. Ook hebben we een grote gevoeligheid van de polarisatie aan de Fe|InAs interface geometrie aangetoond. Om het opmengen van Fe in InAs (interface wanorde) tegen te gaan en daarmee de bijhorende gevoeligheid te reduceren stellen we het gebruik van een bufferlaag voor. We vonden een afname van de gevoeligheid van de spinafhankelijke interface weerstand, ten gevolge van interface wanorde, bij het gebruik van een Au bufferlaag in de Fe|Au|InAs systeem. We zijn van mening dat soortgelijke conclusies mogelijk zijn voor Fe|GaAs en Fe|MgO|Fe systemen.

Spintronica in brede zin omvat eveneens magnetoelektronica, waarbij passieve (hierbij kan het signaal niet versterkt worden) spintronische componenten worden bestudeerd. Tegenwoordig is de magnetische tunnel junctie (MTJ) het meest actief bestudeerde object in het gebied van de magnetoelektronica. De werking van een MTJ is gebaseerd op kwantummechanische tunnel magnetische weerstand (TMW), waarvan de herkomst ligt in de mogelijkheid van een component om zijn elektrische weerstand te veranderen ten gevolge van een extern magnetisch veld. Een MTJ bestaat uit twee ferromagnetische metalen leads met daartussenin een dun laagje van een isolator. Magnetische sensors, waarvan de werking is gebaseerd op TMW, hebben een grote gevoeligheid en kunnen zeer klein gemaakt worden. Dit bezorgde TMW een sleutelpositie in de recente ontwikkelingen op vlak van magnetische opname. Hoewel de bestudering van kwantummechanische magnetische weerstand (MW) zijn aanvang ongeveer 30 jaar geleden vond, blijven er nog steeds belangrijke punten onopgehelderd. In **Hoofdstuk 3** bekijken we één zo een probleem: de grote discrepantie tussen de theoretisch voorspelde en experimenteel gemeten waarden voor TMW. Op dit probleem op te lossen stellen we voor wanorde in rekening te brengen. We waren de eersten die de invloed van interface ruwheid en wanorde in de lead legering op TMW bestudeerden op basis van een *ab initio* methode. We ontdekten dat met het in rekening brengen van dergelijke effecten het mogelijk is de kloof tussen theoretische en experimentele resultaten te dichtten. Het waarnemen van een nieuwe relatie tussen de spincomponenten van de geleiding voor parallelle en antiparallelle oriëntatie van de magnetische richting in ferromagnetische leads heeft ons geleid tot een dieper begrip van het Julliere model. Dit punt is in detail bestudeerd in **Hoofdstuk 4** gebruik makend van onze *ab initio* aanpak. Niet enkel hebben we aangetoond dat het Julliere model kan worden afgeleid uit onze resultaten, we hebben eveneens dit model veralgemeend naar het geval waar een eindige bias over de MTJ aangelegd

is.

**Hoofdstukken 5 en 6** zijn toegewijd aan de studie van een compleet nieuwe familie van spintronische componenten. Op basis van waarnemingen van de mismatch tussen de projecties van het fermi oppervlak van grafiet en van het FM (Ni en Co in zowel fcc als hcp geometrie) minoriteits spinkanaal en de goede overeenkomst tussen de projectie van de fermi oppervlakken van grafiet en het FM majoriteits spinkanaal samen met het feit dat hun roosterconstanten bijna identiek zijn, voorspellen we een perfecte spinfiltering aan het grafiet(grafeen)|FM(111) interface. In ons onderzoek vonden we 100% (maximum) MW, pessimistisch geschat, voor de FM|grafiet|FM(111) junctie. Ook toonden we een zwakke gevoeligheid van de MW voor interface ruigheid en legeringwanorde aan. Voorts, gebruik makend van spinfiltering aan het grafiet|FM interface toonden we de mogelijkheid van perfecte spininjectie (100% spinpolarisatie van de geïnjecteerde stroom) in een NM in FM|grafiet|NM(111) juncties aan. We hopen dat lage temperaturens Andreev reflectie experimenten dit effect experimenteel kunnen aantonen. In onze *ab initio* berekeningen vinden we dat tweedimensionale hexagonale BN en BC<sub>2</sub>N systemen directe gat isolatoren en halfgeleiders zijn, welke ons toelaten een nieuwe familie van vlakke componenten, zoals tweedimensionale LED's, voor te stellen.



# Acknowledgments

Little snail  
inch by inch, climb  
mount Fuji !  
*haiku of Issa Kobayashi*

The coming end of my PhD study is marked by the appearance of this book. On its front page you can see only my name, however, other people have made their contributions and in this chapter I would like to acknowledge them.

I would like to begin by expressing my sincere gratitude to my supervisor *Prof. dr. Paul Kelly* whose help was the most significant. First, I would like to thank you Paul for giving me an opportunity to do this PhD and for the support I was receiving during all these years we worked together. Starting from an early morning (three o'clock!) of August the 14th of 2003 when he came to pick me up from the main entrance of the university campus our relations were more than just formal relations between a PhD student and a supervisor. Regular dinners and parties at Paul's place were carried out in a family-like atmosphere created by his wife Andrea who is a very kind and friendly person as well. I thank you Paul for all I learned from you, for your educative fatherlike attitude, your professional expertise which guided me all these years. Finally, I am grateful to you for your help in preparing this thesis.

*Dr. Geert Brocks*, thank you for all the good things I learned from you, for interesting discussions and remarks that helped me to clarify many problems. I am also grateful to you Geert for the discussions and comments on many practical aspects of life in the Netherlands.

*Prof. dr. Claudia Filippi*, despite being employed in the CMS group for only one day a week, your stay in Enschede has never passed unnoticed. Claudia, your personality added new colors to our group. I also appreciate a lot the work you did as a member of my PhD commission.

*Dr. Maciej Zwierzycki* thank you for the time we spend together. I was very lucky to share an office with you during your stay in Enschede. At the beginning of my PhD I had to learn many new things and you were always ready to discuss and explain them. I would also like to mention the leading role you played in many group social activities: doing sport, sailing, and finally the CMS parties. I thank you for work you have put into joint manuscripts which eventually became a substantial part of my thesis.

*Dr. Petr Khomyakov* you were the first person from the CMS group with whom I contacted. During my stay in Enschede our friendship grew up. Not only is it based upon our mutual professional interests but also on a close mentality and common history we both are sharing. I thank you for interesting discussions and help in preparing this thesis.

*Dr. Mohand Talanana*, thank you for all you have done for me. Discussions with you were very interesting, important and useful due to substantial overlap of our interests. You have helped me a lot on different occasions which is very important for me. Mohand, thank you for sharing with me your valuable experience that concerns life outside the university.

Our secretary *Els* is real professional and kind person whose help especially with all the bureaucratic components of life in the Netherlands is difficult to underestimate. Thank you for all. Our new and old system administrators *Enno* and *Gerrit* thank you for taking care about computer facilities here in Enschede.

Working in the CMS group was not only fruitful but interesting and enjoyable greatly due to a reasonably big CMS Slavic Diaspora which also includes *Anton Starikov* (our computer guru) and *Ilya Marushchenko* (an expert in philosophy and culture). Thank you for everything.

The rest of the group members *Victor*, *Paul*, *Gianluca*, *Danny*, *Suleyman*, *Tulika*, *Pengxiang*, *Qingfang*, *Zhicheng*, I would like to thank you guys for the things I have learnt from you and for a good time we had together.

During the first years of my stay in Enschede I was receiving plenty of support and useful feedbacks from a broad former-USSR community at the UT. Among the rest I would like to thank heartily to *Vovan Shchetinin*, *Nina Dzomkina*, *Ivan Nikolaev* and *Sergii Shkulipa* for all the good time we spent together in Enschede.

I would like to express my sincere gratitude to people with whom I worked in Kyiv. Particularly, I would like to mention my supervisor *Dr. Oleksandr Vasyl'ovych Zolotaryuk* his wife *Larysa Andriivna* and my friend and collaborator *Yaroslav*. While working with Oleksandr Vasyl'ovych and Yaroslav I started to build up my international experience and learned to be more independent in my work. I thank you both for all you have taught me. I would like to express my gratitude to *Yulya* and *Victor Khalack* and all the members of the Department of Condensed Matter Physics at the Institute for Theoretical Physics in Kyiv.

I would like to thank to all my teachers from the University in Chernivtsi particularly to my master project supervisor *Prof. Dr. Mykola Vasyl'ovych Tkach* and *Prof. Dr. Stepan Vasyl'ovych Mel'nychuk*. Special thanks go to my university friends from "316": *Igor*, *Lubomyr* and *Rostyslav*.

Finally, I would like to express my deep gratitude to my family. My wife *Yulya* who brought lots of new colors and joy into my life and who supported me through all the years we are together. На сам кінець хотів би подякувати моїй великій родині: батькам, братам та бабусі. Дякую за вашу любов та підтримку, які я відчував всі ці роки. Здоров'я вам всім, добробуту і хай щастить.

Volodymyr Karpan  
June 2008, Enschede

# Curriculum vitae

**Name:** Volodymyr Mykolaiovych Karpan

**16-09-1977** born in Gorodenka, Ivano-Frankivsk region, Ukraine

**1984-1994** secondary school №2, Gorodenka

**1994-1999** **Master of Science** in Theoretical Physics (cum laude):  
*Electron and hole spectra in CdS/HgS/CdS nanoheterosystems*  
National University, Chernivtsi (Ukraine).  
supervisor: Prof. dr. M.V. Tkach.

**1999-2003** **Post graduate study:**  
*Topological defects in the hydrogen-bonded chains*  
Institute for Theoretical Physics, Kyiv (Ukraine)  
supervisor: Dr. O.V. Zolotaryuk.

**2003-2008** **PhD research:**  
*Study of spin transport from first-principles*  
University of Twente, Enschede (The Netherlands)  
supervisor: Prof. dr. P.J. Kelly.

---

## List of publications

[1] *Doping graphene with metal contacts,*

G. Giovannetti, P.A. Khomyakov, G. Brocks, V.M. Karpan, J. van den Brink  
and P.J. Kelly

Phys. Rev. Lett (accepted). (arXiv:0802.2267)

[2] *Calculating Scattering Matrices by Wave Function Matching,*

M. Zwierzycki, P.A. Khomyakov, A.A. Starikov, K. Xia, M. Talanana, P.X. Xu,  
V.M. Karpan, I. Marushchenko, G.E.W. Bauer, G. Brocks and P.J. Kelly

Phys. Stat. Sol. **245**, 623 (2008)

[3] *Graphene and graphite as perfect spin-filters,*

V.M. Karpan, G. Giovannetti, P.A. Khomyakov, M. Talanana, A.A. Starikov, M.

- Zwierzycki, J. van den Brink, G. Brocks and P.J. Kelly  
Phys. Rev. Lett **99**, 176602 (2007). (arXiv:0708.1735)
- [4] *Influence of roughness and disorder on tunneling magnetoresistance*,  
P.X. Xu, V.M. Karpan, K. Xia, M. Zwierzycki, I. Marushchenko and P.J. Kelly  
Phys. Rev. B **73**, 180402(R) (2006) (arXiv:cond-mat/0601291)
- [5] *Conductance calculations for quantum wires and interfaces: Mode matching and Green's functions*,  
P.A. Khomyakov, G. Brocks, V. Karpan, M. Zwierzycki and P.J. Kelly  
Phys. Rev. B **72**, 035450 (2005) (arXiv:cond-mat/0501609)
- [6] *Discrete kink dynamics in a hydrogen-bonded chains: The two-component model*,  
V.M. Karpan, Y. Zolotaryuk, P.L. Christiansen and A.V. Zolotaryuk  
Phys. Rev. E **70**, 056602 (2004)
- [7] *Discrete Topological Kinks in Hydrogen-Bonded Chains*,  
V.M. Karpan  
Ukr. J. Phys. **48**, 689-698 (2003) (in Ukrainian)
- [8] *Discrete Kink Dynamics in Hydrogen-Bonded Chains: The one-component model*,  
V.M. Karpan, Y. Zolotaryuk, P.L. Christiansen and A.V. Zolotaryuk  
Phys. Rev. E **66**, 066603 (2002) (arXiv:nlin/0208049)
- [9] *A new material system for highly planar electronics*,  
V.M. Karpan, P.A. Khomyakov, A.A. Starikov and P.J. Kelly  
(to be submitted) (**Chapter 6**)
- [10] *Graphene and graphite as perfect spin-filters*,  
V.M. Karpan, G. Giovannetti, P.A. Khomyakov, M. Talanana, A.A. Starikov, M. Zwierzycki, J. van den Brink, G. Brocks and P.J. Kelly  
(to be submitted) (**Chapter 5**)
- [11] *Recovering the Jullière model by including interface disorder*,  
I. Marushchenko, V.M. Karpan, M. Zwierzycki, A.A. Starikov and P.J. Kelly  
(to be submitted) (**Chapter 4**)
- [12] *Influence of roughness and disorder on tunneling magnetoresistance*,  
I. Marushchenko, V.M. Karpan, P.X. Xu, M. Zwierzycki, K. Xia, A.A. Starikov and P.J. Kelly  
(to be submitted) (**Chapter 3**)
- [13] *Efficient spin injection from Fe into InAs*,  
V.M. Karpan, M. Zwierzycki and P.J. Kelly  
(to be submitted) (**Chapter 2**)